Towards Atomic Parity Violation at the Francium Trapping Facility

by

Robert Collister

A thesis submitted to
The Faculty of Graduate Studies of
The University of Manitoba
in partial fulfillment of the requirements
of the degree of

DOCTOR OF PHILOSOPHY

Department of Physics & Astronomy
The University of Manitoba
Winnipeg, Manitoba, Canada
November 2015

Thesis advisor

Gerald Gwinner

Author

Robert Collister

Towards Atomic Parity Violation at the Francium Trapping Facility

Abstract

The development of the Francium Trapping Facility at TRIUMF, Canada and progress towards an atomic parity violation measurement in francium are underway. Francium ($Z = 87$) is the heaviest alkali. Its simple atomic structure and large number of nucleons make it an attractive system for weak interaction studies. For this reason, atomic parity violation in francium is an active area of study, and recent years have seen significant progress towards that end.

Laser trapping of francium at TRIUMF has only recently been achieved, and several useful physics measurements for the future atomic parity violation experiment have been performed. The future measurement is of the highly forbidden $7S - 8S$ optical transition amplitude, which is suppressed by $\sim 10^{-10}$ compared to an allowed transition amplitude. This will be achieved by interference with an allowed Stark transition, similar to the $6S - 7S$ optical atomic parity violation measurement in cesium. The commissioning of the two-chamber trapping apparatus as well as the development of the electric field plates for the Stark interference will be reported on.

The physics measurements include the photoionization cross-section from the $7P_{3/2}$ states, and isotope shifts of the $D1$ line. The cross-section must be known

to evaluate a potential atom loss mechanism from the 506 nm light of the $7S - 8S$ excitation, negatively impacting the trapped population. Atomic theory calculations, which are required for the extraction of the weak coupling constants from the atomic measurement, may be benchmarked against these isotope shifts, allowing theorists to refine their techniques for the more sensitive evaluations.

Contents

List of Figures

List of Tables

List of Copyrighted Material for which Permission was Obtained

- Reprinted figure 1.2 with permission from:

  Drell, P. S. and Commins, E. D. *Physical Review A* **32**, 2196–2210 Oct (1985)

  Copyright (1985) by the American Physical Society.

- Reprinted figure 1.3 with permission from:

  Tsigutkin, K., Dounas-Frazer, D., Family, A., Stalnaker, J. E., Yashchuk, V. V., and Budker, D. *Physical Review A* **81**, 032114 Mar (2010)

  Copyright (2010) by the American Physical Society.

- Figure 1.5 reproduced from:

  Wood, C. S., Bennett, S. C., Roberts, J. L., Cho, D., and Wieman, C. E. *Canadian Journal of Physics* **77**(1), 7–75 (1999)

  ©2008 Canadian Science Publishing or its licensors. Reproduced with permission.

- Figure 1.6 reproduced from:

  Erler, J. In *Journal of Physics: Conference Series*, volume 485, 012010. IOP Publishing, (2014)

  under Creative Commons Attribution 3.0 licence.

Acknowledgments

I am grateful to my family for their unwavering support for the many years I have been a student. Thank you all for taking time to let me talk of my work, even if I couldn't always explain it well. To my significant other, that is doubly true for you. Even when we were far apart, you were never far from my thoughts.

I thank all my friends made in the different places I have lived over the course of this education. You have all been a great source of advice and a most useful sounding board when I needed an outside perspective.

My supervisor, Gerald Gwinner, even with the email lag from across provinces, you have always been available for good ideas, direction and focus. The same is true for Matt Pearson and John Behr, on site at TRIUMF; you both helped me immensely in with your experience and stores of spare optics. I thank my committee for all your efforts over the years on my behalf.

A special thank you must go to my fellow student Jiehang Zhang and postdoctoral fellow Michael Tandecki, with whom I spent many years building the lab up from bare concrete. We have all been tired and irritable leading up to beamtime deadlines, but I think we have built a foundation to be proud of. To the rest of the collaboration; your ideas and assistance have been invaluable, even when it wasn't easy or didn't just work.

Finally, all of the support staff, office staff, shops staff and any others I have interacted with over my tenure on this experiment deserve the utmost credit for their efforts. Thank you all very much.

Funding came from the University of Manitoba Graduate Fellowship and Natural Sciences and Engineering Research Council.

This thesis is dedicated to all my loved ones. It's been a long journey and I am only here thanks to each and every one of you.

Chapter 1

Introduction

The Francium Trapping Facility (FTF) at TRIUMF began operation in October 2011 with its first pair of graduate students, shortly joined by a postdoctoral fellow, who started by unpacking the boxes of shipped equipment to fill a days-old, electromagnetically-shielded, steel-walled, empty box-laboratory. Since then, all of the optics, vacuum chambers, and other pieces of apparatus inside the FTF have been designed and constructed by those three young men. The number of small projects and improvements have multiplied over the years and it can be difficult to remember exactly where one's efforts were applied, but such is the nature of a small collaboration. This thesis outlines my contributions to the FTF as we went from bare concrete to the radioactive atom trapping and spectroscopy facility we are today. Much of my efforts are present in the out-of-mind operation of the FTF, such as the placement and alignment of optics, cabling, assistance in construction of the beamline, and a wide variety of jobs required for the initial operation of a laboratory. Many of these tasks will not be mentioned in this thesis as I focus on those with a

greater impact on the operation of the FTF or an original measurement that I took the lead on in the analysis. A secondary purpose of this thesis is to provide an introduction to the facility for future students to assist them in understanding what has been built during my time in the FTF.

This thesis provides an overview of development of the FTF over the past four years. It is organized as follows:

- Chapter 1 provides the motivation for a precision atomic parity violation measurement in francium with a review of previous measurement in other systems. It concentrates on Stark-interference experiments, as that is the type of measurement we are developing for the $7S - 8S$ spectroscopy.

- Chapter 2 examines the theory behind atomic parity violation and the theory of isotope shifts, which we have measured to high precision in a number of francium isotopes.

- Chapter 3 describes apparatus in the FTF, from the delivery of the radioactive francium ion beam to the magneto-optical neutral atom traps where measurements are performed. Progress on the field plates for a Stark-interference measurement is also discussed.

- Chapter 4 contains the experimental technique and analysis of our $D1$ isotope shift measurements in the neutron deficient franciums we have trapped.

- Chapter 5 describes the photoionization cross-section measurement of the $7P_{3/2}$ state of ^{221}Fr we have performed and our use of this quantity to empirically

estimate an important consideration for the future $7S - 8S$ spectroscopy experiment.

- Chapter 6 concludes with a summary of the present state of the FTF and the direction of the ongoing development of the $7S - 8S$ spectroscopy experiment in the near future.

Portions of chapter 4 are adapted from [6], as I was the primary drafter and first author of that publication. Now, onto the current state of the field.

First, I will briefly survey the current state of Atomic Parity Violation (APV), also known as Atomic Parity Non-conservation (APNC), research since the emergence of the field experimentally in 1974. Section 1.1 concerns the discovery of the weak interaction and examines how parity violation arises from the exchange of neutral Z^0 bosons between atomic electrons and the nucleus. Next, a short summary of APV experiments is also provided, showing the two main types of measurements. Section 1.2 presents the atomic cesium and thallium Stark-interference experiments, the two systems in which this technique produced meaningful measurements of APV. A more recent ytterbium measurement is also discussed. The need for improvements in atomic theory in order to reconcile the experimental values with the Standard Model prediction will be briefly discussed. Then section 1.3 considers other weak coupling measurements and the complementarity of these Standard Model testing experiments. Finally, section 1.4 discusses the current status and near future of APV research.

1.1 Electroweak atomic interactions

Violation of parity, or mirror symmetry, was first discovered in 1957 in electroweak processes. Muon decay and nuclear β-decay maximally violate parity[7, 8, 9] and are charged-current interactions; they involve the exchange of electric charge between the interacting particles and hence are mediated by the charged gauge bosons W^+ and W^-. An additional gauge boson Z^0 was predicted by electroweak unification in the late 1960s[10, 11, 12]. The neutral-current interaction is given by a product of vector and axial vector currents between atomic electrons and nucleons. This generates a parity-violating potential that can be split in the non-relativistic limit into two parts depending on the nuclear spin dependence. The Hamiltonian can be written as [13]:

$$H = \frac{G}{\sqrt{2}}(\kappa_{1i}\gamma_5 - \kappa_{nsd,i}\ \boldsymbol{\sigma}_n \cdot \boldsymbol{\alpha})\delta(\vec{r}), \tag{1.1}$$

where G is the Fermi constant, $\gamma_5, \boldsymbol{\alpha}$ are Dirac matrices, $\boldsymbol{\sigma_n}$ are Pauli matrices and $\kappa_{1i}, \kappa_{nsd,i}$ are the coupling constants with $i = p, n$ for protons or neutrons and $nsd =$ nuclear spin dependent. The weak interaction is very short range, its spatial extent characterized by $\delta(\vec{r})$ in this limit. Couplings in the Standard Model take values $\kappa_{1p} = \frac{1}{2}(1 - 4\sin^2\theta_W)$ and $\kappa_{1n} = -\frac{1}{2}$ with $\sin^2\theta_W \approx 0.23$, and θ_W is the Weinberg angle. Equation 1.1 must be summed over all of the nucleons in an atom. The first term, i.e. the nuclear spin independent contribution, which dominates over the other, is usually parameterized:

$$H_{nsi} = \frac{G}{\sqrt{2}}\frac{Q_W}{2}\gamma_5\delta(\vec{r}), \tag{1.2}$$

where $Q_W = 2(\kappa_{1p}Z + \kappa_{1n}N)$ is the dimensionless weak charge of a nucleus with Z protons and N neutrons. In the Standard Model, $Q_W \sim -N$. The second term is

responsible for nuclear spin dependent parity violating effects, such as the anapole moment [14, 15]. The weak interaction mixes the parity of the purely electromagnetic atomic wavefunctions of atoms, allowing otherwise highly forbidden E1 transitions to occur. However, the effect is exceedingly small, enough to make direct measurements lost against the background of the dominant electromagnetic components of transitions. Fortunately, in 1974 it was proposed that APV effects scale with nuclear electric charge roughly as Z^3[16], suggesting that measurements of APV effects would be possible in the heavier atoms.

Thus the question became how best to proceed. Two different experimental methods were developed. The first method is to examine allowed M1 transitions and observe APV as a difference in the index of refraction for right- and left-circularly polarized light as the frequency was scanned across the atomic resonance. Many experiments were conducted on different transitions in bismuth[17, 18, 19, 20, 21, 22, 23], thallium[24, 25] and lead[26]. This type of measurement had the advantage of higher signal-to-noise than the other type of experiment involving forbidden transitions, but the left-right asymmetry was smaller and the atomic structure much more complex. Additionally, the early experiments suffered from serious systematic effects, resulting in very different results obtained by groups measuring the same transition and even within a group at different times.

The second method is to observe highly forbidden M1 transitions such as $6S_{1/2} \rightarrow 7S_{1/2}$ in cesium, $6P_{1/2} \rightarrow 7P_{1/2}$ in thallium or $6s^2\ {}^1S_0 \rightarrow 5d6s\ {}^3D_1$ in ytterbium. E1 transitions between two S or P orbitals are forbidden by parity conservation. Additionally, the M1 transition is suppressed since the radial quantum numbers are

different, allowing for a relatively large APV contribution to the transition amplitude. The parity-violating signal is detected by interference with a Stark-induced E1 transition where an applied electric field mixes the parity of S and P states allowing the transition to occur, more details are provided in section 2.2. Then, with the modulation caused by a reversal of the applied field, the parity violating part in the interference term in equation 1.3 is relatively easy to detect. This technique describes the Stark-interference experiments; however, they each have their own important considerations for a weak interaction measurement. The single valence electron outside a tight atomic core in cesium makes modelling this system easier than more complex atoms, a definite benefit for the extraction of the couplings from experimental results. Conversely, thallium and ytterbium exhibit the effect more strongly, at the price of a more complicated electronic system.

1.2 APV Experiments in detail

The proposal of the Z^3 scaling law in 1974 led to the first experimental measurements of APV in heavy atoms. While the optical rotation experiments have had some success, the most precise APV measurement was via the Stark-interference technique in cesium [27] and was of sufficient precision to unambiguously observe the nuclear spin dependent term of equation 1.1. This thesis builds towards a similar measurement in francium; thus, we shall not discuss the optical rotation measurements further. Instead, we will provide a brief examination of the Stark-interference measurements in three different systems, showing how there is no single approach to this type of measurement.

1.2.1 Stark-interference experiments

In Stark-interference experiments, a laser resonantly excites a parity-forbidden transition that has an amplitude induced by a parity-mixing applied electric field. Modulating the electric field allows detection of the interference between this Stark-induced component, introduced by the applied field, and the very small component allowed by the weak interaction. The purpose is to measure the strength of the parity violating component of a transition relative to another component, resulting in a relative measurement of the weak charge to some more easily measured atomic property. Consider the total transition intensity as the sum of the amplitudes squared:

$$\begin{aligned} I &= |A_{Stark} + A_{M1} + A_{PV}|^2 \\ &= |A_{Stark}|^2 + 2A_{Stark}A_{M1} + 2A_{Stark}A_{PV} + ..., \end{aligned} \tag{1.3}$$

where A_{Stark} is the component attributed to Stark-mixing of the pure angular momentum states, A_{M1} is the magnetic dipole transition and A_{PV} in the weak interaction contribution. With $\vec{E}$ being the applied electric field and $\vec{\epsilon}$ the electric field of the laser, the amplitudes are [3]:

$$A_{Stark}(F, m \to F', m') = \alpha \vec{E} \cdot \vec{\epsilon}\, \delta_{F,F'}\ \delta_{m,m'} + i\beta(\vec{E} \times \vec{\epsilon}) \cdot \langle F'm'| \sigma |Fm\rangle , \tag{1.4}$$

where α, β are the scalar and vector transition polarizabilities, respectively, analogous to the static polarizabilities and F is the total angular momentum of the atom. Certain geometries select specific terms such that the interference term for the weak charge measurement depends only on one of the scalar or vector polarizabilities. The other amplitudes are:

$$A_{M1}(F, m \to F', m') = M(\hat{k} \times \epsilon) \cdot \langle F'm'| \sigma |Fm\rangle , \tag{1.5}$$

where M contains the radial wavefunction integrals, $\hat{k}$ is the wave vector of the laser with Maxwell's equations used to replace its magnetic field with its electric field, and:

$$A_{PV}(F, m \to F', m') = i\text{Im E1}_{PV}\vec{\epsilon}\cdot\langle F'm'|\,\sigma\,|Fm\rangle\,, \tag{1.6}$$

where E1_{PV} contains the radial integrals of the parity violating Hamiltonian in equation 1.1. Thus, the interference terms in equation 1.3 change sign upon a parity reversal of the electric field. Stark interference experiments repeatedly flip the electric field and look for the oscillating signal superimposed on the large $|A_{Stark}|^2$ signal. With a proper selection of geometry, comparing the ratio of the oscillating to constant intensities gives a measurement of $\text{Im E1}_{PV}/\beta$. Systematic errors arise from the $M1$ interference term, which mimics the parity violating interference term, stray electric fields and misalignments.

First, consider the APV experiments performed on the $6P_{1/2} \to 7P_{1/2}$ transition in atomic thallium at 293 nm (figure 1.1 shows the relevant transitions).

In the Stark-interference thallium experiment performed at Berkeley[1], the absoption of 293 nm light was measured in ^{205}Tl for various electric fields. A schematic of the apparatus is in figure 1.2. The light, produced by pulsed dye lasers at 585 nm and frequency doubled to 293 nm, was sent through two Pockels cells, each acting as a half-wave plate, to control the direction of linear polarization with respect to the direction of the applied electric field. A thallium vapour cell, heated to provide vapour density of $\sim 5 \times 10^{14}$ cm^{-3}, contained the coaxial disk electrodes generating the electric field. There were three pairs of electrodes with each able to have an independent voltage applied to it. This produced two separate interaction regions, each

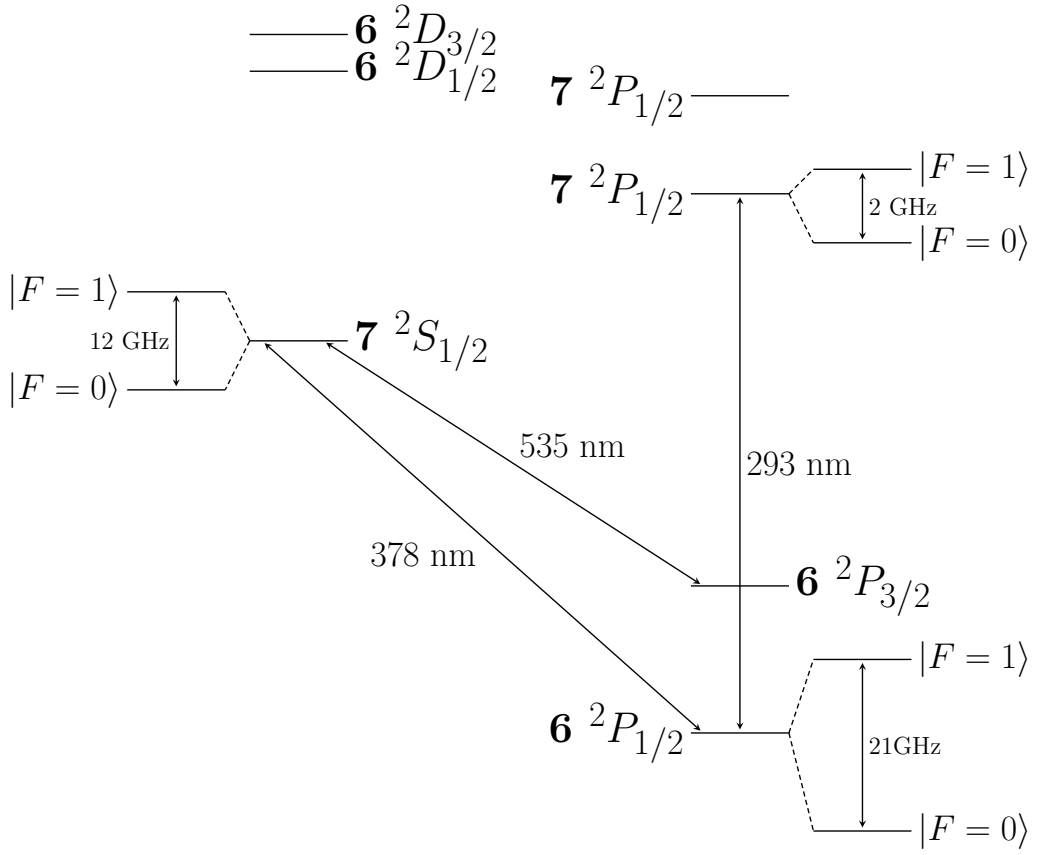

Figure 1.1: The low-lying atomic energy levels above the $6^2P_{3/2}$ ground state of thallium involved in the APV Stark-interference experiment.[1]

observed by a different photomultiplier tube (PMT). The cell was contained inside its oven, which was held under vacuum, and the entire apparatus sat inside an electromagnet providing a homogeneous field. This field Zeeman-shifted the magnetic sublevels so that specific $m \to m'$ transitions could have been selected with specific laser frequencies.

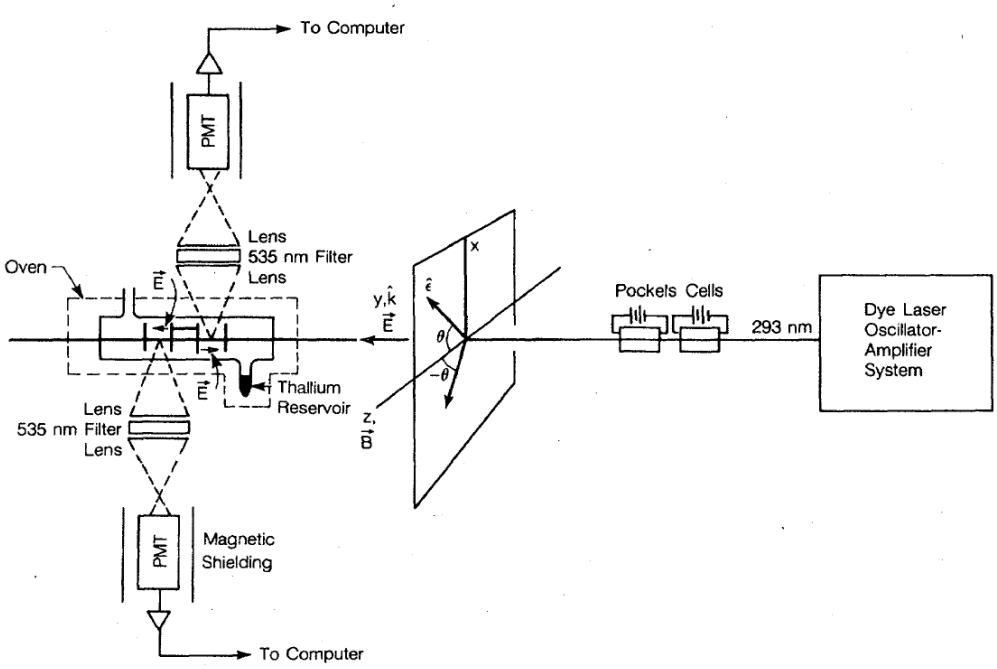

Figure 1.2: Schematic depiction of the apparatus for the thallium APV experiment in Berkeley. The disk electrodes inside the vapour cell had center holes for laser access. An aluminum vacuum chamber contained the cell and sat between the poles of an electromagnet (not shown). Figure taken from ref. [1].

During data acquisition, the outer pairs of electrodes were kept at approximately equal potentials with the center pair kept at the opposite potential, resulting in equal magnitude $\vec{E}$ fields with opposite directions in the interaction regions. This situation provided the parity reversal; while no potentials were changed, the two interaction regions gave parity violating interference contributions of opposite signs. Comparison

of the fluorescence from the two regions allowed the extraction of the interference contribution, and hence a measurement of APV. This was done for linearly polarized laser light set at specific angles with respect to the magnetic field.

Systematic effects which mimic a parity violating signal arise from small misalignments of the electric and magnetic fields and imperfect linear polarizations. These must be very well understood for any Stark-interference APV measurement and will be unique to each apparatus. This thallium measurement claimed a systematic uncertainty of 4% [1]:

$$\mathrm{Im}\frac{\mathrm{E1_{PV}}}{\beta} = (-1.73 \pm 0.26 \pm 0.07)\mathrm{mV/cm}, \tag{1.7}$$

with the first uncertainty being statistical and the second being systematic.

It is important to note that the result of a Stark-interference experiment is a ratio of Im $\mathrm{E1}_{PV}/\beta$, hence β must be well known to extract the weak charge Q_w. Later, a direct measurement of β gave the result [28] (in atomic units):

$$\mathrm{Im\ E1}_{PV} = -2.89 \pm 55 \times 10^{-8}\mu_B, \tag{1.8}$$

where μ_B is the Bohr magneton. The largest single contribution to the uncertainty is the value of the A coefficient, i.e. the spontaneous emission rate, calculated from atomic theory, for the $6P_{1/2} \rightarrow 7S_{1/2}$ transition, required to extract this absolute measurement of Im $\mathrm{E1}_PV$. The dependence on this A coefficient arises from the polarizability measurement being a relative intensity of the allowed $6P_{1/2} \rightarrow 7S_{1/2}$ transition to the induced $6P_{1/2} \rightarrow 7P_{1/2}$ transition. Thus the limiting factor remains the complexity of the atomic calculations.

More recently, an ytterbium Stark-interference measurement has been reported from Berkeley[2, 29]. A schematic of the apparatus is shown in figure 1.3. This

experiment employed a collimated atomic beam of ytterbium sent through a pair of parallel electrodes, similar to the apparatus of the cesium APV experiment with the lowest systematic error, which is discussed in section 1.2.2. Wire-frame electrodes allowed the 408 nm light through, and a power buildup cavity (PCB) generated large intensities of that light incident on the atoms in the interaction region. The applied field was sinusoidal in time with a dc bias, providing a modulating signal for isolation of the interference from the dominant Stark-induced transition. Detection occurred downstream from the interaction region. There, atoms populating the $6s6p\ ^3P_0$ state, to which 65% of the $5d6s\ ^3D_1$ spontaneous decays go, were resonantly excited to the $6s7s\ ^3S_1$ state by 649 nm light, and decay fluorescence was detected by a photodiode.

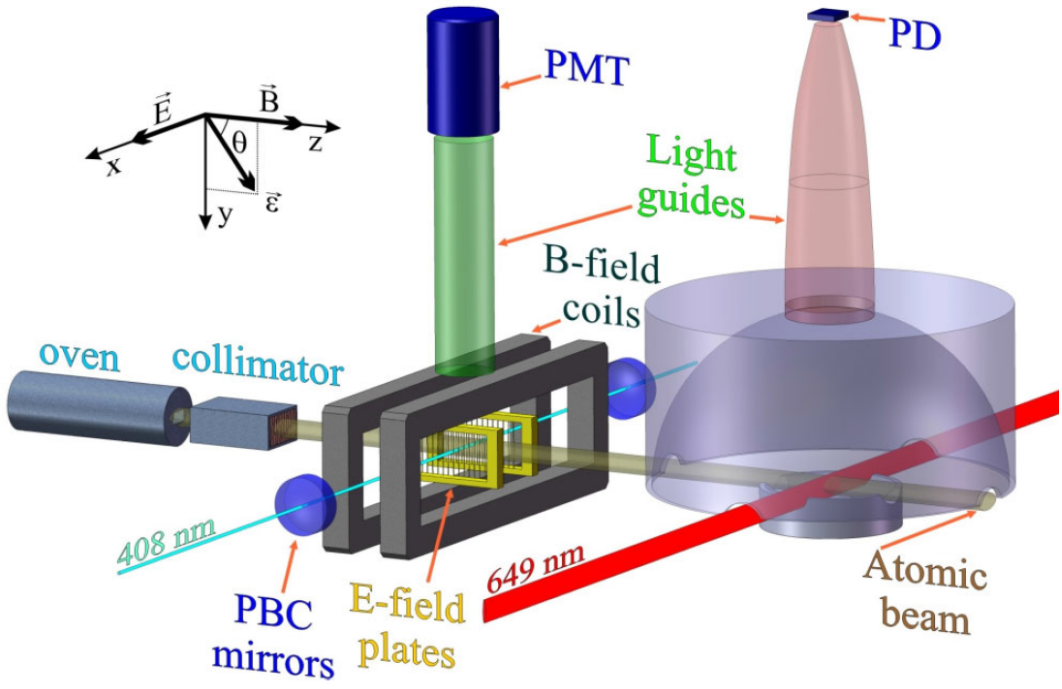

Figure 1.3: Schematic depiction of the apparatus for the ytterbium APV experiment in Berkeley. The wire-frame electrodes allow optical access for the 408 nm light in a power buildup cavity. Detection occurs downstream in a resonant excitation of atoms that underwent the Stark-induced transition. Figure taken from ref. [2].

The final result of this experiment was a value of [2]:

$$\mathrm{Im}\frac{\mathrm{E1_{PV}}}{\beta} = (39 \pm 4 \pm 3)\mathrm{mV/cm}. \tag{1.9}$$

Along with a previously measured β [30], this gives a parity violating amplitude of (in atomic units):

$$\mathrm{Im\ E1_{PV}} = 8.7 \pm 1.4 \times 10^{-10} e a_0, \tag{1.10}$$

with an uncertainty still much above the $< 1\%$ accuracy needed to observe nuclear spin dependent APV.

1.2.2 The cesium experiment

The early Stark-interference experiment in cesium showed the potential for a high precision measurement in this system [31, 32]. However, the best cesium measurement, and most precise APV measurement to date, belongs to the Boulder group [27]. This experiment excited the $6S_{1/2} \rightarrow 7S_{1/2}$ transition (figure 1.4 shows the relevant transitions) in a region of perpendicular electric, magnetic and laser fields. The handedness of this region was reversed by reversing the direction of each field, invoking a parity transformation. The parity violating component was then the amplitude unaffected by these reversals.

The apparatus (as shown in figure 1.5) consisted of an effusive beam of atomic cesium from an oven[3]. The beam was prepared in the desired hyperfine level by optical pumping en route to the interaction region. The electric field in the interaction region was provided by a pair of parallel plates 0.98577(25) cm apart operated at typically 500 V between plates. There were 23 magnetic field coils driven with both

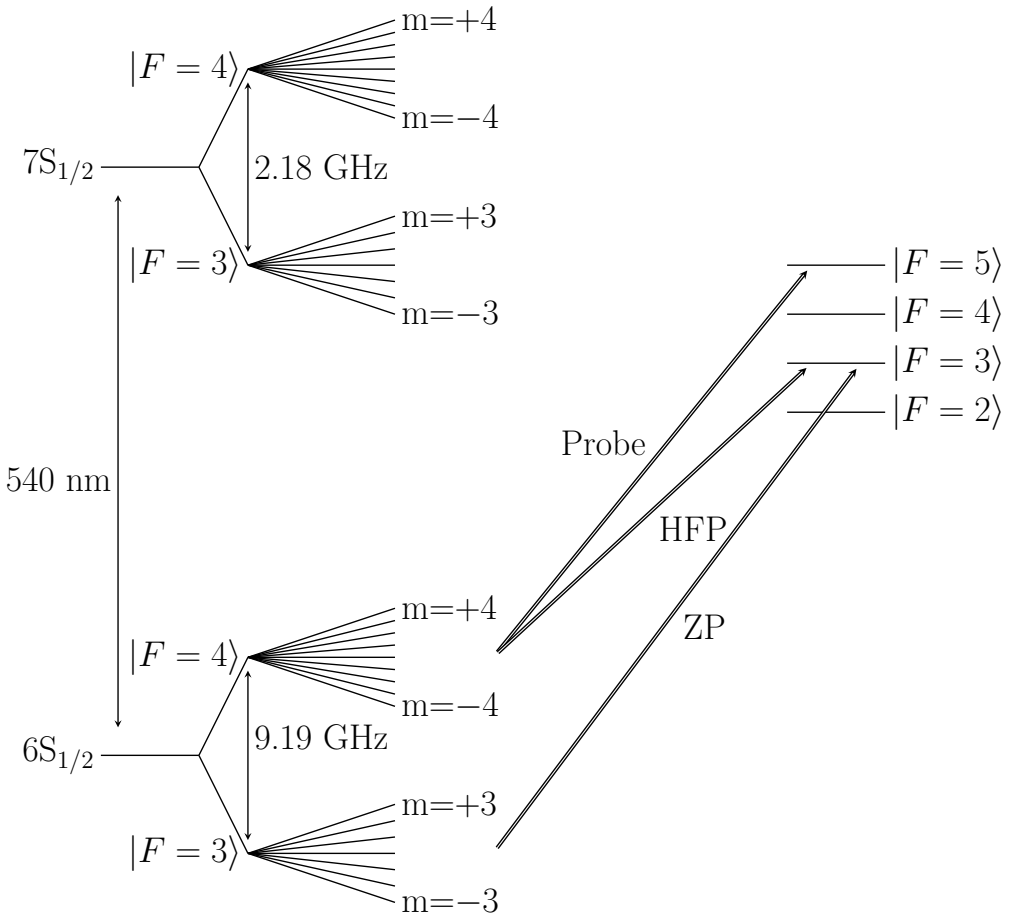

Figure 1.4: The low-lying energy levels of atomic cesium showing hyperfine and weak-field Zeeman structure as relevant to the Boulder APV experiment. Laser designations refer to figure 1.5. Figure taken from ref. [3].

reversing and nonreversing components of current to produce the required fields in the optical pumping and interaction regions, with zero magnetic field in the detection region. An ensemble of 31 different servosystems provided optical, mechanical and thermal stability to achieve sufficiently precise alignment and control of all aspects of the experiment.

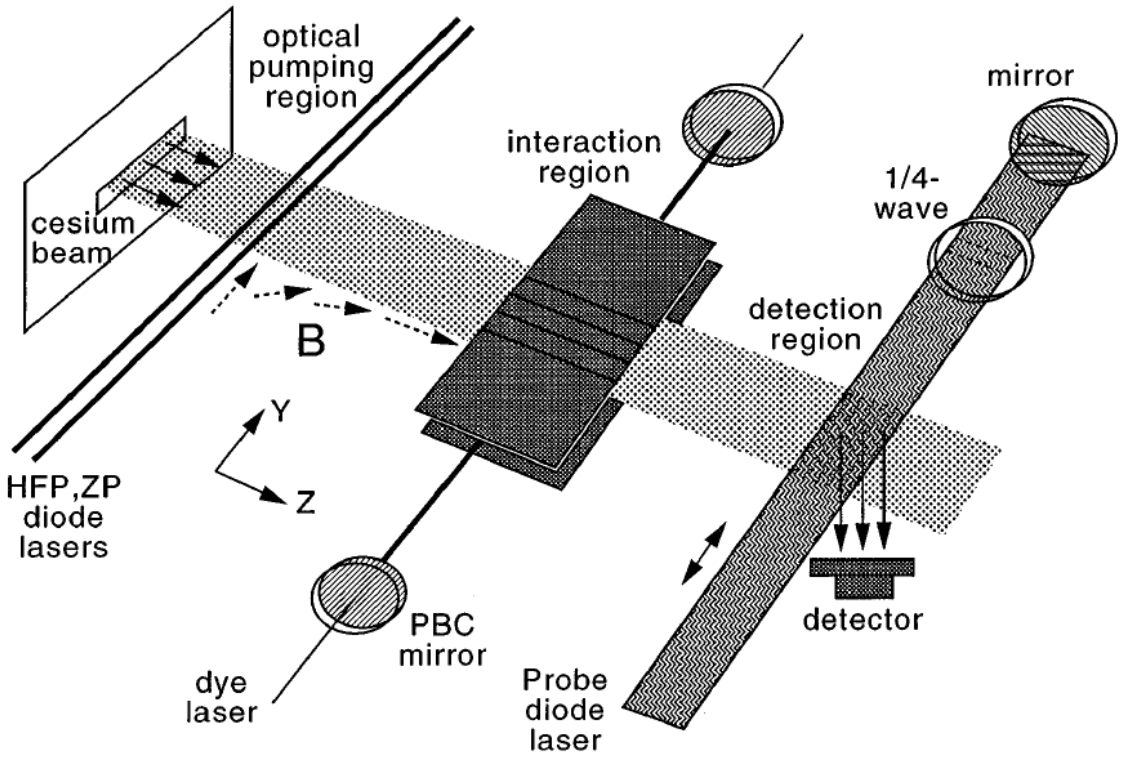

Figure 1.5: Schematic of the apparatus from the Boulder APV experiment on cesium. The hyperfine(Zeeman) pumping in the optical pumping region prepares the beam into a desired hyperfine(m) state by exciting the required $6S_{1/2} \rightarrow 6P3/2$ transitions. The interaction region is characterized by $\vec{B}$ along the z axis, $\vec{E}$ along the x axis and the $6S_{1/2} \rightarrow 7S_{1/2}$ excitation laser beam defines the y axis. Figure taken from ref. [3].

Atoms were optically pumped to one hyperfine ground state, and then they were excited through the Stark-induced transition. Once in the $7S_{1/2}$ state, they decayed

via the $6P_{3/2}$ and $6P_{1/2}$ states to the previously empty $6S_{1/2}$ hyperfine state with 60% probability. Atoms in this state were excited by another laser back into the $6P_{3/2}$ state many times in the detection region. Cycling this transition produced 100 to 240 photons per atom, depending upon which hyperfine state was being detected. The scattered photons were collected by a silicon photodiode. All of the lasers involved in this experiment were stabilized by both optical and electronic feedback, locking them to their desired atomic transitions. This ensured the high signal-to-noise ratio required for such a precise experiment.

One remarkable point about this measurement is that the high precision enabled a comparison of the parity violating amplitude for transitions involving different hyperfine states. This yielded the first unambiguous observation of nuclear spin-dependent APV and is a manifestation of the nuclear anapole moment. The final reported result is:

$$\text{Im E1}_{PV}/\beta = \begin{cases} -1.6349(80)\text{mV/cm} \\ -1.5576(77)\text{mV/cm} \end{cases} \tag{1.11}$$

for the $6S\ F = 4$ to $7S\ F = 3$ and $6S\ F = 3$ to $7S\ F = 4$ transitions respectively. The difference between them is the much smaller spin dependent component of the APV effect, which is hidden below the uncertainties of other measurements. Statistical uncertainties, 0.0078 and 0.0073 mV/cm respectively, dominate the errors as systematics such as misaligned or stray fields, mirror birefringence and laser power fluctuations are all well taken care of to the sub-0.1% (at most) level. It is worth noting how this result is usually quoted: i.e. the value of $\text{Im E1}_{PV}/\beta$ means that the APV effect is equivalent in this transition to a Stark effect with an applied ~ 1.6 mV/cm electric field, thus indicating just how small the APV effect is. The vector transition

polarizability β was measured shortly after the Stark-interference experiment [33].

1.2.3 Revision to atomic theory

A thorough understanding of the atomic systems involved in these experiments is required to extract the Standard Model parameters from the results. Initially, the precise cesium measurement disagreed at 2.5σ with the Standard Model value of $Q_w(\mathrm{Cs}) = -73.19(13)$ until advancements in atomic theory resolved the discrepancy [34]. It was discovered that higher-order bound-state QED radiative corrections were required to properly interpret the result, in addition to improvements in neutron distribution, strong-field self-energies and relativistic correction calculations. This, in turn, brought the Boulder cesium APV measurement of $\sin^2\theta_W$ (extracted from $Q_w(\mathrm{Cs}) = -72.2(8)$) into 1σ agreement with the Standard Model and allowed reliable bounds on the weak couplings involved to be imposed.

More recently, further developments in APV calculations[35, 36] have reduced the theory uncertainty, and they have also introduced new controversy. The first theory result produced a weak charge of the ^{133}Cs nucleus $Q_{weak} = -73.16(29)_{expt}(20)_{theory}$ [35], precisely ($< 1\sigma$) in agreement with the Standard Model and with a small theory error pushing the experiment to once again give the largest uncertainty. Later, a reexamination of that calculation by another group produced a slightly different result, $Q_{weak} = -72.58(29)_{expt}(32)_{theory}$ [36]; this is 1.5σ below the Standard Model value and the theory error is again the larger uncertainty. As yet, there has been no resolution to which is the preferred result.

1.3 Weak coupling constraints from other sources

APV experiments measure the weak nuclear charge, from which the weak couplings of the quarks can be extracted. These low-energy results complement the high-energy accelerator experiments, as shown by figure 1.6. In particular, they measure couplings between new particles and the first generation of quarks. The constraints imposed by APV experiments run essentially orthogonally to those imposed by the high-energy experiments, as shown in figure 1.7.

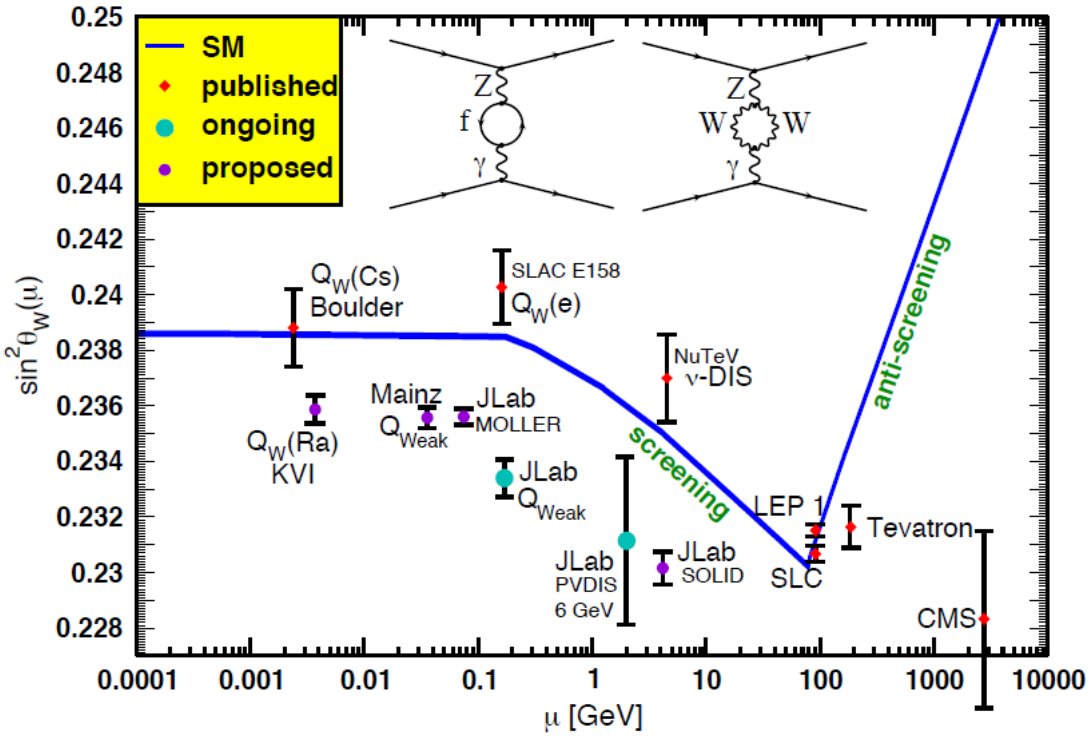

Figure 1.6: Current and future experimental determinations of the Standard Model parameter $\sin^2\theta_W$. The relevant momentum transfer μ of the Tevatron and CMS values make them effectively Z-pole, i.e. rest mass of the Z boson, measurements and they have been shifted horizontally for clarity. Figure taken from ref. [4].

The experiments all probe different couplings. APV is predominantly sensitive to

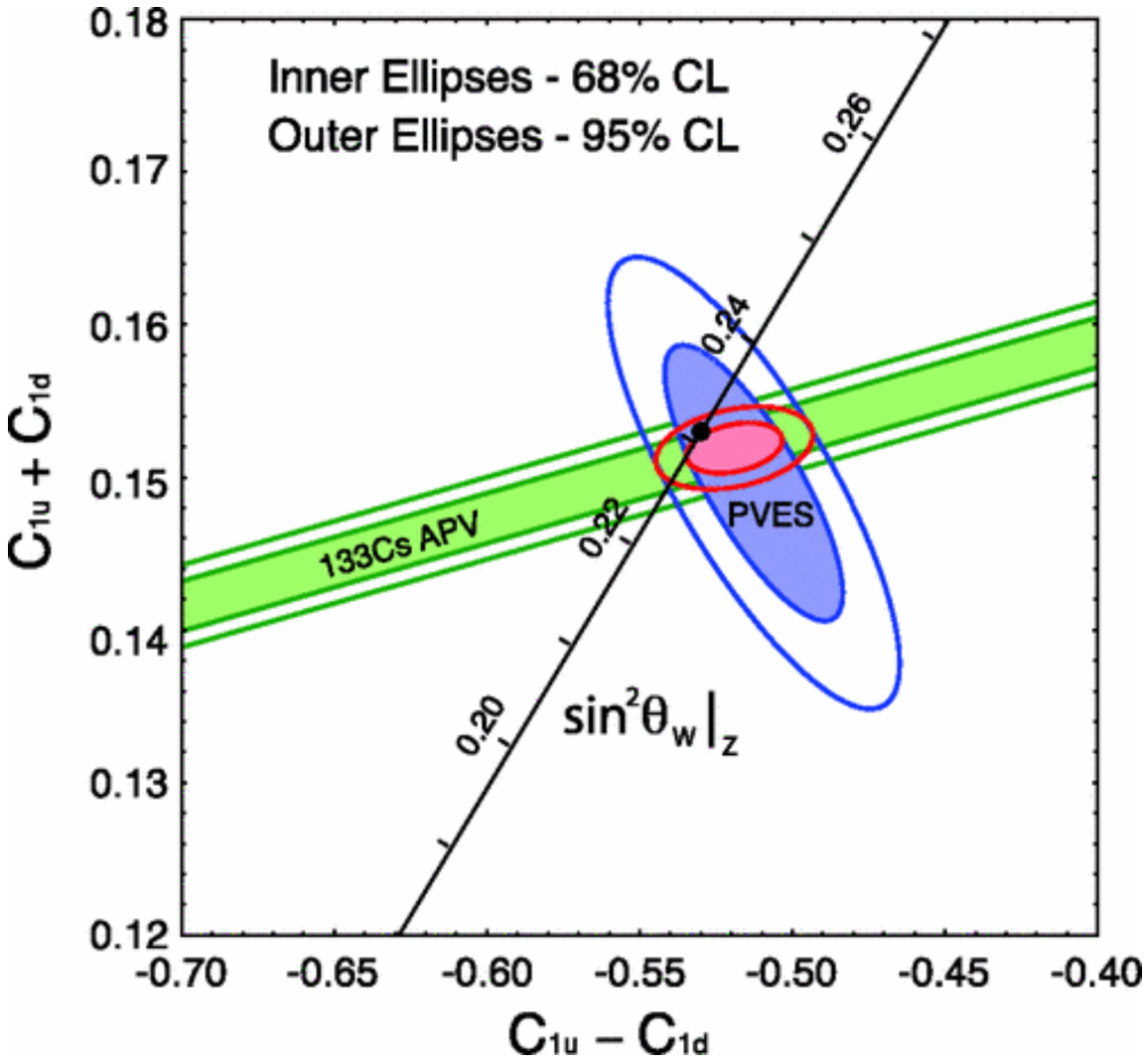

Figure 1.7: Constraints imposed by the different parity violation experiments on the neutral-weak quark coupling constants, showing the complementary nature of APV to the high energy electron scattering experiments. The black dot indicates the Standard Model prediction. Figure taken from ref. [5].

the neutron's weak charge, Qweak's $\vec{e}+p$ scattering determines the proton's weak charge and E158's $\vec{e}+e$ scattering measures the electron's weak charge. They all constrain different avenues of extending the Standard Model. APV is very competitive concerning searches for extra gauge bosons [37, 38, 39] and leptoquarks [40], where purely leptonic scattering has little sensitivity.

1.4 Outlook

The cesium experiment, along with the new atomic physics calculations, has determined the weak Cs atom's charge to 0.6% accuracy, in fair agreement with the Standard Model. A new experiment in cesium with a novel coherent control method [41] is seeking confirmation with a measurement of similar or better precision. Other experiments using single trapped ions of Ra^+[42] or Ba^+[43] have made good progress in developing their aparatus and should produce results in the near future. Additionally, a parity violation measurement in BaF molecules is in progress [44]; the group anticipates sensitivity to the anapole moment, and there is also the ytterbium experiment[2] previously mentioned. Thus, there are a number of competing APV experiments in progress.

There are also a number of groups working with francium for fundamental symmetry tests, such as searching for permanent electric dipole moments [45, 46]. Our experiment is in direct competition with another collaboration which similarly traps francium for an APV measurement [47]. We have the advantage of a larger ion beam and have collected $> 10^5$ atoms in our first trap, compared to their $\approx 10^3$ trapped atoms. The APV effect is predicted to be almost $20\times$ larger in francium compared to cesium.

All of these APV experiments can potentially be of great importance. A measurement in another system than cesium will help to discriminate between the many methods used in the atomic theory calculations. Francium, along with the monovalent ions Ba^+ and Ra^+, should have similarly accurate levels of calculations with a sizable APV effect. However, francium has different-sized radiative corrections than cesium,

and calculations that agree in cesium differ for francium [48]. An APV measurement in francium will differentiate between the methods, allowing further refinement and a corresponding decrease in the theory error.

Chapter 2

Theory

2.1 Atomic parity violation (APV)

Glashow-Weinberg-Salam theory is based on the SU(2)xU(1) symmetry group and can be used to generate the expressions for the neutral current interaction between atomic electrons and nuclei in section 1.1. This theory frames the electroweak interaction in terms of a mixing angle θ_W and four vector bosons: the photon (γ), neutral weak boson (Z^0) and charged weak bosons ($W^{\pm}$). The heavy Z^0 and $W^{\pm}$ bosons mediate the short-ranged neutral and charged weak current interactions, respectively. The theory follows a vector-axial vector form, describing how interactions behave under charge conjugation, parity and time reversal (CPT) symmetry transformations.

Parity violating transitions in atoms are generated primarily by the exchange of the weak neutral currents between electrons and nucleons. The weak interaction mixes states of opposite parity resulting in modification of the pure angular momentum states and allowing otherwise forbidden transitions to occur, although the effects

are exceedingly small. Recall that APV is predicted to scale with nuclear charge roughly as Z^3 [16], suggesting that measurements of its effects are possible in the heavier atoms. Francium makes an ideal system for these measurements due to its large number of nucleons and simple atomic structure. The single valence electron in francium makes extracting the electron-nucleon couplings from experimental results easier than other, more complex systems. The APV effect can be divided into two types, according to the dependence on the nuclear spin of the atom.

2.1.1 Nuclear spin independent APV

The nuclear spin independent component of APV is the largest contributor to the total effect. This component arises from the exchange of a neutral Z^0 boson between a nucleon and an orbiting electron (nucleon vector current), see figure 2.1. The parity-violating Hamiltonian from equation 1.1 mixes electronic states of opposite parity, allowing otherwise highly forbidden transitions to occur. Thus, measuring the transition amplitude arising from this effect can provide a precise measurement of the pivotal parameter known as the weak mixing angle $\sin^2\theta_W$ in the low-energy regime of the Standard Model. The final result of an APV measurement is often reported in terms of the weak charge of a nucleus Q_W.

The $7S - 8S$ transition in francium is electric dipole forbidden, making it an ideal candidate for an optical APV experiment. A similar measurement of the cesium $6S-7S$ transition [27] is the current standard. However, the cesium result was initially in 2.5σ disagreement with the Standard Model prediction; higher-order bound-state QED radiative corrections were required to properly interpret the result[49, 48], in

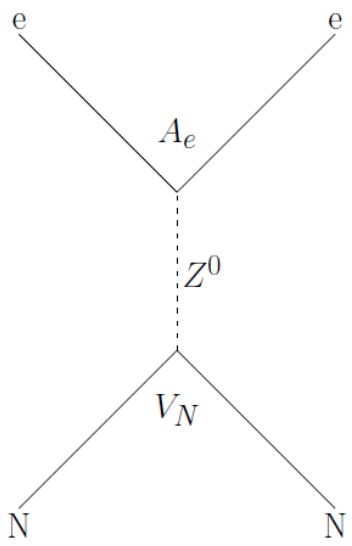

Figure 2.1: Diagram of the nucleon vector current process. Using the vector part of the nucleon-Z^0 vertex makes this process independent of the nuclear spin.

addition to improvements in neutron distribution[50], strong field self-energies and relativistic correction calculations[51]. This brought the measurement into 1σ agreement with the Standard Model.

More recently, further developments in APV calculations[35, 36] have introduced new controversy and, when resolved, have potentially caused the uncertainties in experiments to lag behind the theory. Another measurement in francium, where the APV effect is predicted to be almost $20\times$ larger [52, 53], should reduce experimental uncertainty and could test whether the previous theoretical advancements were correct.

2.1.2 Nuclear spin dependent APV

The nuclear spin dependent component of APNC arises from a trio of interactions: (i) an electron exchanges a Z^0 boson with a nucleon (nucleon axial-vector current), (ii)

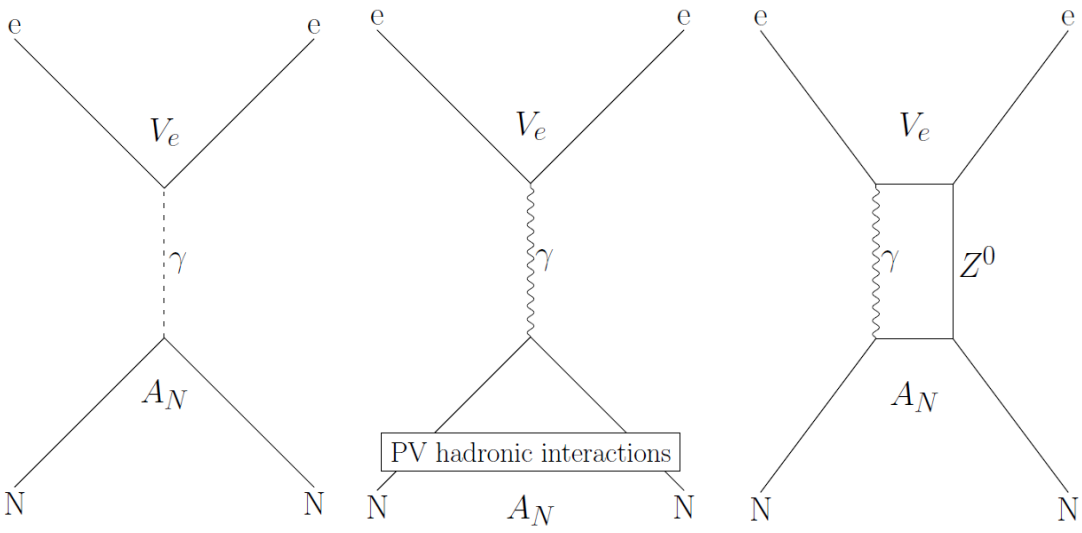

Figure 2.2: (Left) Diagram of the nucleon axial-vector current process. Using the axial-vector part of the nucleon-Z^0 vertex makes this process dependent on the nuclear spin. (Center) Diagram of the anapole (literally, not a pole). The exchange of heavy bosons in the nucleus causes a toroidal current, which interacts with the electron. (Right) Combination of the hyperfine interaction and the spin independent nucleon vector current.

an electron experiences an electromagnetic interaction with a nuclear current generated by weak interaction between nucleons (anapole moment), and (iii) a combination of the hyperfine interaction and spin independent nucleon vector current, see figure 2.2.

The nuclear spin dependent anapole moment, an interaction between the electron and a toroidal current in the nucleus, dominates in heavy atoms ($\propto A^{8/3}$). Detailed calculations suggest it is susceptible to core polarization by the valence nucleons [54, 55]. This suggestion can be tested by a study of isotopes with paired and unpaired neutrons. The large number of accessible francium isotopes makes francium a choice system for these experiments. The anapole moment measurement is also a goal of the Francium Trapping Facility but it is not a topic of this thesis. Further details will

not be provided.

2.2 Stark-induced transitions

Applying a static electric field $\vec{E}$ to an atom mixes its states of opposite parity. Using first order perturbation theory, the $7S_{1/2}$ ground states of francium become:

$$\left|\overline{7S_{1/2}Fm}\right\rangle = \left|7S_{1/2}Fm\right\rangle + \sum_{n,J,F'',m''} \frac{|nP_JF''m''\rangle \langle nP_JF''m''| - e\vec{E}\cdot\vec{r}|7SFm\rangle}{E_{7S} - E_{nP_J}} \quad (2.1)$$

where the bar indicates the perturbed state and F, m are the total angular momentum quantum numbers. The same situation applies to the $8S_{1/2}$ state.

An oscillating electric field $\vec{\epsilon}$ causes a "Stark induced" electric dipole transition with amplitude [56]:

$$\begin{aligned}
A_{Stark} &= \left\langle \overline{8S_{1/2}F'm'} \right| - e\vec{\epsilon}\cdot\vec{r}\left|\overline{7S_{1/2}Fm}\right\rangle \\
&= \left\langle 8S_{1/2}F'm' \right| - e\vec{\epsilon}\cdot\vec{r}\left|7S_{1/2}Fm\right\rangle \\
&+ \sum_{n,J,F'',m''} \frac{\langle 8SF'm'| - e\vec{\epsilon}\cdot\vec{r}|nP_JF''m''\rangle \langle nP_JF''m''| - e\vec{E}\cdot\vec{r}|7SFm\rangle}{E_{8S} - E_{nP_J}} \\
&+ \frac{\langle 8SF'm'| - e\vec{E}\cdot\vec{r}|nP_JF''m''\rangle \langle nP_JF''m''| - e\vec{\epsilon}\cdot\vec{r}|7SFm\rangle}{E_{7S} - E_{nP_J}} \\
&+ \text{second order} \\
&= \vec{\epsilon}\cdot\left\langle 8SF'm'\right| \vec{r}_{\mathit{eff}} \left|7SFm\right\rangle
\end{aligned} \quad (2.2)$$

where the first term is zero by parity conservation. The second order has a factor involving transitions between P states and is also zero by parity conservation. We collect the surviving first order terms together into the effective dipole operator $\vec{r}_{\mathit{eff}}$. Using the principle of irreducible tensor operators, the matrix elements of $\vec{r}_{\mathit{eff}}$ must

have the form [56]:

$$A_{Stark} = \vec{\epsilon} \cdot (\alpha \vec{E} \delta_{F,F'} \delta_{m,m'} + i\beta \langle F'm' | \vec{\sigma} \times \vec{E} | Fm \rangle), \tag{2.3}$$

where $\langle F'm' | \vec{\sigma} \times \vec{E} | Fm \rangle$ is the angular component of the matrix element and α, β are the scalar and vector transition polarizabilities respectively containing radial integrals and spin couplings. The transition polarizabilities are given by:

$$\begin{aligned} \alpha = \frac{1}{6} \sum_n [& \langle 8S || \vec{r} || nP_{1/2} \rangle \langle nP_{1/2} || \vec{r} || 7S \rangle \left(\frac{1}{E_{8S} - E_{nP_{1/2}}} + \frac{1}{E_{7S} - E_{nP_{1/2}}} \right) \\ & - \langle 8S || \vec{r} || nP_{3/2} \rangle \langle nP_{3/2} || \vec{r} || 7S \rangle \left(\frac{1}{E_{8S} - E_{nP_{3/2}}} + \frac{1}{E_{7S} - E_{nP_{3/2}}} \right)], \end{aligned} \tag{2.4}$$

and

$$\begin{aligned} \beta = \frac{1}{6} \sum_n [& \langle 8S || \vec{r} || nP_{1/2} \rangle \langle nP_{1/2} || \vec{r} || 7S \rangle \left(\frac{1}{E_{8S} - E_{nP_{1/2}}} + \frac{1}{E_{7S} - E_{nP_{1/2}}} \right) \\ & + \frac{1}{2} \langle 8S || \vec{r} || nP_{3/2} \rangle \langle nP_{3/2} || \vec{r} || 7S \rangle \left(\frac{1}{E_{8S} - E_{nP_{3/2}}} + \frac{1}{E_{7S} - E_{nP_{3/2}}} \right)]. \end{aligned} \tag{2.5}$$

Using the vector identity:

$$\vec{\epsilon} \cdot (\vec{\sigma} \times \vec{E}) = (\vec{E} \times \vec{\epsilon}\,) \cdot \vec{\sigma}, \tag{2.6}$$

equation 2.3 becomes:

$$\begin{aligned} A_{Stark} &= \alpha \vec{\epsilon} \cdot \vec{E} \delta_{F,F'} \delta_{m,m'} + i\beta \vec{E} \times \vec{\epsilon} \cdot \langle F'm' | \vec{\sigma} | Fm \rangle \\ &= \alpha \vec{\epsilon} \cdot \vec{E} \delta_{F,F'} \delta_{m,m'} + i\beta [(\vec{E} \times \vec{\epsilon})_z \langle F'm' | \vec{\sigma_z} | Fm \rangle \\ &\quad + (\vec{E} \times \vec{\epsilon})_x \langle F'm' | \vec{\sigma_x} | Fm \rangle + (\vec{E} \times \vec{\epsilon})_y \langle F'm' | \vec{\sigma_y} | Fm \rangle]. \end{aligned} \tag{2.7}$$

Changing to the spherical basis where:

$$\begin{aligned}\sigma_z &= \sigma_{10} \\ \sigma_x &= -\frac{1}{\sqrt{2}}(\sigma_{11} - \sigma_{1-1}) \\ \sigma_y &= \frac{i}{\sqrt{2}}(\sigma_{11} + \sigma_{1-1}),\end{aligned} \tag{2.8}$$

produces:

$$\begin{aligned}A_{Stark} = \alpha\vec{\epsilon}\cdot\vec{E}\delta_{F,F'}\delta_{m,m'} + i\beta(\vec{E}\times\vec{\epsilon})_z \langle F'm'|\,\sigma_{10}\,|Fm\rangle \\ - i\beta(\vec{E}\times\vec{\epsilon})_x \langle F'm'|\,\frac{1}{\sqrt{2}}(\sigma_{11}-\sigma_{1-1})\,|Fm\rangle - \beta(\vec{E}\times\vec{\epsilon})_y \langle F'm'|\,\frac{1}{\sqrt{2}}(\sigma_{11}+\sigma_{1-1})\,|Fm\rangle\,.\end{aligned} \tag{2.9}$$

The remaining angular integrals can be calculated with further applications of the Wigner-Eckart theorem. Following the coupling rules results in:

$$\begin{aligned}A_{Stark} = \alpha\vec{\epsilon}\cdot\vec{E}\delta_{F,F'}\delta_{m,m'} + i\beta(\vec{E}\times\vec{\epsilon})_z C_{Fm}^{F'm'}\delta_{m,m'} \\ - i\beta(\vec{E}\times\vec{\epsilon})_x \frac{1}{\sqrt{2}}(C_{Fm'+1}^{F'm'} - C_{Fm'-1}^{F'm'}) - \beta(\vec{E}\times\vec{\epsilon})_y \frac{1}{\sqrt{2}}(C_{Fm'+1}^{F'm'} + C_{Fm'-1}^{F'm'}),\end{aligned} \tag{2.10}$$

where the coefficients $C_{Fm}^{F'm'}$ are the angular integrals.

Transition intensities may then be calculated for specific $7S(F) \rightarrow 8S(F')$ transitions. Note that the scalar polarizability α term is non-zero only for transitions where $F' = F$, so that the ratio of both hyperfine transitions provides a measurement of α/β.

2.3 Isotope shifts

The isotope shift is the variation in the atomic transition energy between isotopes of the same element. It arises due to a combination of nuclear and atomic effects, requiring detailed knowledge of both for accurate predictions. Isotope shifts provide information about the nuclear charge distribution (for examples, see [57, 58]), and are sensitive to electron correlations. They have been employed in the search for space and time variation of the fine structure constant [59] and play a role where accurate spectroscopic information is required, for example when calculating stellar element abundances [60].

Francium, with its high nuclear charge ($Z = 87$) and relatively simple, alkali electronic configuration, has attracted considerable attention as a candidate for fundamental symmetry tests [61, 62, 63]. These investigations require a thorough knowledge of both the atomic and nuclear structure of francium, in particular the overlap of the electronic wavefunctions with the nucleus, to which optical isotope shifts are sensitive. The interpretation of atomic parity non-conservation measurements also relies on accurate many-body theory [64], for which isotope shifts provide benchmarks. Agreement between theory and experiment for the isotope shifts must be achieved before a reliable interpretation of a future parity violation measurement in francium will be possible.

2.3.1 Optical isotope shift theory

In the present work, we measure the optical isotope shift between laser-trapped, cold francium isotopes (see Fig. 2.3). The isotope shift can be separated into two

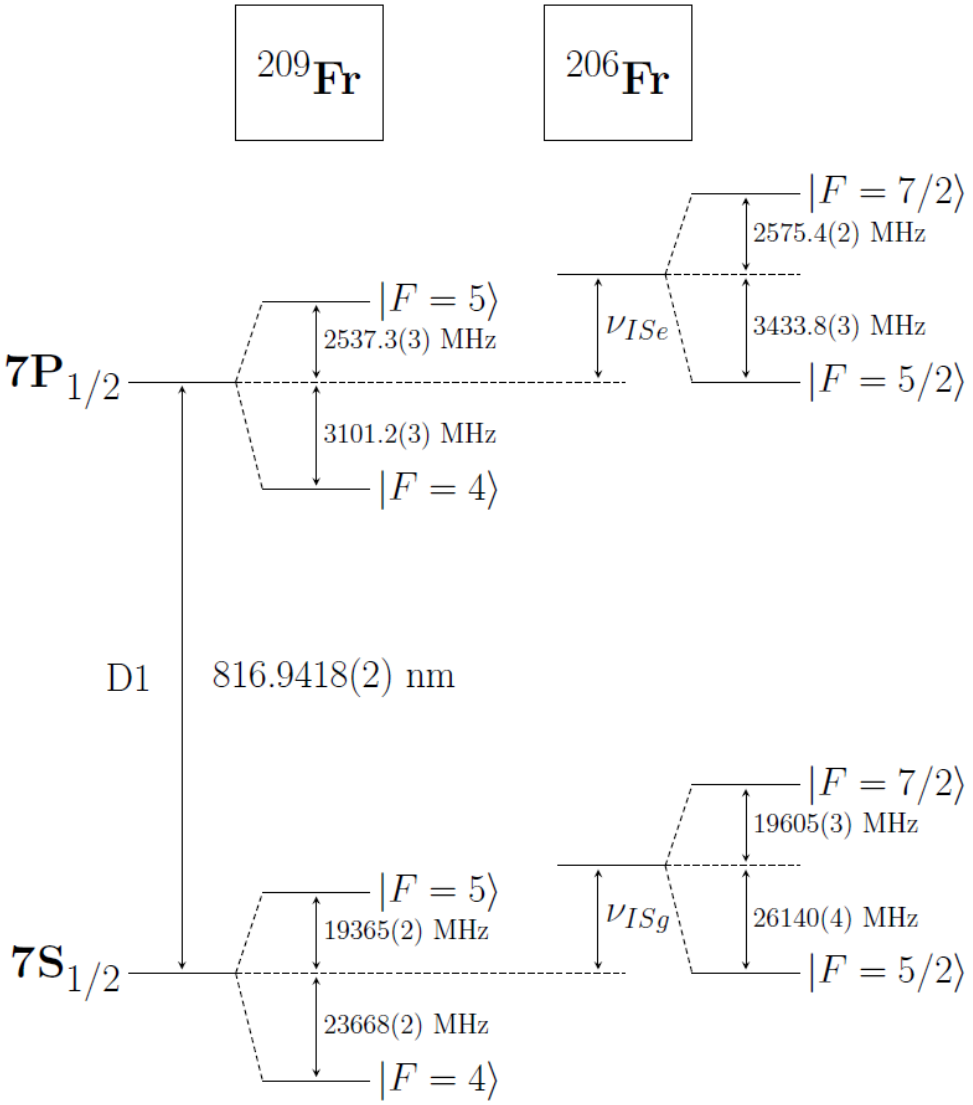

Figure 2.3: Energy level diagram of ^{209}Fr and ^{206}Fr showing the $7s_{1/2}$ and $7p_{1/2}$ levels. The isotope shift of the D1 line is measured between the centers of gravity of the ground and excited states comprising the transition, i.e. the difference between the isotope shifts of those two states (ν_{ISe} - ν_{ISg}).

distinct parts: the field shift, caused by variation in the charge distribution in the nucleus, and the mass shift, caused by the different kinetic energy of the finite-mass nucleus. For a complete treatment of the optical isotope shift, see Ref. [65, 66].

The mass shift comes directly from the changing mass of the nucleus. In the center of mass frame,

$$\Delta E = \mathbf{P}^2/2M = (\sum_i \mathbf{p}_i)^2/2M, \tag{2.11}$$

where M is the nuclear mass, $\mathbf{P}$ is the nuclear momentum and $\mathbf{p}_i$ is the momentum of the ith electron. In all but the lightest of elements, the mass shift can be separated into two parts:

$$\Delta E = \frac{1}{2M}\sum_i {\mathbf{p}_i}^2 + \frac{1}{M}\sum_{i>j} \mathbf{p}_i \cdot \mathbf{p}_j, \tag{2.12}$$

where the first term, the normal mass shift or Bohr reduced mass effect, can be determined exactly, and the second term, the specific mass shift arising from the change in momentum correlations between electrons, is much more difficult to calculate. In the lightest elements, where the mass shift dominates the field shift, the proportionately large normal mass shift has a significant effect on the electron correlations of the specific mass shift. In heavy francium, this is not the case and the mass shift is separable.

Isotope shifts are measured with respect to a reference isotope. The contribution of the normal mass shift to the frequency shift of an optical transition is [65]:

$$\delta\nu_{NMS}^{AA'} = \nu(A')\frac{m_e(M_A - M_{A'})}{M_{A'}(M_A + m_e)}, \tag{2.13}$$

where $\nu(A')$ is the transition frequency of the reference isotope with mass number A', $M_A(M_{A'})$ is the nuclear mass of the measured (reference) isotope and m_e is the mass of the electron, which can be neglected in the denominator. The mass term comes from the difference in the reduced masses of the two isotopes. Electron correlations for the specific mass shift must be very well known in order to check the theoretical

models used to extract, e.g., the time variation of α [59]. Francium, as the heaviest alkali, is more tractable than multi-valence electron systems like lead, making it very suitable for testing calculations. Together, the total mass shift $\delta\nu_{MS}$ between isotopes of mass numbers A and A', and following the form of eq. 2.13, can be written as:

$$\delta\nu_{MS}^{AA'} = (N+S)\frac{M_A - M_{A'}}{M_A M_{A'}}, \tag{2.14}$$

where N, S are the normal and specific mass shift constants.

The field shift is due to the modification of the point-charge Coloumb potential by a finite-size nucleus. This results in a contraction of the spacings between electronic bound state energies of an atom. The contraction is isotope dependent so that there is a difference in the transition frequency between isotopes:

$$\delta\nu_{\mathrm{FS}}^{AA'} = F\delta\langle r^2\rangle^{AA'}, \tag{2.15}$$

where $\delta\langle r^2\rangle^{AA'}$ is the difference in the mean nuclear charge radii squared of the two isotopes. The field shift constant F for a particular atomic transition is:

$$F = -\frac{\pi a_0^3}{Z}\Delta|\psi(0)|^2 f(Z), \tag{2.16}$$

where $\Delta|\psi(0)|^2$ is the change of the electron charge density at the nucleus between the states involved in the transition and $f(Z)$ is an increasing function of Z that accounts for relativistic and nuclear shape corrections.

The sum of mass and field shifts gives the total isotope shift:

$$\delta\nu_{IS}^{AA'} = (N+S)\frac{M_A - M_{A'}}{M_A M_{A'}} + F\delta\langle r^2\rangle^{AA'}, \tag{2.17}$$

which we measure in our experiment, and compare to theoretical predictions. Neglecting the isotope-dependent nuclear effects considered later, the isotope shift of a

transition, e.g. the D1, is the difference in the isotope shifts of the states involved:

$$\delta\nu_{IS,D1}^{AA'} = (N_{D1} + S_{D1})\frac{M_A - M_{A'}}{M_A M_{A'}} + F_{D1}\delta\langle r^2\rangle^{AA'}, \tag{2.18}$$

where the field shift constant is $F_{D1} = F(7S_{1/2}) - F(7P_{1/2})$, and likewise for the normal and specific mass shift constants.

Isotope shifts from two transitions can be combined with the isotope masses to produce a King plot [65]. The two isotope shifts are plotted against one another, allowing a separation of the field shift from the mass shift and thus an independent comparison of each to theory. More details are provided in section 4.4, following the analysis of our isotope shift measurements.

2.3.2 Higher-order corrections to the field shift

Now we will examine the field shift in greater depth, following the framework set out in [67], to observe any isotope dependence of the field shift constant F. Beginning with two isotopes and writing the spherical averages of their nuclear charge distributions as $\rho(r)$ and $\rho(r) + \delta\rho(r)$, the potential experienced by an electron in the fields set up by these distributions are $V(r)$ and $V(r) + \delta V(r)$ respectively. The energy change between these two is then given by first order perturbation theory:

$$\delta E^{(1)} = F, \tag{2.19}$$

where

$$F = e\int_0^\infty (P^2(r) + Q^2(r))\delta V(r)dr \tag{2.20}$$

where F is the field shift constant of equation 2.15, with $P(r), Q(r)$ being the large and small radial Dirac functions of the valence electron in potential $V(r)$. Thus we

need to know the electronic functions only where $\delta V(r) \neq 0$. At this point, two approximations are applied; the binding energy of the electron within the nucleus and the contributions of the core electrons to the potential are both neglected; the electron is treated as a single, independent, free electron as it enters the nuclear charge distribution. Thus the form of the wavefunction only depends on the shape of the nuclear charge distribution. It can be separated into a function that depends only on the nuclear potential at small r and a normalization factor, which accounts for, among other things, the long range details of the potential:

$$F = N\Lambda, \tag{2.21}$$

where

$$\Lambda = e\int_0^\infty f(r)\delta V(r)dr \tag{2.22}$$

and $f(r)$ only depends on the nuclear charge distribution. N is the "volume (probability) density of the electron at the origin", also written as $|\psi(0)|^2$.

The electronic function $f(r)$ is approximated as a polynomial over the range of the nucleus, following the work in [68]:

$$f(r) \approx \tilde{f}(r) = \sum_{n=2}^{n'} h_n r^n. \tag{2.23}$$

Coefficients h_n are determined to accurately represent $f(r)$, if the order, set by the value of n', is high enough. In practice, only a few terms are required for smaller errors in F than a first-order perturbation theory calculation[67]. The change in the nuclear potential between isotopes can be written as:

$$\delta V(r) = \frac{-e}{4\pi\epsilon_0}\int \frac{\delta\rho(r')}{|r-r'|}d^3r', \tag{2.24}$$

and then the integral Λ containing the part that depends on the nuclear distribution becomes:

$$\Lambda = \frac{2\pi}{3}\left(\frac{Ze^2}{4\pi\epsilon_0}\right)\sum_{n=2}^{n'} S_n \delta\langle r^n\rangle, \tag{2.25}$$

with the Seltzer coefficients:

$$S_n = [6/n(n+1)](h_n/h_2) \tag{2.26}$$

and mean order charge radii:

$$\langle r^n\rangle = \frac{\int \rho(r) r^n r^2 dr}{\int \rho(r) r^2 dr}. \tag{2.27}$$

The Seltzer coefficients tell the magnitude of the contributions of the higher order moments. As with equation 2.23, only a few are needed for an accurate result.

This gives us a relation between the earlier polynomial fitting the charge distribution and the coefficients of these changes in nuclear moments $\delta\langle r^n\rangle$. Then we define the so-called Seltzer moments:

$$\lambda = \sum_{n=2}^{n'} S_n \delta\langle r^n\rangle, \tag{2.28}$$

and note that, according to equation 2.26, $S_2 = 1$ means that the leading term is simply $\delta\langle r^2\rangle$. Finally, going back to the observed energy shift, we have the expression:

$$\delta E^{(1)} = kN\lambda, \tag{2.29}$$

where

$$k = \frac{2\pi}{3}\left(\frac{Ze^2}{4\pi\epsilon_0}\right) \tag{2.30}$$

is simply a collection of constants from the expression for Λ.

Writing these equations in a more familiar form using the isotope shifts in section 2.3.1 and later in chapter 4 shows the first-order perturbation energy shift is:

$$\delta E = \frac{2\pi}{3}\left(\frac{Ze^2}{4\pi\epsilon_0}\right)|\psi(0)|^2 \sum_{n=2}^{n'} S_n \delta\langle r^n\rangle. \tag{2.31}$$

The Seltzer moments can be written as:

$$\sum_{n=2}^{n'} S_n \delta\langle r^n\rangle = \delta\langle r^2\rangle(1 + \sum_{n=4}^{n'} S_n \frac{\delta\langle r^n\rangle}{\delta\langle r^2\rangle}), \tag{2.32}$$

where we have pulled the first order $\delta\langle r^2\rangle$ out front. Then the energy shift can be written as the familiar expression:

$$\delta E = \frac{2\pi}{3}\left(\frac{Ze^2}{4\pi\epsilon_0}\right)|\psi(0)|^2 \delta\langle r^2\rangle K, \tag{2.33}$$

where the term

$$K = 1 + S_4 \frac{\delta\langle r^4\rangle}{\delta\langle r^2\rangle} + S_6 \frac{\delta\langle r^6\rangle}{\delta\langle r^2\rangle} + ... \tag{2.34}$$

is to correct for nuclear shape. We collect terms together to produce:

$$\delta E = F \delta\langle r^2\rangle K, \tag{2.35}$$

and call F the field shift constant. This division can be confusing as, e.g., [64] combines what is here F with K and reports calculations of the one quantity F. This is natural for their numerical calculations: they choose a nuclear potential and compute from there. Here, F and K are kept separate as the first is a purely electronic quantity and hence *should not* change between isotopes, whereas K *does* change between isotopes, as demonstrated shortly.

The Seltzer coefficients S_n take different values for S and P states. Discussion of their magnitudes and corrections due to the polynomial approximation 2.23 are presented in [67], but are beyond the scope of this work.

Equation 2.35 is the energy shift for a single electronic state. What we measure is a transition between two of these. Thus, what we require is, for transition a between states 1 and 2, with $E_2 > E_1$:

$$\begin{aligned}\delta E_a &= \delta E_2 - \delta E_1 \\ &= F_2\delta\langle r^2\rangle K_2 - F_1\delta\langle r^2\rangle K_1 \\ &= (F_2K_2 - F_1K_1)\delta\langle r^2\rangle.\end{aligned}$$

For two transitions between 3 states, which will be used to make the King plot in chapter 4, and including the mass shift constants N, S and mass factor $g^{AA'} = AA'/A - A'$:

$$\delta E_a = (N_a + S_a)/g^{AA'} + (F_2K_2 - F_1K_1)\delta\langle r^2\rangle, \tag{2.36}$$

$$\delta E_b = (N_b + S_b)/g^{AA'} + (F_3K_3 - F_1K_1)\delta\langle r^2\rangle. \tag{2.37}$$

Combining them to eliminate $\delta\langle r^2\rangle$ produces:

$$g^{AA'}\delta E_b = (N_b + S_b) - \frac{F_3K_3 - F_1K_1}{F_2K_2 - F_1K_1}(N_a + S_a) + \frac{F_3K_3 - F_1K_1}{F_2K_2 - F_1K_1}g^{AA'}\delta E_a, \tag{2.38}$$

the King plot equation with slope dependent on the field shift constants, with the nuclear corrections, and intercept dependent on the mass shift constants.

2.3.3 Isotope dependence of K

Nuclear structure effects are contained within the term K, which is isotope dependent. The form of K depends on the model used for the nuclear charge distribution [69]. This point can be illustrated by going through the formalism with the liquid

drop model. Other models for the nuclear charge distribution are equally valid but the simple liquid drop model seems appropriate for the spherical francium isotopes just below the neutron shell closure at $N = 126$.

For $\langle r^m \rangle$ over the nucleus, with radius R, recall from equation 2.27:

$$\begin{aligned}\langle r^m \rangle &= \frac{\int_0^R r^m r^2 dr}{\int_0^R r^2 dr} \\ &= \frac{\frac{1}{m+3} r^{m+3}|_0^R}{\frac{1}{3} r^3|_0^R} \\ &= \frac{3}{m+3} R^m,\end{aligned}$$

so then

$$\delta\langle r^m \rangle = \frac{3}{m+3} m R^{m-1} \delta R. \tag{2.39}$$

In the nuclear distribution for the chosen liquid drop model, $R = r_0 A^{1/3}$, and thus $\delta R = \frac{r_0}{3} A^{-2/3} \delta A$, so that:

$$\delta\langle r^m \rangle = \frac{3m}{m+3} R^{m-1} (\frac{r_0}{3} A^{-2/3}) \delta A. \tag{2.40}$$

Note that:

$$R^{m-1} = \frac{R^m}{r_0 A^{1/3}}, \tag{2.41}$$

then

$$\delta\langle r^m \rangle = \frac{3m}{m+3} \frac{R^m}{r_0 A^{1/3}} (\frac{r_0}{3A^{2/3}}) \delta A, \tag{2.42}$$

and

$$R^m = \frac{m+3}{m} A \frac{\delta\langle r^m \rangle}{\delta A}. \tag{2.43}$$

To obtain the first two terms of interest in equation 2.34 for our nuclear correction K:

$$R^2 = \frac{5}{2} A \frac{\delta\langle r^2 \rangle}{\delta A} \rightarrow \delta\langle r^2 \rangle = \frac{2}{5} R^2 \frac{\delta A}{A}, \tag{2.44}$$

$$\delta\langle r^4\rangle = \frac{4}{7}R^4\frac{\delta A}{A}, \tag{2.45}$$

so then

$$\frac{\delta\langle r^4\rangle}{\delta\langle r^2\rangle} = \frac{25}{7}A\frac{\delta\langle r^2\rangle}{\delta A}. \tag{2.46}$$

Likewise

$$\frac{\delta\langle r^6\rangle}{\delta\langle r^2\rangle} = \frac{125}{12}A^2(\frac{\delta\langle r^2\rangle}{\delta A})^2. \tag{2.47}$$

The coefficients S_4, S_6 are taken from [69] based on calculations in [68], where they are written as C_2/C_1 and C_3/C_1. They follow simple, monotone dependence on the atomic number Z:

$$S_4 = \frac{C_2}{C_1} = -1.04\times10^{-5}Z - 4.07\times10^{-8}Z^2 = -1.04\times10^{-5}Z\phi(Z), \tag{2.48}$$

where $\phi(Z) = 1. + 3.91\times10^{-3}Z$, and

$$S_6 = \frac{C_3}{C_1} = 3.73\times10^{-8}Z. \tag{2.49}$$

With that we now have an expression for K, for the nuclear charge distribution based on the liquid drop model:

$$K_{\mathrm{LDM}} = 1 - 3.71\times10^{-5}ZA\frac{\delta\langle r^2\rangle}{\delta A}\left(\phi(Z) - 1.05\times10^{-2}A\frac{\delta\langle r^2\rangle}{\delta A}\right). \tag{2.50}$$

The slope $\delta\langle r^2\rangle/\delta A$ is obtained from measurements of the charge radii. A simple model such as this does not account for anything that would cause the obvious kinks at, e.g., shell closures or sudden onsets of deformation. For francium, these charge radii are extracted from isotope shift measurements using static field shift constant values. Thus the absolute accuracy may be unknown, but the model should still give an idea of the magnitude of this correction.

One final consideration is the difference between S and P states. The value of K is dependent on the state of the electron. All of the work in [69] is for $S_{1/2}$ electrons, since those are the most important for calculating field shifts due to their large overlaps with the nuclear charge distribution, and hence their large F values. Thus the evaluation of K for an $S_{1/2}$ electron is to simply apply the above expression. Other electronic states are not so simple.

The difference in K values for other states comes from the S_n values, none of which are explicitly calculated for the P states. What is given is the ratio between Seltzer moments λ (from equation 2.28) for $S_{1/2}$ and $P_{1/2}$ electrons using the nuclear model of a uniformly charged, incompressible sphere, i.e., the liquid drop model [67]:

$$\frac{\lambda_S - \lambda_P}{\lambda_S} \sim 3 \times 10^{-3} \tag{2.51}$$

showing that there is little difference in this nuclear correction for the S and P states with $J = 1/2$.

As for the $P_{3/2}$ electrons, they are rarely mentioned in the literature. Typically, they are neglected in isotope shift calculations since the wavefunction is zero at the origin. However, we know that they play some role in the isotope shifts for francium; if we do not include their contribution to the field shift, then the constant ratio F_{D2}/F_{D1} predicted from theory does not match our King plot, which is displayed in chapter 4. That said, with no means to evaluate their contribution, and with the understanding that $P_{3/2}$ electron wavefunctions vanish at the origin, we will neglect them for the nuclear correction term K.

2.4 Summary

We have briefly explored the origin of the parity-violating effects in atoms, showing the dominant nuclear spin independent Z^0 exchange between nucleons and electrons that is parameterized in the weak charge Q_W. The nuclear spin dependent weak interactions were also shown but are not a topic of this thesis. Stark-induced transitions were explored, showing how the applied electric field mixes states of opposite parity, allowing otherwise highly-forbidden transitions to occur with a measureable amplitude. Isotope shifts were discussed in detail, with greater focus given to the field shift, which dominates in heavy atoms. Finally, attention was given to higher-order corrections to the field shift, with the case of an isotope dependent correction being shown based on the liquid drop model of the nuclear charge distribution.

Chapter 3

The Francium Trapping Facility

3.1 Introduction

Francium has no stable isotopes. The longest lived one, ^{223}Fr, has a half-life of 22 minutes. Thus it must be produced online at an accelerator facility. TRIUMF, Canada's national laboratory for particle and nuclear physics, has repeatedly demonstrated large francium yields from their uranium carbide targets. However, these relatively large yields, high rates by radioactive beam standards, are still orders of magnitude below those of the thermal beams produced from stable species. Therefore, we employ a magneto-optical trap in order to collect a sufficient amount of short-lived francium for precision measurements.

This chapter will detail the facility where we trap francium. All aspects of beam production and delivery up to the point of Fr^+ ions entering the FTF are the responsibility of TRIUMF and will only briefly be described. The rest of our apparatus, inside the laboratory, will receive more attention. Much of the development of the appara-

tus has been done using rubidium for testing. This is a great advantage as our time with francium is limited by target availability and the demand by other experiments at TRIUMF. The wavelengths involved in trapping both rubidium (780 nm and 795 nm) and francium (718 nm and 817 nm) are accessible by Ti:sapphire lasers, making it relatively simple to change between the two. Many of the atomic properties of the systems are similar as well, such as saturation intensities and Zeeman shifts, so that many systematic tests can be done in rubidium.

3.2 Francium production

TRIUMF, located in Vancouver, British Columbia, houses the largest negative ion cyclotron in the world. Francium is produced by spallation of 480 MeV ($\frac{3}{4}c$) protons on a thick ($\sim$13 g/cm^2) uranium carbide (UCx) target in the Isotope Separation and Acceleration (ISAC) facility, where the FTF is located. Atoms diffuse out of the target material before effusing along the target container to a hot ($\sim$ 2200°C) rhenium-coated tantalum ionizer tube. Here the atoms are surface ionized prior to being accelerated to $\sim$20 keV, mass-selected through a pair of magnetic dipoles, and transported to the FTF. ISAC delivers an isotope dependent maximum 10^9 ions per second, and figure 3.1 shows the yields for each isotope. Although isobaric contaminants, e.g. radium, may be delivered alongside the desired isotope, anything other than that isotope will not be trapped by the specific laser frequencies employed in the optical trap.

The low-energy beamlines in ISAC, held under high vacuum, conduct the francium ions to the FTF through a series of electrostatic steering and focusing ion optics.

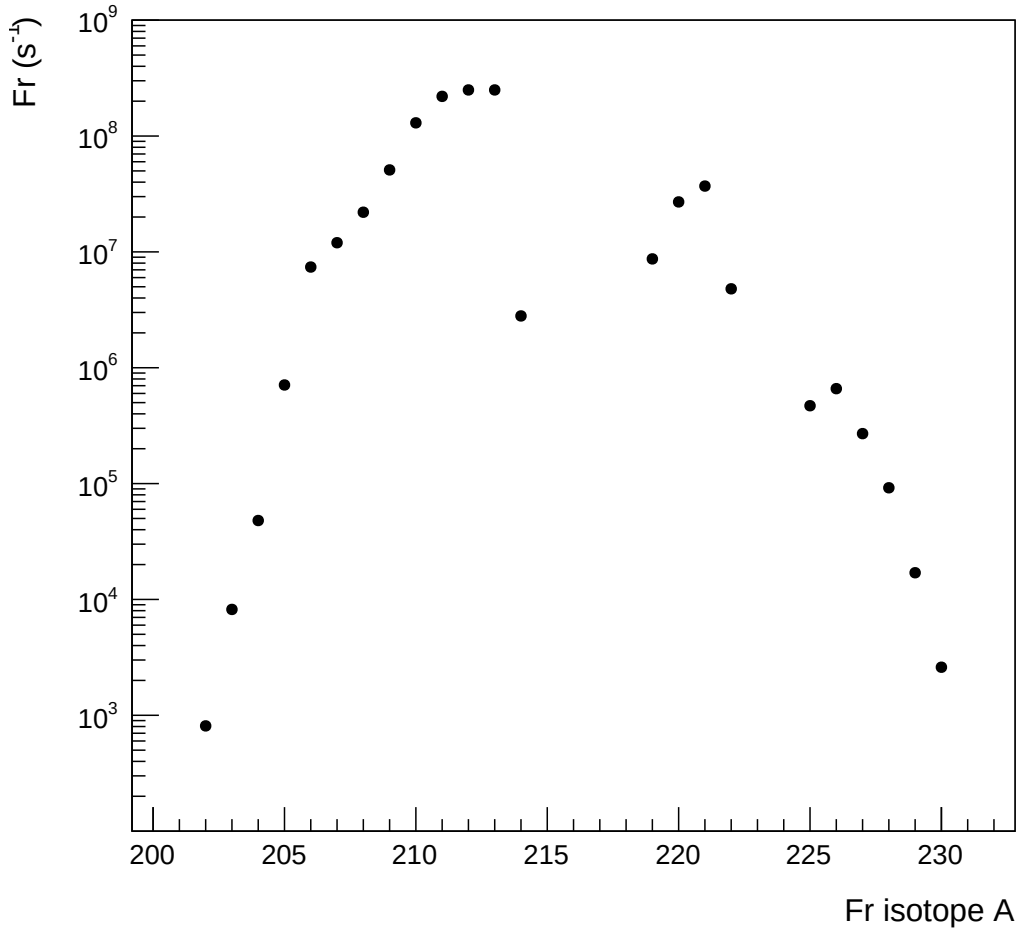

Figure 3.1: Francium ion yields reported at the ISAC yield station for the September 2013 UCx target, operated at 8 μA of protons. Other targets have been operated at 2-9.8 μA of protons with yields scaled accordingly and showing the same trends.

These optics are controlled by the ISAC operators who are responsible for steering the requested francium isotope to us during an experiment period. Tuning is accomplished by steering the ion beam through various collimators to the final Faraday cup in our apparatus. The currents from these diagnostics are read out for the operators, and they tune the beam using the upstream steerers.

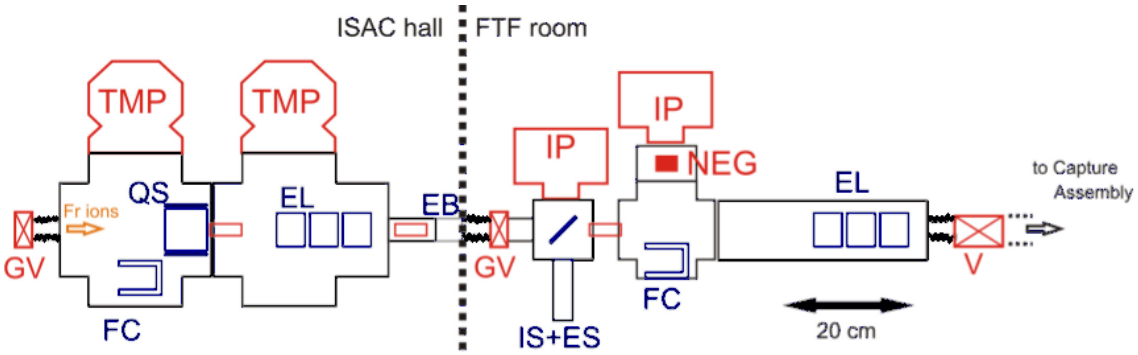

Figure 3.2: Overview of the ISAC beamline leading to the capture assembly in the FTF [70]. The abbreviations used in the figure are as follows: (G)V (gate) valve, TMP turbomolecular pump, FC retractable Faraday cup, QS quadrupole elements and electrostatic steerer, EL Einzel lens, EB electronic break (isolates inside the FTF from ISAC beamline ground), IP ion pump, IS+ES ion source + retractable electrostatic mirror, NEG non-evaporative getter cartridge. The vacuum system is colour-coded in red while the beam delivery is blue. The capture assembly is the vacuum chamber containing the yttrium neutralizer foil and is to the right of the final valve. Bellows are depicted as staggered lines and link different parts of the beamline, isolating them from vibrations.

The last pair of focusing optics (Einzel lenses) depicted in figure 3.2 are inside the FTF wall and under local control. This allows us to focus the ion spot optimally on the neutralizer foil using the trap as a diagnostic. Additionally, figure 3.3 shows the α-particle detector (Hamamatsu S3590-09 silicon photodiode) we have placed to capture the charged particles produced in francium radioactive decays. The α-particle detector is beside the Faraday cup, but not looking into the beam, with a solid angle of ~ 0.176 sr (1.4%) visible from the center of the cup. Counts at this detector rise when the neutralizer is raised and exponentially decay when the neutralizer blocks the ion beam, giving us another beam diagnostic and means of isotope identification through decay lifetimes (see figure 3.4).

3.2.1 Ion neutralization

The francium ions are delivered to the capture assembly shown in figure 3.3 where they accumulate in a 25 μm thick yttrium neutralizer foil that is rotated and heated to release neutral francium atoms for trapping. Yttrium is selected for its low work function, ensuring efficient release of neutral atoms from the foil. The foil is heated with a $\sim$9 A current for 1 s to no more than 700 ^{o}C, causing the now neutral atoms to emerge and enter the trapping volume on a 20 s cycle. A Kepco ATE 25-20, a unipolar, stabilized linear power supply, operating in current limited mode provides the current. Our first commisionning run achieved a $\sim 2.5 \times 10^5$ atom trap with lifetime > 10 s for ^{209}Fr. This is an initial population before trap losses and radioactive decays reduce that number in the time between yttrium heating pulses. The trap lifetime is mainly determined by the rate of collisions with background gas ejecting atoms from the trap; our typical vacuum pressure of a few times 10^{-10} Torr gives a trap lifetime of a few tens of seconds. Radioactive decay also removes atoms from the trap, however that is only a concern for the shorter half-life isotopes. The MOT population will differ between isotopes mainly due to the different ion beam yields delievered to us by ISAC; the yields and some other basic isotopic information are provided in appendix E.

The rotation of the neutralizer assembly is accomplished by a pneumatic actuator on a bellows feedthrough into the vacuum chamber. Our control program dictates the sequence of triggering the actuator and the neutralizer heating current, set so that the neutralizer rotation is complete before heating commences. There is a timer interlock on the heating current to ensure that a control program entry mistake or

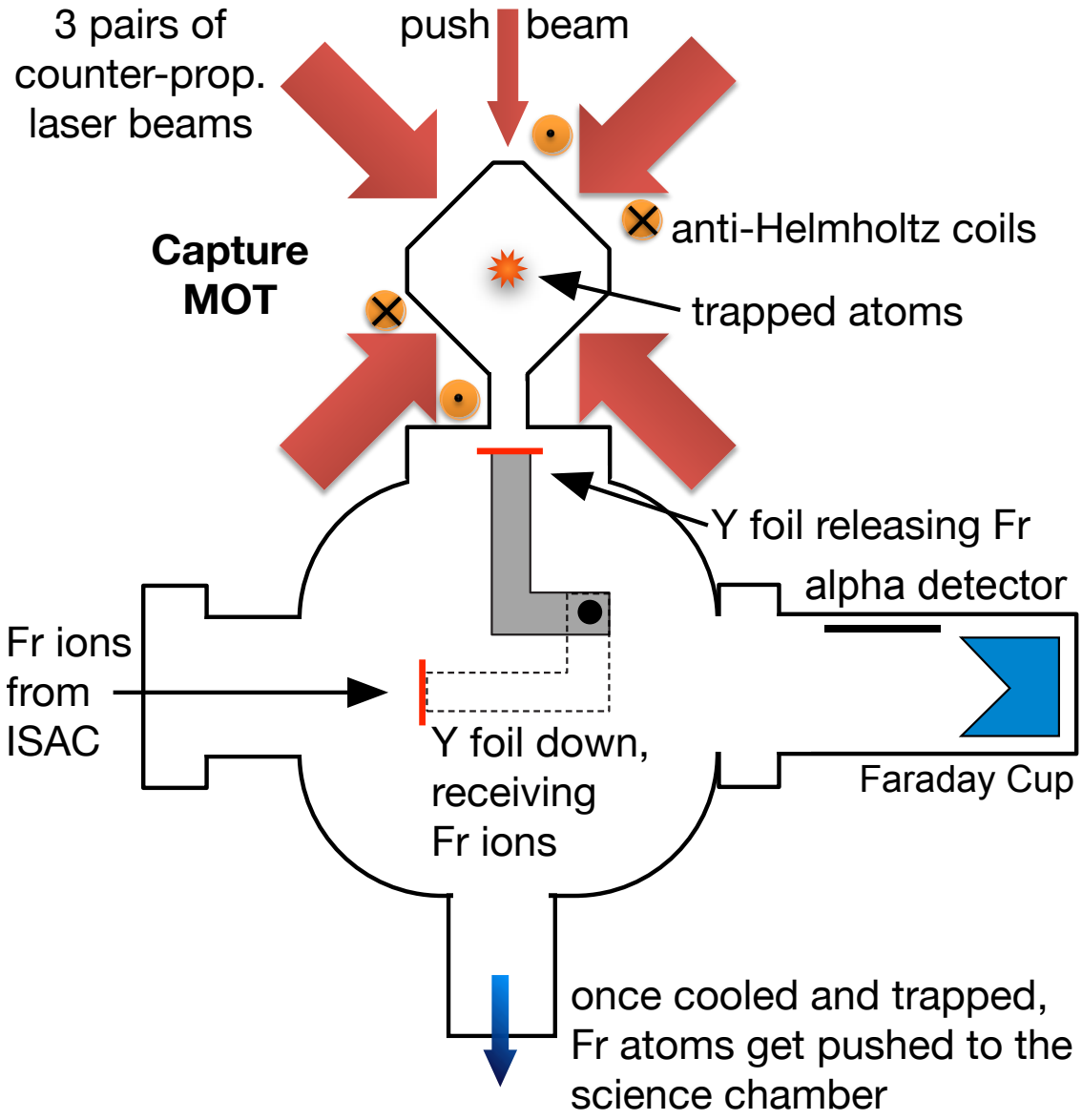

Figure 3.3: Schematic diagram of the upper vacuum chamber showing the capture assembly, Faraday cup and MOT cube. Fr ions delivered by ISAC implant into the Y foil where they are neutralized. The foil assembly is rotated and heated to release Fr atoms into the top glass bulb where they are cooled and confined in a MOT. With the neutralizer in the raised position, the ion beam terminates in the Faraday cup where activity is recorded by the α-particle detector.

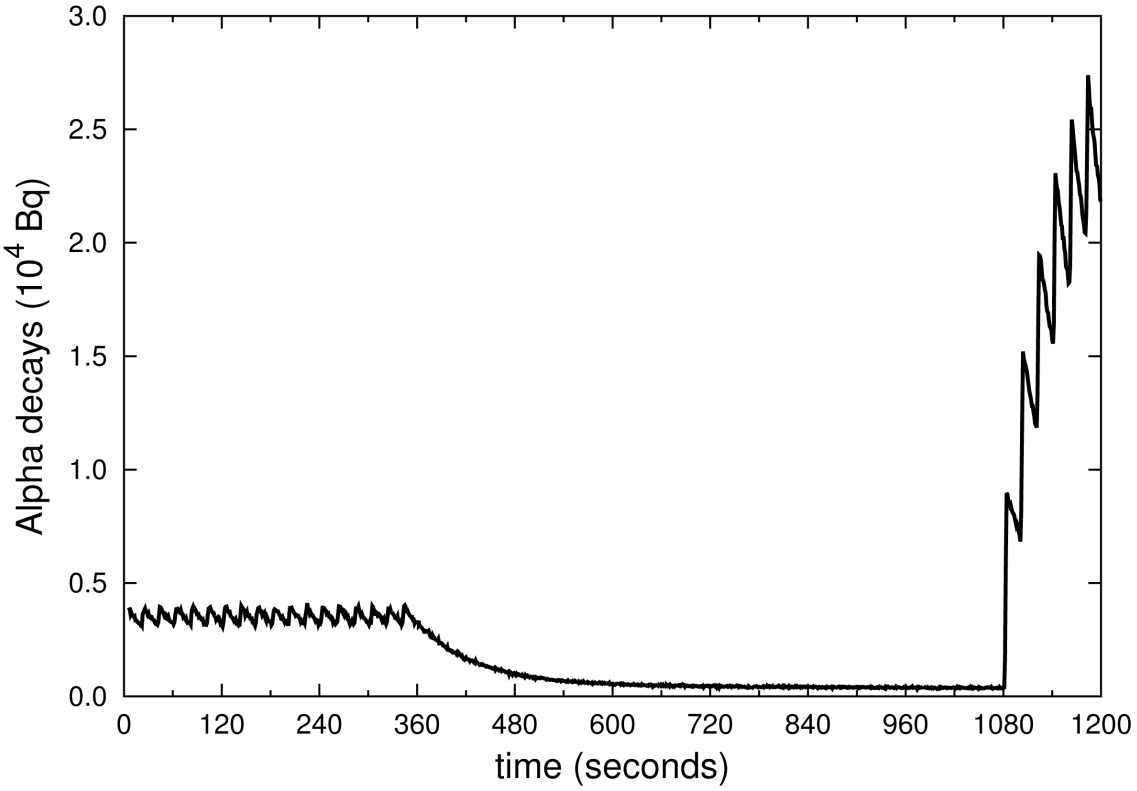

Figure 3.4: Signal from the α-particle detector showing neutralizer operation [70]. Initially, ^{207}Fr is being trapped. This is followed by a period of no beam as an isotope change is made by the ISAC operators. Finally, the higher yield ^{209}Fr is delievered to the apparatus. Note the pulsed nature of the signal; counts rise only when the neutralizer is rotated upwards, exposing the Faraday cup to the ion beam. The ^{209}Fr counts are increasing between pulses as the activity on the Faraday cup rises to equilibrium.

failure does not keep the current on for too long, which could destroy the neutralizer foil. Details of the timer interlock are provided in appendix C.

3.3 Francium magneto-optical trap

The Francium Trapping Facility employs a magneto-optical trap (MOT) to cool and collect sufficient francium atoms for high precision measurements. The densities

we achieve allow measurements comparable to those possible with the massive thermal beams available for stable species.

A MOT is a hybrid neutral atom trap consisting of both laser light and magnetic fields. When an atom absorbs a photon, it recoils due to the momentum of the photon $\vec{p} = \hbar\vec{k}$, and by conservation of momentum this is in the direction of propagation of the light. The emission of the photon, which can be in any direction, leads to a randomly directed recoil, which means the contribution from many emissions averages to zero. Thus the atom experiences a net force from many absorptions of laser photons. A MOT is constructed such that the force on the atom tends to be opposed to its direction of motion, both slowing it, and directed towards the center of the trap. The MOT consists of counterpropagating laser beams tuned near specific atomic resonances directed to three mutually perpendicular axes along with a quadrupole magnetic field. Combined, these provide the slowing and restoring forces of the MOT.

The slowing force is accomplished by tuning the MOT trapping lasers to a frequency several atomic linewidths below a cycling transition in the atom (red detuned), so that atoms moving counter to the propagation direction are Doppler shifted onto resonance, see figure 3.5. Conversely, atoms moving with the light are Doppler shifted even further from resonance. Thus, there is preferential absorption from the correct laser beams, and the atoms are slowed. With laser beams along three perpendicular axes, all atoms are cooled, or slowed.

The spatially dependent force which restores atoms to the center of the trap is made possible by the exploitation of angular momentum selection rules. All of the MOT laser beams are circularly polarized and carry angular momentum. Consider

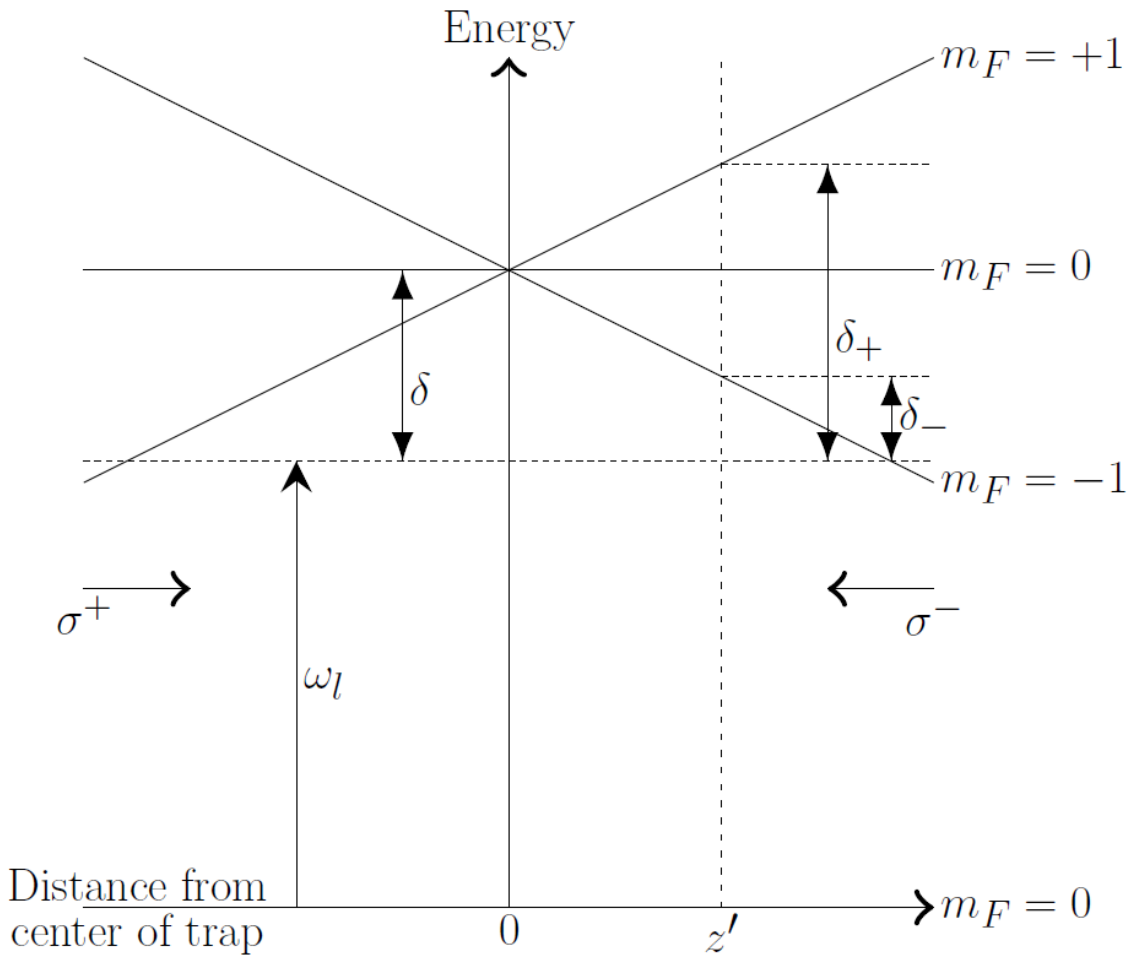

Figure 3.5: Energy levels in a 1D MOT for a simple atom with $F = 0$ ground state and $F = 1$ excited state utilized for trapping. The quadrupole magnetic field has $B = 0$ in the center and the laser frequency (ω_l) is detuned δ below the trapping resonance (to the dashed line where $B = 0$). The excited states are split by the magnetic field into $m_F = 0, \pm 1$ components, which are selectively excited by the specifically polarized beams from the $m_F = 0$ ground state. Atoms at $z = z'$ are closer to resonance with the σ^- beam and are forced towards the center.

two counterpropagating beams with the same helicity; one, with polarization σ^+ as viewed by the atom, will only excite $|F, m_F\rangle \rightarrow |F + 1, m_F + 1\rangle$ transitions. The other, with the same helicity but opposite direction, has polarization σ^- and will only excite $|F, m_F\rangle \rightarrow |F - 1, m_F - 1\rangle$ transitions.

The quadrupole magnetic field generated from a pair of anti-Helmholtz coils has radial and axial field profiles which increase linearly with distance from the center of the trap. In the presence of the magnetic field, the hyperfine sublevels m_F are no longer degenerate. They are split by the linear Zeeman effect at low fields, proportional to the field strength:

$$\Delta E = g_F \mu_B m_F B, \tag{3.1}$$

where g_F is the Landé g-factor, μ_B is the Bohr magneton and B is the applied field. Thus, the $m_F = +1$ level in figure 3.5 increases in energy with increasing field while the $m_F = -1$ level decreases. The differences in the energies of the levels and the laser, called the detunings $\delta_\pm$, are position dependent. At position z', level $m_F = -1$ is closer to the laser frequency than level $m_F = +1$, resulting in more absorptions from the σ^- beam and a net force towards the $B = 0$ center.

There is one more essential component to a MOT. Atoms are more complicated than the simple picture used in figure 3.5. The presence of additional states, such as multiple hyperfine ground states, means that electrons can populate states that are not in resonance with the trapping lasers, and the atoms are then lost to the trap. This effect is countered in two ways. First, trapping lasers are tuned to cycling transitions. A cycling transition is one where the excited atom can only decay to the state it was excited from. Consider that σ^+ light excites a $|F, m_F\rangle \rightarrow |F+1, m_F+1\rangle$ transition. With the selection rule $\Delta F = 0, \pm 1$, if there is no $|F+1\rangle$ ground state, the atom must decay back to the $|F, m_F\rangle$ state. For example, ^{209}Fr is an alkali atom with nuclear spin $I = 9/2$. As illustrated in figure 3.6, its $7S_{1/2}$ ground state is split into $F = 4, 5$ hyperfine states and its $7P_{3/2}$ excited state has $F = 3, 4, 5, 6$ hyperfine

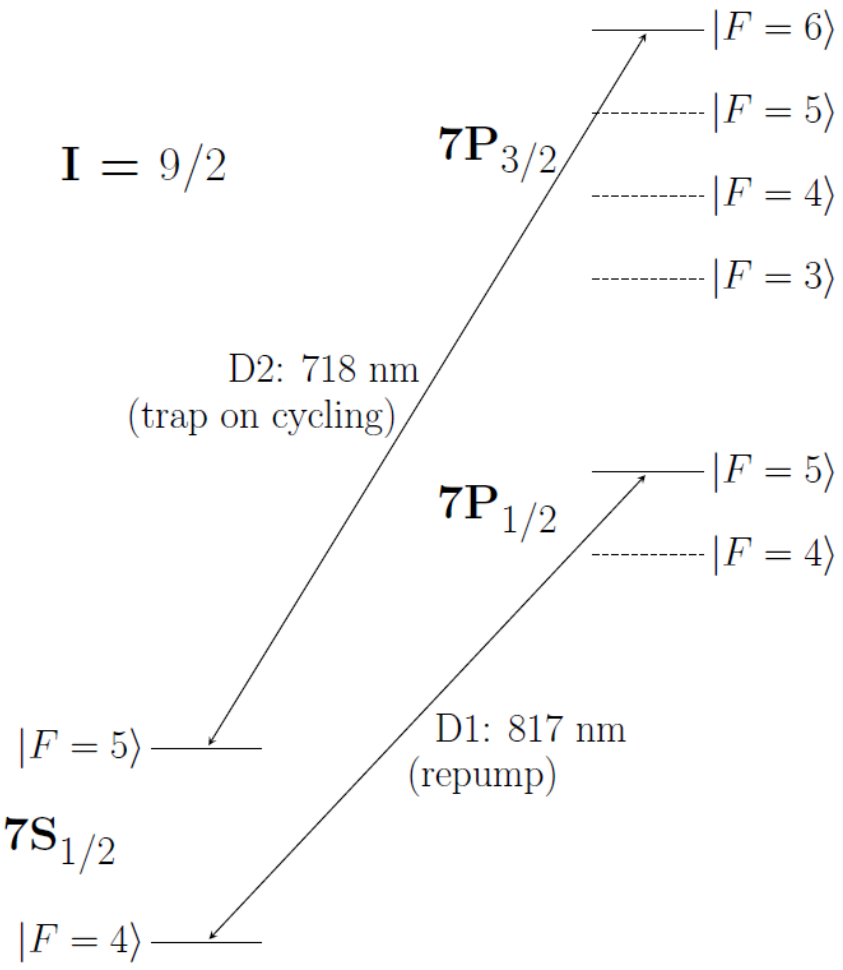

Figure 3.6: Energy level diagram of an $I = 9/2$ alkali, i.e. ^{209}Fr, showing the D1 and D2 transitions to the $7S_{1/2}$ and $7P_{3/2}$ levels, respectively. The trapping laser is tuned to a cycling transition on the D2 line. The repump laser is tuned to any transition whose upper state can decay to the upper hyperfine ground state; here, it is on the D1 transition but D2 transition repumping is also possible.

states. We tune the laser to the $|F = 5\rangle \rightarrow |F = 6\rangle$ D2 transition and the atoms will cycle (almost) exclusively between those two states.

However, there remains a small probability of a transition to the $F = 5$ excited state occuring due to the Lorentzian width of the state. This probabilty is dependent on the detuning, hyperfine splitting and lifetime of the excited state. Atoms in this

excited state may decay to another hyperfine ground state, a so-called dark state that is out of resonance with the trapping laser, and are thereby lost to the trap. The large hyperfine splittings of francium compared to, e.g., rubidium make this less of a concern in the francium case. To counter this issue, a second laser is tuned to excite atoms from the dark state to an excited state that can decay and put the atoms back onto the cycling transition. This second laser is called the repumper.

A repumper sending atoms back to the cycling transition is the final component neccessary to make a MOT. The combination of red detuning, proper circular polarizations and a quadrupole magnetic field produces a cool, dense collection of atoms for further manipulation and experimentation. All of the neutron-deficient francium isotopes have similarly large hyperfine splittings and behave alike in the MOT. ^{221}Fr, with its much smaller hyperfine splittings, has a smaller number of trapped atoms, but there are still more than enough for physics measurements.

3.3.1 Capture trap

The Francium Trapping Facility has two MOTs. The first, named the capture trap, collects and cools francium atoms from the ion beam in the upper vacuum chamber connected to the beamline. These atoms are available for spectroscopy, e.g. the isotope shift measurements of chapter 4, or can then be transferred down to the second MOT in the science chamber, a cleaner environment for the highly sensitive APV measurements. The capture trap is based on a proven design developed at Stony Brook [71] for their past francium programme, which has evolved into the TRIUMF-based laboratory. The laser light is delivered to the apparatus via single

mode, polarization-maintaining fiber optic cables. All of the optics to condition the beams for the capture MOT, i.e. to set circular polarizations and beam diameters, are attached to a metal exoskeleton structure cage surrounding the cube. This structure is engineered in the appropriate alignment, so that the MOT is set up correctly once the optics are in place, and is depicted in figure 3.7. The glass trapping cell is centered inside the cage with all of its optically flat surfaces accessible. The center of the MOT is determined by the magnetic field minimum of the quadrupole field, generated by a pair of water-cooled, kapton-insulated copper coils in an anti-Helmholtz configuration.

As mentioned in section 3.2.1, the yttrium neutralizer operates on a pulsed cycle. Roughly 95% of the time, francium is collected in the foil. In the remaining time, the foil rotates upwards, closing the trapping cell. It then heats and releases francium atoms into the trapping volume. The glass trapping cell has been treated with a silane-based dry-film coating to prevent the francium atoms from sticking to the walls [72], increasing the number of rethermalizing atom-wall interactions, which occur at each bounce. Rethermalization redistributes the kinetic energies of the atoms. Thus, at each bounce, the low-energy tail of the velocity distribution is repopulated, putting more atoms into the potentially-trapped population below the capture velocity of the MOT, where the radiation pressure is sufficient to confine the atoms before they leave the MOT beam. The capture velocity v_c is determined by the laser wavelength λ and beam diameter D, linewidth of the cycling transition γ and Planck's constant h: $v_c = \sqrt{h\gamma D/m\lambda}$, from the work done by the laser to bring a v_c atom to a stop before it exits the beam [73]. Our MOT has a capture velocity of roughly 5 m/s, compared to a room temperature atom cloud whose average kinetic energy corresponds to a

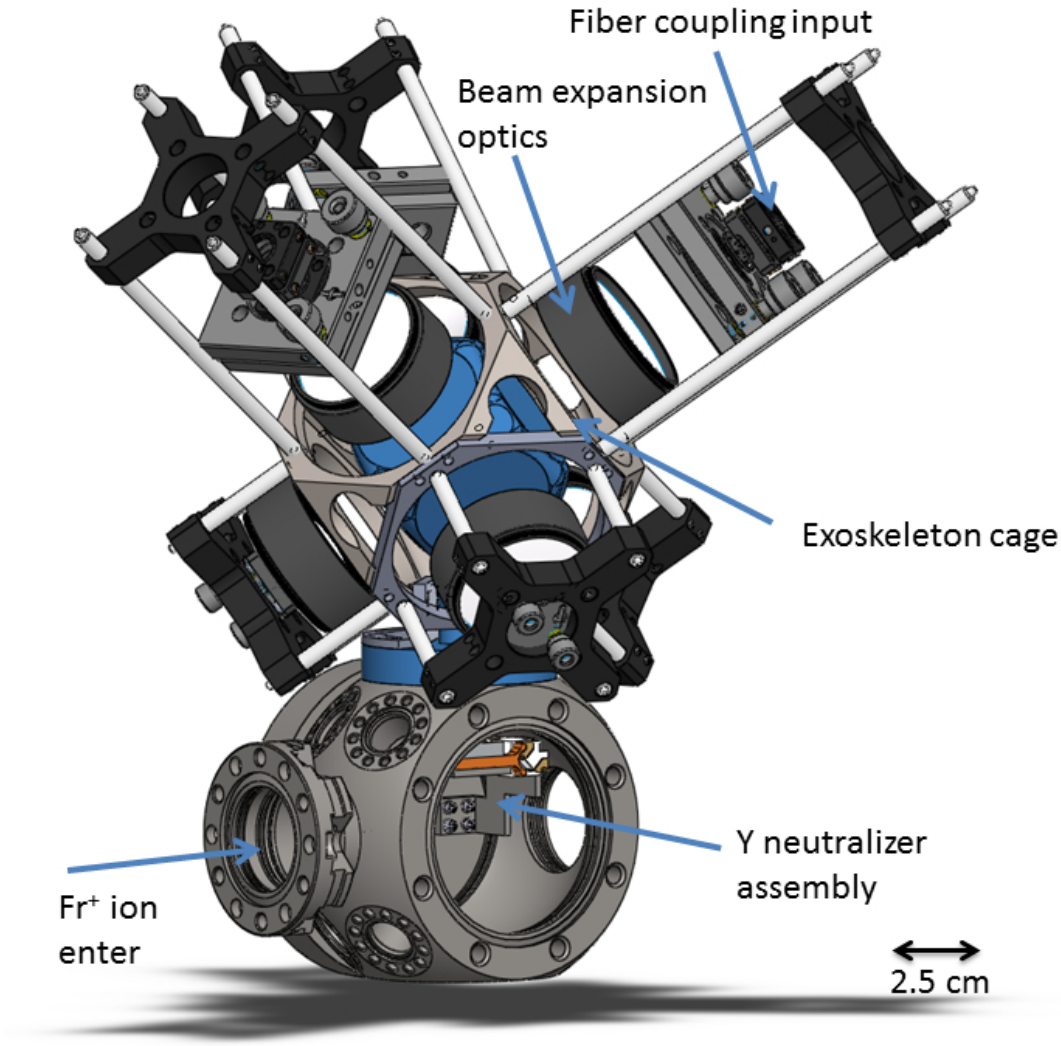

Figure 3.7: Solidworks model of the capture trap and upper vacuum chamber, created by J. Zhang and taken from ref. [70]. All of the laser beam alignment for the MOT are set by the engineering of the exoskeleton cage. The glass trapping cell is in blue and the neutralizer blocks the inlet when it rotates upwards to release francium into the trapping volume.

speed of roughly 100 m/s. The temperature of the atoms released from the heated neutralizer is higher than that and thus only a very small fraction is trapped during a passage through the MOT volume. Increasing the number of passages by encouraging

the francium atoms to bounce from the wall rather than stick to it greatly increases our trapping efficiency. It is difficult to estimate our trapping efficiency as we can not reliably quantify other sources of loss, such as the release fraction from the neutralizer. Our best estimate from our first beamtime is a total efficiency of 0.05% for ions from the ^{209}Fr beam being trapped as atoms in our MOT [70]. A larger release fraction from the neutralizer by better heating, along with other improvements to the trap since that measurement, have likely increased the trapping efficiency of the facility, but we have not directly measured the population since the first commissioning run.

There are two main advantages of this pulsed operation over a comparable continuous trap loading scheme. First, if the dry film coating is good enough to allow a large number of bounces, closing the trap volume with the neutralizer foil when loading prevents atoms from escaping before many bounces off the walls. The cell is open to the vacuum pumps the rest of the time, ensuring a low background gas pressure for a long trap lifetime. Second, the short heating time of the foil minimizes the exposure of the dry film to possible damage; silane-based coatings exhibit degradation after prolonged exposure to high temperatures [72].

The diameter of the laser beams in the MOT is large enough to almost completely fill the glass trapping cell with light, for increased trapping efficiency. They are expanded from the fiber output to fill standard Thorlabs 2" optics, corresponding to a $1/e^2$ Gaussian beam diameter of 5 cm. The magnetic field coils are typically operated at 40 A, generating a field gradient of approximately 7 G/cm (strong axis) for the capture trap. There are also six shimming coils which can be used to cancel out stray magnetic fields impinging upon the apparatus. Offline measurements conducted

in rubidium show a typical MOT size characterized by full-width half-maximum of roughly 0.5 mm and a temperature upper limit of 133 μK.

3.3.2 Science chamber

The science chamber is a separate vacuum chamber that sits below the capture trap [74]. It is separated from the rest of the vacuum apparatus by a pneumatic valve and vacuum bellows, allowing for as much isolation as possible from vibrations and background gases. Additionally, the science chamber sits on a platform connected to an optics table, decoupling it vibrationally from the room. This science chamber will be home to both APV experiments: the $7S - 8S$ optical spectroscopy field plate apparatus, with details provided in section 3.5, and the anapole moment microwave apparatus [54].

The science chamber has its own MOT operating in tandem with the the capture trap to provide a dense sample of atoms for high precision measurements in a clean environment. This MOT has a smaller capture volume, only capturing from the falling atom cloud. It is optimized for beam diameters of 2.5 cm, compared to the 5 cm of the capture trap, and the magnetic field gradient is $\sim$ 10 G/cm, stronger than that of the capture trap. The same trapping and repumping lasers are used for both traps and the push beam; frequencies may be manipulated differently for each MOT by changing the frequency modulation on a series of acousto-optic modulators through which the light passes prior to being coupled into the optical fibers. This also lets the light be turned on/off independently for each trap, and the power in each trap, set by how much light each AOM sends to their respective fibers, can also

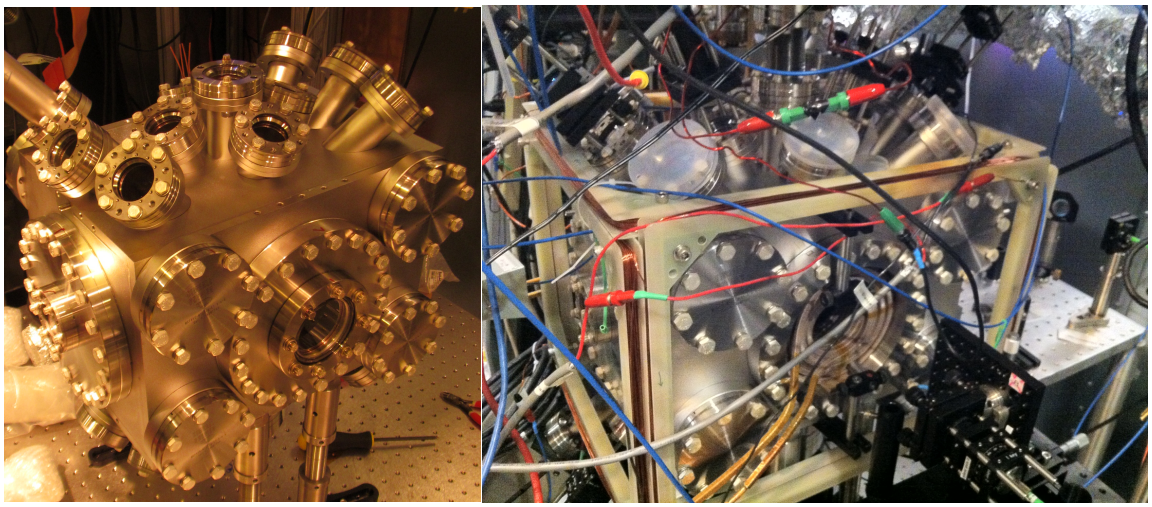

Figure 3.8: (Left) Photograph of the science chamber in its position below the capture trap, before optics and a transfer section linking to capture trap have been installed. (Right) Photograph of the science chamber with optics and the transfer section linking to the capture trap. Visible on the front is a recessed viewport, allowing the magnetic coils to remain outside of the vacuum. This image is of the setup after successfully demonstrating the transfer of francium atoms between the MOTs.

be manipulated as required during the transfer cycle. This setup ensures that there are no concerns about the transfer failing due to frequency issues with the science chamber trap; if there are atoms available to be transferred, the science chamber trap will be able to catch them. Atoms in the capture trap are illuminated with a vertical push beam to transfer them into the science chamber MOT where they are caught and retrapped. The push beam is 4 mW and is set to be parallel with a diameter of 5 mm. It is aligned with both capture and science MOTs as determined by observation of the trap being 'blown away' when the push beam is turned on.

The efficiency of the transfer in rubidium is estimated from the intensity of the digital images of the traps. Each trap is viewed by identical PointGrey Flea3 digital cameras with the same quantum efficiency 35% at 780 nm, set for the same exposure times. We measure the power in the MOT beams and set them such that the atoms

experience the same intensity of light in both traps. Then a direct comparison between the counts on the analog-digital converters (ADC) of each camera in the region of the atom clouds gives a good estimate of the ratio of the number of atoms in each trap. Optimization of the transfer produced best efficiencies of ∼70% for rubidium. Transfer of francium has been demonstrated in the 50-60% range at our most recent beam time.

There are many parameters for the trap-to-trap transfer that have been explored using rubidium. The most sensitive is the push beam frequency, set to be approximately 21 MHz below the trapping transition. Small shifts of 6-9 MHz (∼1-1.5 atomic linewidths) reduce the transfer efficiency by at least a factor of 2. We saw no noticeable effect by attempting to catch faster atoms by ramping the detuning of the science chamber trap during the push time. The transfer efficiency appears to be fairly insensitive to the field gradient of the science chamber trap and the precise alignment of the push beam, within reason. We also employed an optical funnel through windows midway down the transfer pipe between chambers; the funnel did not affect the transfer efficiency.

The commissioning of the science chamber occured in December 2014, where we demonstrated the transfer of francium from the capture MOT to the second trap in the lower chamber. Initial attempts at this transfer were successful with an estimated efficiency of 10%. Unfortunately, the neutralizer foil then developed a crack which prevented further trapping and we were unable to optimize the transfer rate.

3.3.3 Lasers

There are a number of lasers used for our experiments in the Francium Trapping Facility. We primarily utilize Ti:sapphire ring lasers for their broad tunability, allowing a relatively easy wavelength change for the switch between online francium and offline rubidium. Additionally, there is a pair of diode lasers. The first is a Toptica DL100 at 780 nm, now permanently assigned to a saturation spectroscopy setup used to calibrate a precision wavemeter, and the second is a Sacher diode laser at 817 nm as a backup repumper in case another laser fails during or leading up to a beamtime.

There are two types of Ti:sapphire lasers in the FTF. They are all capable of outputting several Watts of power over their tunable ranges, typically 700-950 nm. We have a pair of the first type, the Coherent 899 class of lasers, one with an additional external reference cavity for increased stability. This 899-21, with the cavity, is often used as the repumper laser for the trap while the more basic 899-01, without an external reference cavity, is a backup. The other type of Ti:sapphire lasers in the FTF are the new M2 SolsTiS. These lasers are built to have very good passive frequency stability and power output, improved by internal electronics providing feedback along with their attached external reference cavities. One has an additional frequency doubler to produce the 506 nm (496 nm) light for the forbidden transition in francium (rubidium). The fundamental output of this laser is tunable from $\sim$810-1020 nm and can also be used as a repumper or probe at the francium D2 wavelength of 817 nm. The other SolsTiS is our primary trapping laser for both francium and rubidium. These SolsTiS lasers are controlled via computer interface, where they can be tuned using graphical sliders and buttons.

Trapping can only occur efficiently on the D2 transition at 718 nm. We also repump on the D2 transition to keep the D1 transition clean for measurement at 817 nm. Both trap and repump laser light are coupled into a fiber splitter to generate the three spatial beams at two frequencies that are retro-reflected to trap on each axis. Laser powers delivered to the trap are limited by the coupling fibers, resulting in approximately 20 mW/cm^2 in the trapping beams and 5 mW/cm^2 in the repumping beams; all beams of the capture MOT have $1/e^2$ power diameters of 5 cm to cover all space inside of the MOT cube, and the beams for the science MOT are 2.5 cm in diameter. Quadrupole magnetic field coils provide a field gradient of approximately 7 G/cm (strong axis). The typical detuning of the trap laser is about 15 MHz, roughly two and a half linewidths detuned to the red. Once the transitions are found and the isotope is trapped, the lasers are locked using a polarization stabilized HeNe laser as a reference, transferred via the scanning Fabry-Perot cavity (more details are provided in section 3.3.4). The stability of the laser-lock system is important and will be discussed below.

3.3.4 Frequency stabilization

Our narrow linewidth lasers are constructed with active and passive components designed for short term stability to reduce linewidths. They do not have the internal ability to correct for long term frequency drifts caused by, e.g., external environmental factors. These drifts, over minutes or hours, are unacceptable during a long measurement, where they introduce systematic errors and/or cause the MOT to gradually or suddenly fail. Slow drifts are corrected via a feedback signal generated from the dif-

ference from an external reference, typically via saturation spectroscopy of an alkali or I_2 gas.

For radioactive francium, we do not have easy-to-use atomic references at the frequencies required for trapping. Thus we have built a transfer lock system for the long term stability of our trapping lasers. This provides an insensitivity to such problems as temperature drifts, allowing the lasers to stay at their set frequencies. Hence we can trap for an indefinite period without having to manually adjust those lasers.

The transfer lock we have implemented is based on previous work [75] and works by transferring the stability of a 632.8 nm polarization-stabilized HeNe laser (Melles-Griot 05-STP-901) to any other laser using a confocal scanning Fabry-Perot cavity. The cavity has a free spectral range of 300 MHz and a finesse of 100 at 718 nm. Signals from photodiodes are sent to the analog inputs of National Instruments ADC cards, whose analog outputs provide corrective feedback to the lasers.

The LabView-based control program operates by sending a voltage ramp to a high voltage amplifier (Exfo RG-91), which is then sent to a piezoelectric crystal on the Fabry-Perot cavity, scanning its length. Light from the stabilized HeNe and other lasers will be transmitted through the cavity only at specific voltages on the piezo. Light exiting the cavity is split using dichroic filters or polarizing beamsplitters onto specific photodiodes, each corresponding to a single laser to be stabilized. The photodiode signals are acquired in synchronization with the voltage ramp, and the control program then locks the relative frequencies of each laser with respect to the HeNe by keeping the relative positions of the transmitted peaks constant.

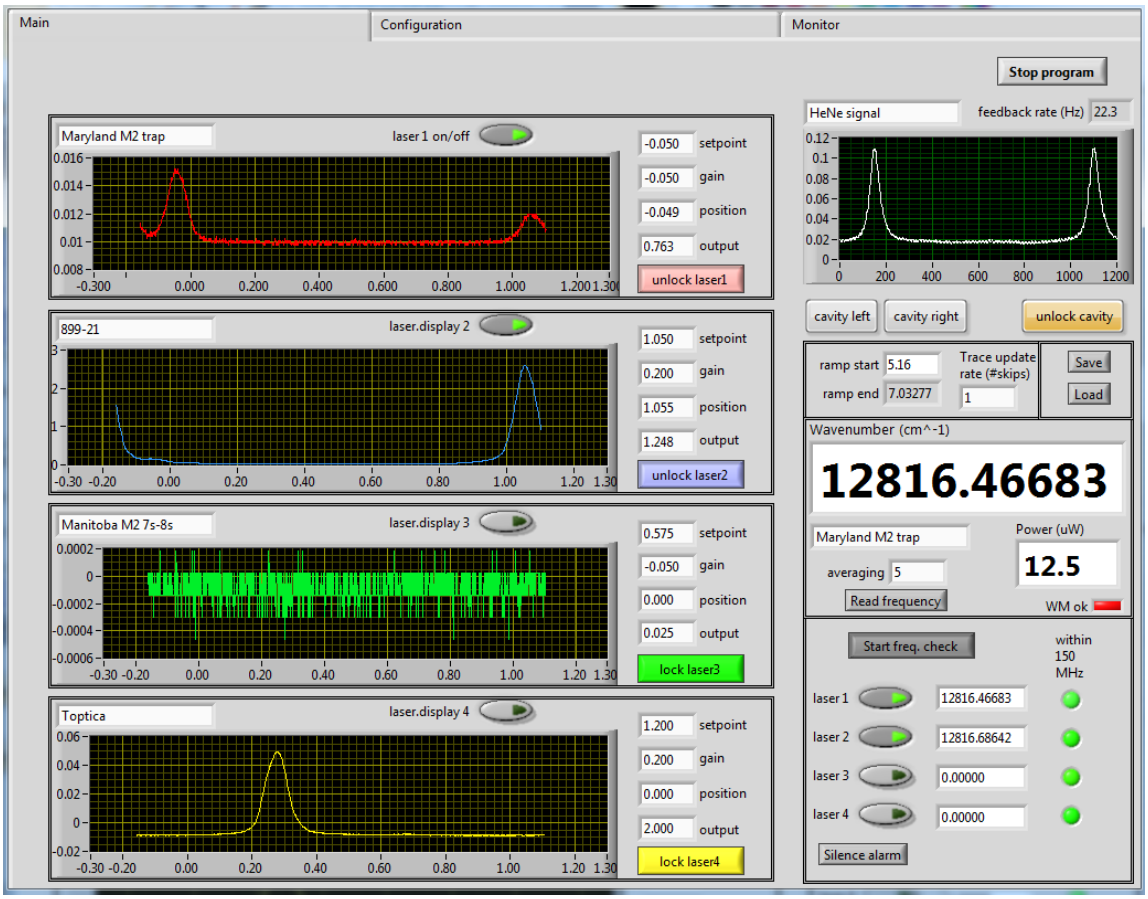

Figure 3.9: Screen capture of the front panel of the cavity locking program. The top right shows the two HeNe peaks from adjacent cavity modes. The other laser traces lock their peak positions relative to those HeNe peaks, transfering the long-term stability of the polarization stabilized HeNe to any other laser. Communication with the High Finesse wavemeter enables continuous monitoring of laser frequency accurate to a few MHz.

Initially, the stability of the laser lock was on the order of roughly ±5 MHz over a few days. The main drift arose from changes in atmospheric conditions having an effect on the optical length of the cavity. This has been ameliorated by placing the cavity under vacuum and maintaining it at a set temperature via proportional-integral-derivative control. This improved the system to its current stability of ±2 MHz. At this level, we are at the limit of the components used with non-linearities

in the piezo crystals and the stability of the HeNe being the dominant contributors. Additional details of the laser locking program are available in appendix D.

3.4 Francium production from ^{225}Ac decay

We have developed a long-lived radioactive source for ^{221}Fr fed by the decay of ^{225}Ac. This source complements the radioactive beams provided by TRIUMF, which are limited by target availability and sharing with other experiments. A complete description of the system is available [76]; we will only describe it briefly here.

^{225}Ac ($t_{1/2} = 9.920(3)$ days) continues to diffuse out from the UCx target once the proton beam is removed if the target remains at its operating temperature. At ISAC, this is achieved by the use of resistive heating. It can continue to be delivered like any other requested beam. The 20 keV beam is implanted in a primary tantalum foil, turned to face the incoming beam. This implantation occurs for several hours and the resulting source's activity is determined by the total amount of ^{225}Ac implanted and its decay half-life of 9.920(3) days. The relatively long half-life of ^{225}Ac gives the source a viable operating life longer than a month, by which time the rate has decreased enough that, combined with other efficiencies before trapped atoms are observed, the number of trapped atoms in the capture MOT is no longer useful.

Once the incoming proton beam is removed, the tantalum foil is rotated to face the yttrium neutralizer 3 mm away This corresponds to the secondary foil in the down position in figure 3.11. Following ^{225}Ac decay, the recoil energy of ~ 105 keV is more than sufficient to eject the daughter ^{221}Fr from the foil. If the randomly directed recoil leads outwards, the ejected ^{221}Fr is implanted in the yttrium foil, which is rotated

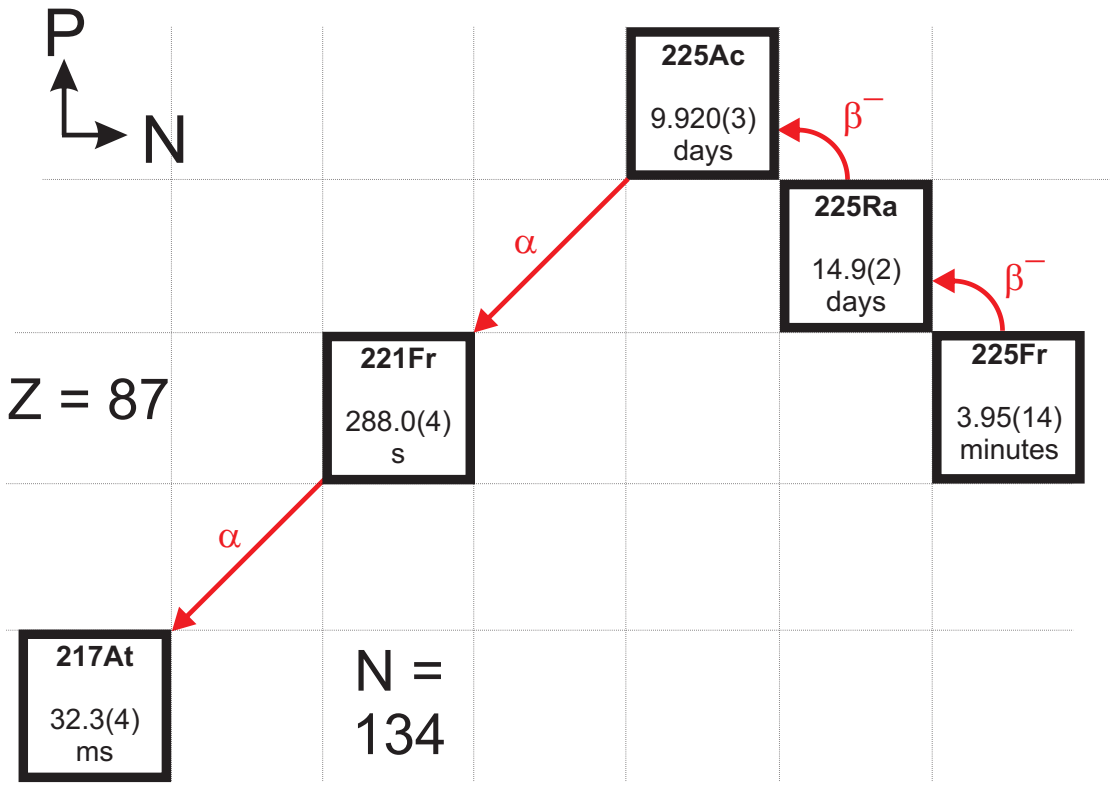

Figure 3.10: Simplified decay chain for the ^{221}Fr implantation scheme [76]. Decays inside the target produce the relatively long-lived ^{225}Ac that is delivered to us by ISAC. The ^{225}Ac in our apparatus decays to ^{221}Fr, which we trap and use for further studies.

and heated the same as in an online experiment.

Our estimate of the efficiency of this offline source determines a 10-100 times lower yield compared to an online source of francium. It is difficult to produce an exact value as the diagnostic is the number of atoms in the MOT, which is succeptible to variable losses in trapping efficiency day-to-day, such as precise laser frequencies or background vacuum pressure. Additionally, ^{221}Fr is more difficult to trap due to its smaller hyperfine splittings compared to the neutron-deficient francium isotopes,

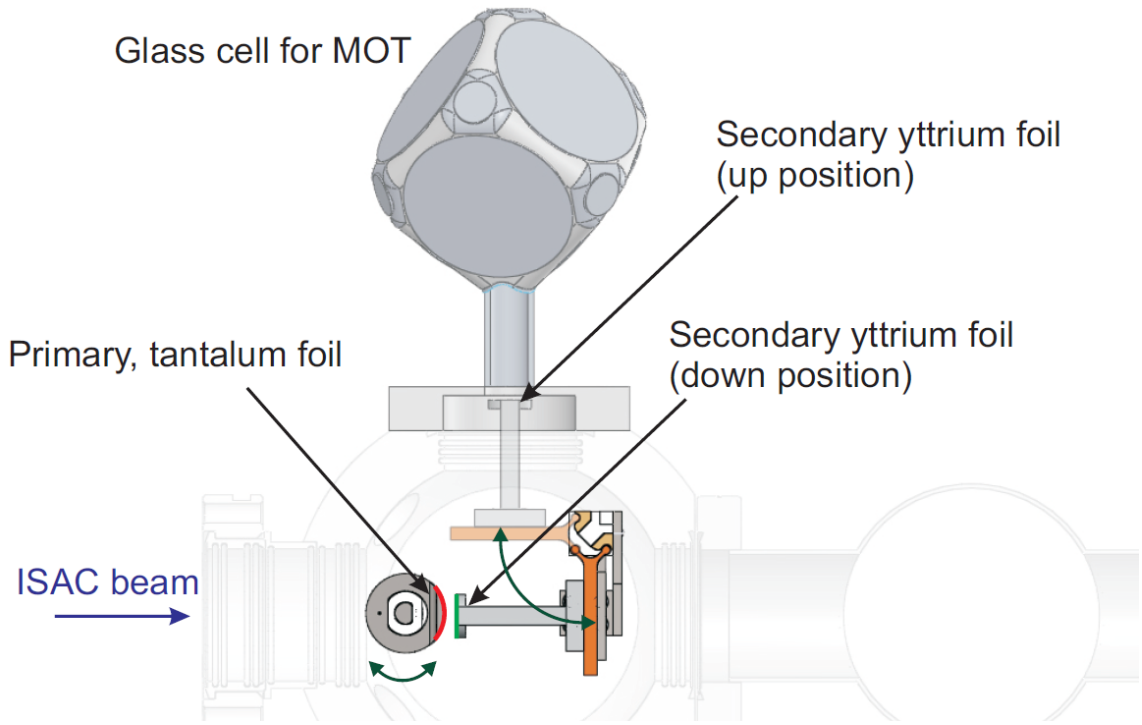

Figure 3.11: Diagram of the actinium implantation apparatus [76]. Ion beam from ISAC is implanted for several hours in the primary tantalum foil. Once the beam is removed, the foil is rotated to face the secondary yttrium foil. Recoiling ^{221}Fr daughters of the ^{225}Ac α decay accumulate in the yttrium, and neutral francium release proceeds as in the online scenario.

further complicating the matter. The offline source produces a more diffuse implantation spot on the yttrium foil compared to a well collimated ion beam, due to the ^{225}Ac decaying from a point-like source 3 mm away. ^{221}Fr is implanted deeper in the yttrium from the offline source; the α-decay implants them with energies up to 105 keV into the yttrium while the francium ion beam energy is 20 keV. The angle of emission from the yttrium foil due to the random angular distribution of the decays also contributes a geometric factor to the efficiency. Nevertheless, we have demonstrated that the offline source is viable for francium trapping, providing us with an option when francium beams are unavailable.

There are some disadvantages to this technique. The hyperfine splittings of ^{221}Fr are much smaller than those of the neutron deficient francium isotopes. This presents a different challenge in trapping ^{221}Fr, as nearby hyperfine states allow more population to escape the cycling transition and end up in the dark hyperfine ground state, requiring more repump power. The ground state hyperfine splitting also limits its usefulness for the anapole moment experiment [54]; the microwave equipment designed for the 40-50 GHz splitting of the neutron deficient francium isotopes does not function at the 18.6 GHz required for the ^{221}Fr ground state splitting. Thus the offline source is useful as a complement, not a replacement, to the online ion beams provided by ISAC.

3.5 Electric field plates

The field plates that will generate the electric field for the Stark-induced $7S - 8S$ transition measurement have a number of design considerations. First, they must accomodate the MOT in the science chamber. This means that the plate spacing can be no less than 1", as that is the size of the laser beams of that MOT. Furthermore, the geometry that best suits our measurement places the z-axis MOT beam passing through the field plate. Uniformity of the field is another important consideration. The cesium experiment lists typical stray fields being on the order of 50 mV/cm [3]; our design should keep this uniformity in the region we expect the atom cloud to occupy. This also means that the plates should be as large as possible, to reduce the effects of fringing from the edges of the plates. The limitation on plate size is that the entire apparatus must fit through the bore of the 8" conflat flange on the side

of the science chamber. Considerations for the mechanical support of the field plates include *in situ* mounting and optical access for probe beams and imaging.

One last point to consider is the distance between charged surfaces and any grounded surface inside the vacuum chamber. Our rule-of-thumb is to have this distance no less than 1 cm, to prevent arcing discharges when 10 kV with respect to ground is applied to the field plates. While this voltage is well above that required for a final parity violation measurement, it may be required in the initial stages when searching for a signal.

The electric field modelling in this section was performed using SIMION 8.0 [77]. This commercial software is designed for simulating ion paths through modelled ion optic elements. We employ its modelling capabilities to design electrodes and solve the Laplace equation $\nabla^2 V = 0$ for the desired combination of electrodes. Many of the figures shown in this section are from this software. They will show the equipotentials calculated by SIMION to visually depict the electric field, which is useful for a qualitative understanding of the field uniformity.

3.5.1 Metal plates with holes

Proposed designs can be broadly categorized into two types. The first is metal field plates with holes in them to accomodate the MOT laser beam along the z-axis, perhaps with some modification to improve the field profile in the center between the plates. Complicated designs consisting of many charged rings, held at different voltages to create a uniform field profile in the MOT atom cloud location, were discarded early in the design process. Their difficulty lies in exactly balancing the

applied voltages, as well as rebalancing them for a field reversal, required for the $7S-8S$ interference measurement. Performing this field reversal exactly, reproducibly, and on a short timescale is deemed to be too large a potential source of systematic error for such an arrangement of rings. Thus we aim to keep the design simple with a limited number of elements.

The centered 3 cm diameter hole in the field plate, providing clearance for 2.54 cm (1") MOT beams, is an unavoidable constraint which limits the field uniformity. One way to compensate for this hole is to extend a conducting tube outwards from the plates, electrically connected to each plate and thus held at the same voltage. The plates can be any shape, with preference given to square and circular plates for ease of modelling, so long as they will fit through the 8" CF bore.

First, consider circular disk electrodes, with 1" tubes protruding from the backs. There is an improvement in the field profile over the same disk without the charged tubes, as shown in figure 3.12. However, the tubes need to be very long for a complete correction to the field uniformity, and these tubes would not fit into our chamber with the recessed viewports. They also would need additional clearance to prevent discharging to any other nearby grounded metal and would not be compatible with any other field plate support apparatus. Thus, for a first iteration of the field plates, we will proceed without any additional conducting structure to compensate for the holes.

The design chosen for metal electrodes consists of 4.5" square plates with 1" circular holes centered on each plate, as shown in figure 3.13. All of the edges are rounded to prevent the high fields associated with points and leading to discharges.

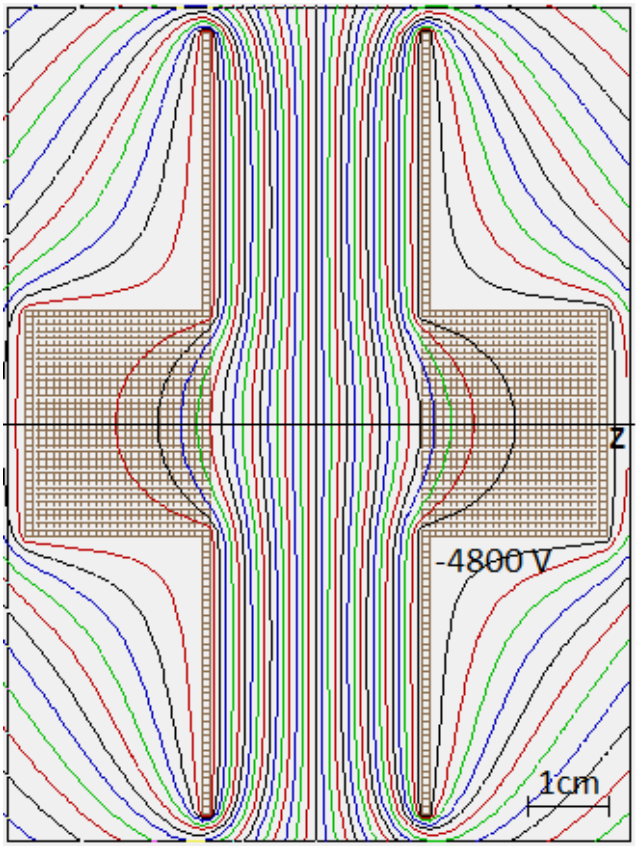

Figure 3.12: SIMION electric field modelling showing the equipotentials between two circular plates charged to ±5000 V with circular holes and protruding tubes. The equipotentials are separated by 300 V and the lowest equipotential shown is at −4800 V. The tubes restore some uniformity to the central region, however the field does decrease away from the exact center.

These plates use the same support structure designed for the transparent field plates, as discussed in section 3.5.2, and it is a simple matter to exchange the two.

The model of this field plate design in figure 3.14 includes the effects of one charged and one grounded electrode, the grounded stainless steel plates on the support structure that the electrodes connect to, and the (not shown) grounded vacuum chamber. Currently, we only have one high voltage power supply capable of +0-20 kV. In this situation, with only one electrode charged, the steel support structure plates have no-

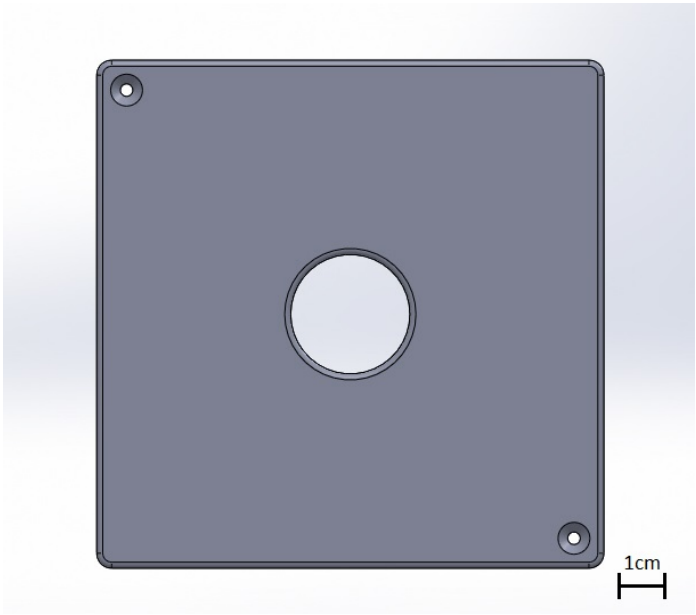

Figure 3.13: Model of the 4.5" square stainless steel metal field plates, viewed from the side facing the atom cloud. The 1" circular hole provides clearance for the MOT beam passing through the plate and all edges are rounded to prevent arcing when the plates hold charge. Screw holes are recessed to prevent protruding heads from the screws connecting the field plates to their support structure.

ticeable effects on the field. The grounded steel plates effectively displace the uniform region between the electrodes towards the uncharged electrode, as shown in figures 3.14 and 3.15, away from the preferred location of the trapped atom cloud. In this case, an exact field reversal is no longer possible by reversing which voltage is applied to the two electrodes, which is the simplest, and hence strongly preferred, method of reversing the electric field. Thus, for any measurement where the uniformity is critical, the electrodes will need to be charged independently to opposite voltages and not have one grounded.

The electrical connection is made through Accuglass Capton insulated wire, secured to the plate by a screw in the back. Isolation between the charged field plate

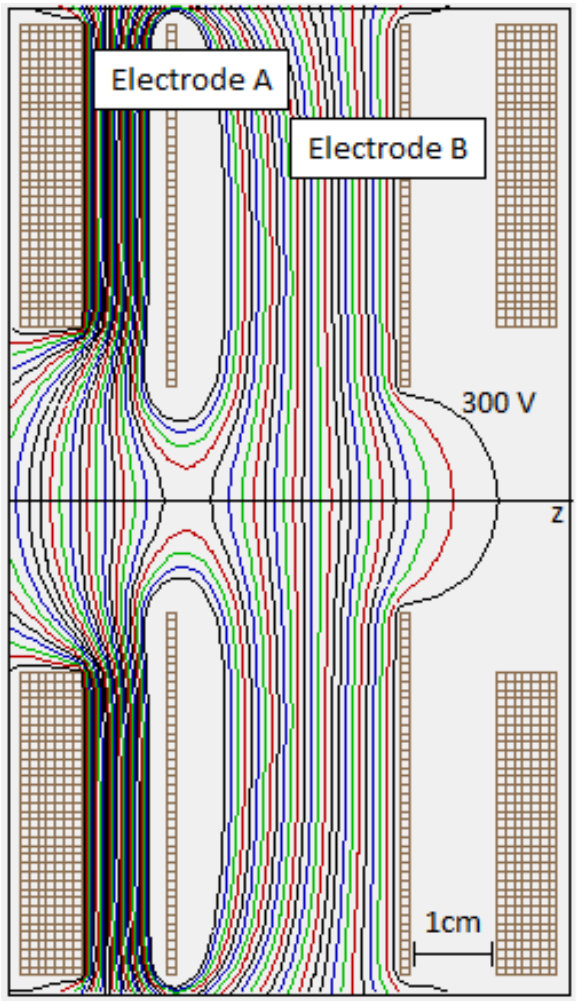

Figure 3.14: SIMION electric field modelling showing the equipotentials between two square field plates with circular holes. Electrode A is charged to 10 kV and electrode B, along with the stainless steel plates behind each electrode, is grounded, producing a field of 2775 V/cm in the center. The region of uniform field is displaced towards the grounded electrode B.

is provided by ceramic standoffs, each 6/32" long. An SHV bulkhead connector connects to the other end of the capton insulated wire and allows the high-voltage into the vacuum. All external connections are made via a single 8" CF flange, for ease of exchanging between the field plates of the optical $7S - 8S$ experiment and the microwave cavity of the anapole experiment. The field plates have been tested and

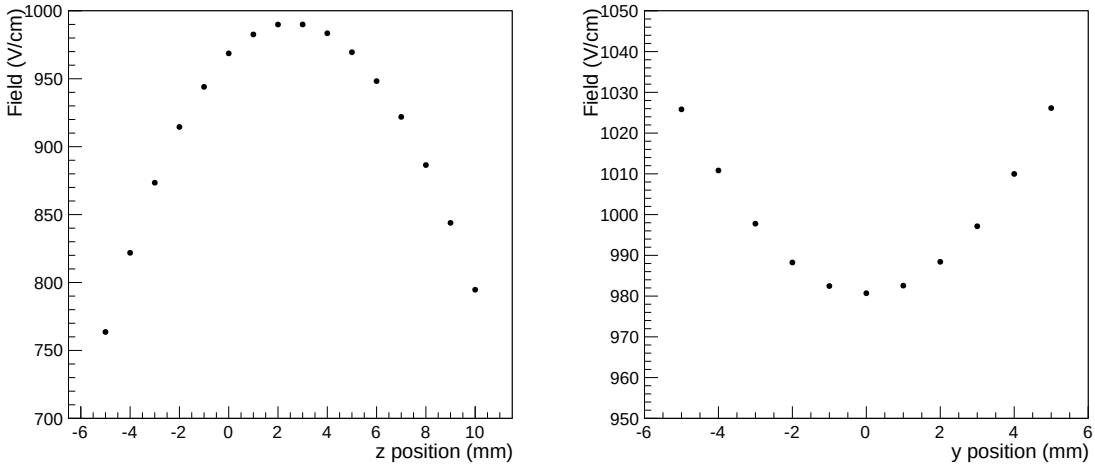

Figure 3.15: (Left) Simulated electric field profile between the field plates, along the axis through the plates (z). Note that the maximum, where the field is more uniform, is displaced from the nominal center of the trap at $z = 0$. Field plate positions are at $z = \pm 13$ mm. (Right) Simulated electric field profile between the field plates, along the vertical axis between the plates (y). The field minimum, where the field is more uniform, is centered at the nominal trap position at $y = 0$.

hold 10 kV without discharging in vacuum. During assembly, it was decided that the plates should be spaced at 1.125", to preclude any possible interference with the critical first-demonstration of transferring francium atoms into the science chamber. This would change the magnitude of the electric field present, but not the shape of the field profile compared to the original plan. Unfortunately, failure of the yttrium neutralizer occured before we could apply high voltage across these field plates in search of a Stark-induced $7S - 8S$ transition in francium.

3.5.2 Transparent field plates

The second type of field plate we have considered is a transparent conducting electrode. This consists of a transparently thin layer of conductor applied to a glass

substrate. We have selected indium tin oxide (ITO) as our transparent coating. There are other transparent conducting electrodes available; however they are usually more expensive and exhibit poorer performance [78].

The electrode consists of a 4" circle of deposited ITO on a square BK7 glass plate. Holes are drilled at the corners of the glass plate for mounting the plate to the support structure. The holes are placed such that they do not align with the radial MOT beams, which enter at 45° to the horizontal. Our simulations show that electrodes of these dimensions show electric field non-uniformities on the order of 10 mV/cm in the region where we expect our atoms to be, well below our constraint set by the cesium experiment. Additionally, the outside surfaces are antireflection coated for less than 1% reflectivity for 718-817 nm from that surface. Total transmission for the ITO field plates is between 92-95% for the range of laser wavelengths used in our MOTs.

The issue of patch fields remains unknown for these ITO electrodes. Patch fields are generated by a combination of three factors: crystal orientation, composition inhomogeneities and surface adsorption. These three factors cause a change in the work function across the surface of the material, resulting in small regions of slightly different electric field. Patch fields, and their gradients, can mimic a parity violating signal by not reversing correctly with a voltage reversal and so great care must be taken for their control during a high precision APV measurement. The cesium experiment eventually abandoned the use of transparent electrodes due to patch fields [79]: a recurring problem even with their metallic field plates. It was believed that one of the leading causes of patch fields was the deposition of cesium from their massive

thermal atom beam, as they saw patch fields get worse over time for some materials. This is not a problem for the francium trap as we do not receive radioactive beams remotely near such quantities. Furthermore, our plate separation is 2.5 times larger than the 1 cm of the cesium experiment. As the patch field effect falls off as $1/z^2$ [80], it should be a smaller problem for us. Ultimately, the cesium experiment constructed field plates of a thin layer of molybdenum for its very low patch field contribution [3], which is unfortunately not transparent and can not be used in our geometry.

The support structure for the electric field plates was designed for these transparent electrodes, as shown in figure 3.16. Due to the cost of these ITO-coated plates, it is much more economical (and much, much quicker) at this early development stage to construct additional metal plates and adapt them to the structure than to order additional transparent electrodes. The electrodes are attached to a steel support plate, which is in turn connected to a steel tilt platform. This tilt platform is clamped onto a support plank that spans the science chamber and is secured to the flange on each end. The tilt platform can tilt and rotate with respect to the support plank, hence allowing for adjustment of the electrodes with respect to the rest of the science chamber. The connection between the support plate and tilt platform can be adjusted in position and secured to set the electrode spacing. All of these steel pieces are made of 316LN stainless steel for its high resistivity and low magnetic susceptibility compared to other steels. This will reduce inconsistent magnetization of components and eddy currents, which will help reduce stray magnetic fields and MOT magnetic field turn-off times, respectively.

The support structure leaves optical access open from the bottom for imaging

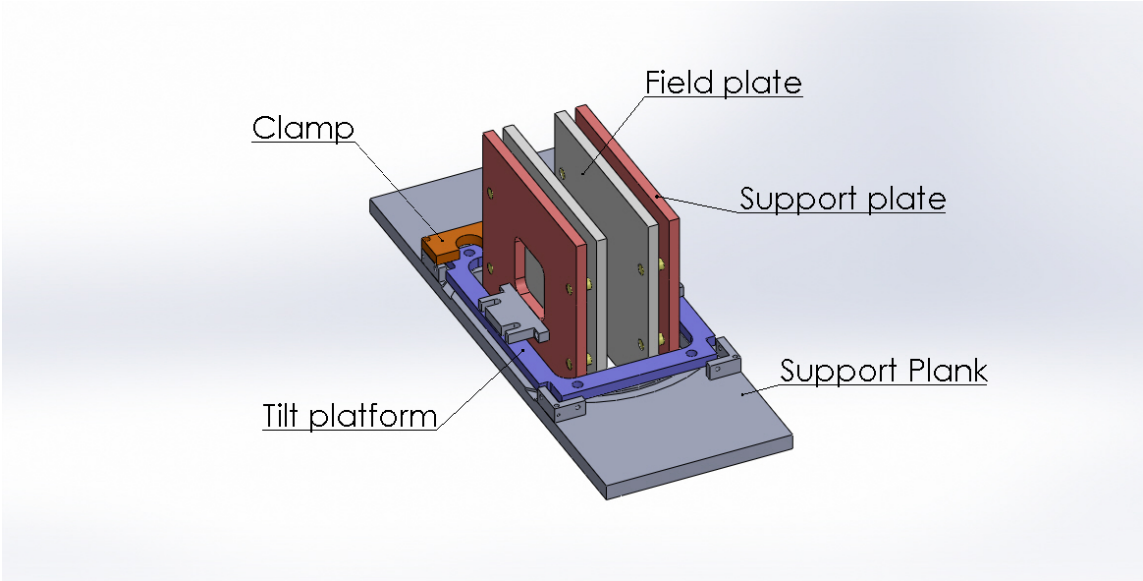

Figure 3.16: Model of the field plate support structure. The field plates are connected to a support plate, which is in turn adjustably connected to the tilt platform. The tilt platform can be tilted and rotated with respect to the support plank, to which it is clamped once aligned. The second clamp mirrors the position of the labelled clamp and is not shown.

and optical pumping. The horizontal access is left open for the forbidden transition laser and future power buildup cavity. More than enough space has been left on the supporting plank to accomodate the power buildup cavity in vacuum. This plank has been separated into two pieces; one of each is mounted on the 8" CF flanges on the sides of the science chamber for installation purposes. Each piece of the plank can be secured to the flange outside of the chamber. Both flanges are then installed, leading the pieces together inside where the three titanium guide pins on one piece make a precise fit on holes on the other piece, allowing a robust, reproducible mating and thus consistent positioning of the electrodes. The guide pins are titanium to prevent cold welding to the sides of their holes during a vacuum bakeout.

There was an error made during the design of the support apparatus leading the

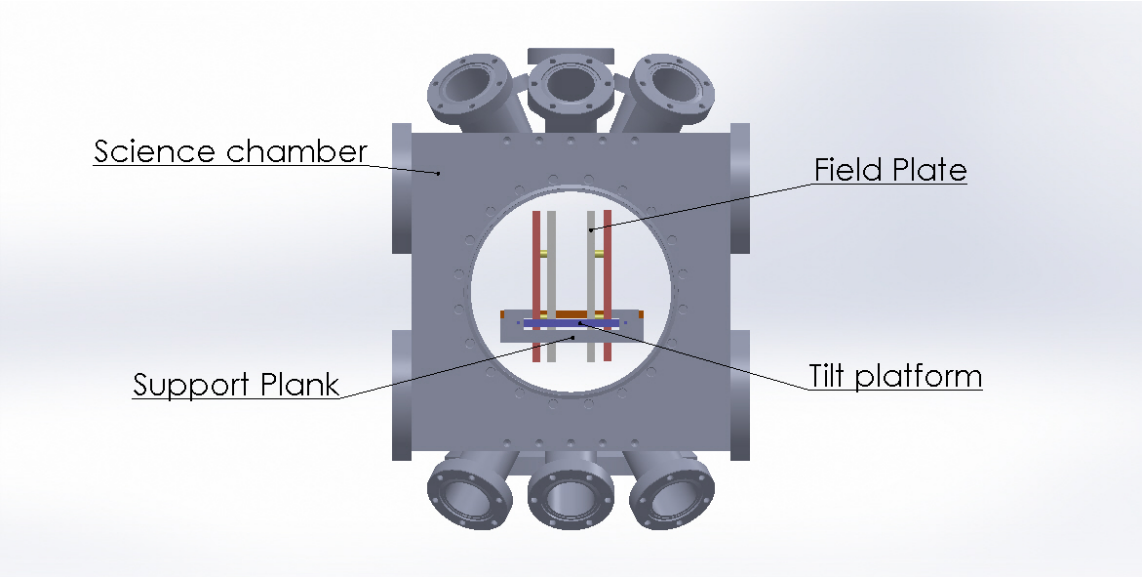

Figure 3.17: Model of the field plates and support structure placed inside the science chamber. The entire structure must fit through the 8" CF bore. Flanges on both ends of the science chamber connect to the support plank, holding it in place, and contain all of the electrical connections and other future vacuum feedthroughs for the optical spectroscopy experiment. The mounting connections make the installation straightforward and ensure a reproducible positioning of the field plates.

steel plank spanning the science chamber to be too short by 2". Two adapter pieces were constructed to correct this mistake. These adapters will not be needed in any future iterations of the support structure if the plank is made long enough.

One outstanding issue is the method of setting the precise spacing of the electrodes. The current implementation has 1" precision-ground Macor spacers setting this distance between the front faces of the glass substrates. Macor, a machinable glass-ceramic, is an insulator, preventing shorting or discharging between the electrodes along the spacer. This also means that it will not dissipate any accumulated charge, possibly leading to irreproducible stray fields in the science chamber. One proposed solution is to coat the outside of the macor spacer with a thin film resis-

tor, converting the spacer into a high-value resistor that will gradually dissipate any accumulated charge. Unfortunately, we have not found a company willing to do this for us, so this modification has not yet been implemented.

Chapter 4

Isotope Shifts

4.1 Introduction

Isotope shifts of atomic transition energies, through the nuclear field shift contribution (as discussed in section 2.3), are a useful probe of the overlap of the electronic and nuclear wavefunction. Measurements of isotope shifts provide a stringent test of theory, required for correct interpretation of atomic parity violation measurements.

Absolute measurements of the field shift are difficult for several reasons. First, the electron correlation calculations required for the subtraction of the specific mass shift are extremely challenging in all but the lightest elements. Fortunately, in heavy elements the specific mass shift comprises only a small fraction of the total isotope shift. In francium, this is less than 0.5% of the total isotope shift; the ^{221}Fr$-^{212}$Fr D1 isotope shift is 22437(4) MHz with a calculated mass shift of 39 MHz [6]. Second, field shifts, dependent on the nuclear charge radii and the electronic distributions of the atoms, require knowledge of both. Charge radii can be obtained by scattering

experiments for stable species, which is not possible for francium. We circumvent these difficulties by means of a King plot [65].

The King plot takes the isotope shifts of any two transitions, electronic [81, 82, 83] or muonic [84, 85], scaled by the mass factor of the normal mass shift, and thereby separates the mass shift from the field shift. The linear relationship on the King plot enables a precision measurement of ratios of the isotope shift constants of both transitions. For francium, there exist D2 line data [86], but not much else for many isotopes. In this chapter, we present the measurement of the D1 isotope shifts for the other axis of the King plot, obtain the isotope shift constant ratios and compare them with theory predictions. Our results benchmark those calculations, enabling further refinement of methods that will be used for future parity violation measurement interpretation.

Much of this chapter has previously been published [6]. However, many additional details are presented here that were not appropriate for the concise nature of a journal publication, e.g., the analysis of higher-order nuclear corrections. Additionally, since the publication, new measurements of D2 isotope shifts, relevant to our King plot, have appeared in the literature. These measurements resolve an outstanding issue with the ^{206}Fr point on the King plot and allow us to include the isomer ^{206m}Fr. The updated version of the King plot is here with an erratum for the journal publication being prepared at the time of this writing.

4.2 Experimental Technique

An isotope shift is a differential measurement; a reference is required. The isotope shift measurements we have performed involve the fast radiofrequency (RF) scan of sidebands on a carrier (probe) laser in a fiber modulator to locate specific transitions in a particular isotope with respect to a reference isotope. This RF scanning technique has several advantages over scanning the laser frequency. First, measuring absolute laser frequencies is difficult without a very well known, nearby reference transition, which we do not have in francium. For the RF sideband technique, we only need to know the sideband frequency for the relative measurement from one isotope to another and not the exact laser frequency. Measuring the RF is possible to very high precision using inexpensive commercial equipment, in our case passive mixing components and an oscilloscope. Second, the RF scan is robust and very linear. Non-linearities in, e.g., piezoelectric crystals would cause a systematic effect in a laser scan, and scanning itself can induce mode hops. Both of these issues are avoided by using the RF scanning technique.

Figure 4.1 depicts the measurement scheme. First, we collect one isotope in the MOT, such as ^{206}Fr in figure 4.1. Then we tune the probe laser frequency to lie in the hyperfine multiplet of the D_1 line originating from the upper hyperfine ground state, and sweep the sideband frequency in 10 ms to find the transition. The 10 ms sweep is fast enough that we can neglect varying experimental conditions, such as the lifetime of the trap or radioactive lifetime of the francium isotopes. Sweeping is repeated until enough counts are accumulated that the transition peak is judged able to be fit. This could take seconds to minutes depending on the number of atoms in

the trap, which is isotope dependent. Next, we change the isotope in the trap, to e.g. ^{209}Fr, and sweep the RF sidebands again to find the desired transition while the carrier remains locked. The measured difference in RF frequencies is used to calculate the isotope shift.

Data collection occured during two experimental periods using two different RF generation schemes (details below). In the first period we measured the isotope shifts of ^{206,207,213}Fr with respect to ^{209}Fr, while the second yielded $^{206,208-212,221}$Fr with a fixed carrier laser wavelength and no need to return to a reference for each new isotope. This was allowed by new RF generating equipment and will be discussed later.

Our RF sideband method finds the transitions to both excited hyperfine levels by selecting the probe laser frequency such that the positive and negative sidebands each excite a transition, see figure 4.2. By taking the difference in the two peak frequencies, we obtain the hyperfine splittings to 100 ppm precision, sufficient to study changes in the hyperfine anomaly [87]. The hyperfine splittings and nuclear spin are required to calculate the hyperfine shifts of the ground and excited states, which are different for each isotope. These are necessary to extract the isotope shift since we need to locate the center of gravity of the transition. We determine the isotope shift from:

$$\delta\nu_{IS} = (\nu_1 - \nu_2) + (\nu_{HFg} - \nu_{HFe}) - (\nu_{HFg} - \nu_{HFe})_{ref}, \tag{4.1}$$

where $\nu_{1,2}$ are the RF frequencies where the hyperfine transitions are observed (see figure 4.1), $\nu_{HFg(e)}$ are the hyperfine shifts of the ground (excited) states for the measured isotope and the reference. The common probe laser frequency is not included

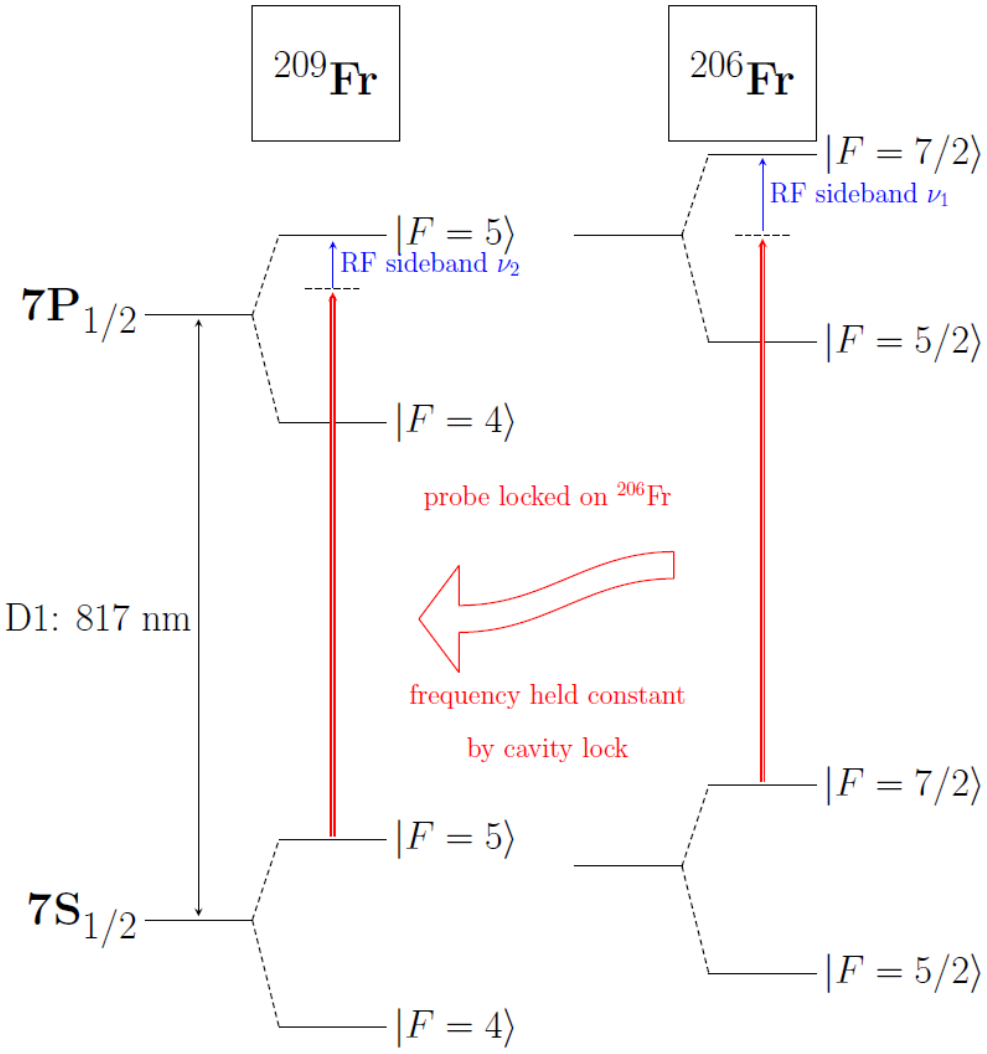

Figure 4.1: Isotope shift measurement scheme, splittings not to scale. The transition to the upper hyperfine excited state $F = 7/2$ is located in ^{206}Fr, and the probe laser frequency is locked using the external Fabry-Perot cavity. Then ^{209}Fr is trapped, and the transition to $F = 5$ is located by changing the RF frequency only, leaving the carrier laser frequency unchanged. This difference in RF frequencies gives the D1 transition isotope shift once we know the hyperfine shifts (see figure 2.3).

as it cancels out. The hyperfine shifts are given by:

$$\nu_{HF} = \frac{A(g(e))}{2}[F(F+1) - I(I+1) - J(J+1)], \tag{4.2}$$

where $A(g(e))$ is the isotope-dependent hyperfine A coefficient of the ground (excited) state, determined by experimental measurement of the hyperfine splitting, I, J and F are the nuclear spin, electronic and total angular momentum quantum numbers, respectively. We obtain the hyperfine splittings of the excited $7P_{1/2}$ state for each isotope from our measurements and use literature values for the ground $7S_{1/2}$ state.

Our method of setting the carrier laser frequency between the hyperfine levels allows a clean extraction of the total $7P_{1/2}$ splitting independent of the exact carrier laser frequency. The difference of the observed transition centroids in a single scan is the hyperfine splitting; any shift in one centroid position caused by laser offset is cancelled by a corresponding shift in the other centroid, assuming there is no laser drift during a single RF sweep.

The probe laser frequency is locked to this midpoint frequency via a scanning Fabry-Perot cavity and a stabilized Melles-Griot 05-STP-901 HeNe laser, transferring the long-term stability of the HeNe to the other laser (details are provided in section 3.3.4). We keep the probe laser locked during the isotope change in the MOT. The probe laser is a Ti:Sapph laser operating at 817 nm; we send linearly polarized light into an EOSpace AZ-2K1-10-PFA-PFA-800-UL amplitude modulator for sideband generation. A fiber carries the probe light to the atoms, and the light is retro-reflected to minimize any pushing of the atoms as they scatter photons. The 10 mW/cm^2 in each sideband is enough to saturate the transition, and the fluorescence collects in our detection system (details below) when a sideband frequency is resonant with a hyperfine level.

Sidebands are generated by an RF signal applied to the fiber modulator, con-

sisting of a lithium niobate electro-optic modulator in one arm of a Mach-Zehnder interferometer. A YYLabs Mini-MBC-1 modulation bias controller card gives a bias voltage to the modulator to keep the carrier suppressed. This increases the power to the sidebands and reduces the scattered light from the carrier.

Two different RF synthesizer setups have been used to measure the isotope shifts. One, employed during the first experimental data collection period, involves Analog Devices AD4350 synthesizers mounted on a pair of UG-110 evaluation boards to generate the RF frequencies desired. The boards operate using a phase-locked loop (PLL) stabilized voltage controlled oscillator (VCO) referenced to a 10 MHz clock. A continuous output frequency sweep is performed by manipulating the input clock frequency using a Stanford Research Systems DS345 function generator. The scanning range (70 MHz) of one frequency synthesizer is limited to how far the clock can be moved off the nominal set point before the PLL is lost and the VCO becomes unlocked, resulting in output instability and unresponsiveness to further clock manipulation. This frequency-dependent range, along with the 4.4 GHz maximum frequency, limits the isotopes we could measure with these boards using ^{209}Fr as a reference. Two of the boards are employed along with a Mini-Circuits ZFSWA-2-46 RF switch synchronized with the clock sweep to pass the correct synthesizer output allowing for $\sim$140 MHz of continuous frequency scanning.

The second RF setup, used for the second data collection period, uses a Phase Matrix QuickSyn FSW-0020, a direct digital synthesizer using a fundamental VCO and PLL to generate frequencies from 0.5 - 20 GHz. This synthesizer allows us to tune the probe laser sidebands to any of the D1 transitions in the isotopes we trap.

The output sweep is digitally controlled stepwise at a maximum 7 kHz rate, giving us 70 frequency steps in the 10 ms allocated for each measurement. The probe lockpoint is maintained for all isotopes, and the sideband frequency is tuned to locate both D1 transitions for each isotope once it is trapped. Thus this setup has the additional advantage of not requiring a return to a reference isotope for each new measurement. The time saved is of great advantage when our beamtime is extremely limited in a multi-user facility like ISAC.

Fluorescence is collected by a double relay optical system and detected by a Hamamatsu H7422 photomultier tube (PMT). An interference filter centered at 820 nm and an edge filter with 795 nm cut-on wavelength are in place to block light other than the D1 line scattered photons in order to reduce background counts. A Stanford Research Systems SR430 multichannel scaler (MCS) collects the signal from the PMT as a function of time. The MOT operates with trap and repumper lasers on the D2 line at 718 nm and thus they do not contribute appreciably to the background.

In order to minimize AC Stark shifts [88] of the $7S_{1/2}$ ground state, the trap laser light is extinguished periodically during the 10 ms RF sweep on a 32 μs cycle of 50 MCS bins each 640 ns long. The chopping cycle is 21.76 μs (34 bins) with the light on, followed by 7.04 μs (11 bins) with the light extinguished by an acousto-optic modulator with a greater than 10^4 extinction factor, and ended by the remaining 3.2 μs (5 bins) with the light back on. The data acquisition system is collecting at all times and the data with the trap light off is separated in the analysis using a bin calibration performed offline.

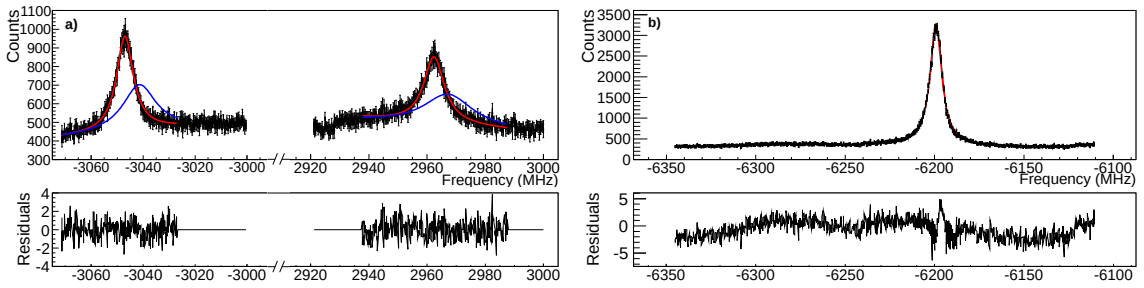

Figure 4.2: Data of a) the $7P_{1/2}$ splitting of ^{206}Fr and b) the reachable transition in ^{209}Fr using the AD4350 RF generator, along with the normalized residuals of their fits. The Lorentzian fits on a quadratic background are shown (red line). The blue lines show the AC Stark shifted peaks in the presence of the trapping laser light (data points not shown). Transitions are identified by knowing the directions of both the probe laser detuning from the midpoint and RF sweep.

4.3 Results

We measured the D1 isotope shifts for isotopes $^{206-213}$Fr with respect to ^{221}Fr. Analysis of the data yields the frequency difference between isotopes of the hyperfine transitions, which we used to calculate the isotope shift (see figure 2.3 and Eq. 4.1). The splittings of the $7P_{1/2}$ level were obtained by taking the difference of the sideband frequencies of the two transitions from a single scan (see figure 4.2a). Our reported isotope shifts are ultimately calculated with reference to ^{221}Fr, and we recalculated the literature D2 isotope shifts from reference ^{212}Fr to ^{221}Fr for the King plot analysis which follows.

4.3.1 Isotope shift data

The peaks in the data are fit with Lorentzians on a quadratic background using the ROOT analysis package to determine the centroid of each transition. We do not consider the effect of trap losses or nuclear decays on the fit, as the 10 ms scan length

is much shorter than the 20 s lifetime of the trap or the 15 second to 20 minute half-lives of the isotopes. Statistical uncertainties on the centroid frequencies from these fits are less than 100 kHz and in some cases less than 15 kHz. The peaks typically have Lorentzian widths of 8 MHz for data collected with the trap light off; this is partly due to saturation broadening of the 5.4 MHz natural linewidth, calculated from the measured lifetime of the $7P_{1/2}$ state [89].

An example scan is provided in figure 4.2 for the ^{206}Fr to ^{209}Fr D1 isotope shift. We determine the hyperfine splitting of the excited state from scans like a) where it is the difference of the centroids of both peaks. The reference isotope measurement for the isotope shift shows a single transition peak; the other is roughly 6 GHz away, well outside the range of our scan. Table 4.1 summarizes the results from all of the isotopes studied; the reported errors for the D1 isotope shifts are the quadratic sums of the measurement error, and hyperfine shift errors, calculated from A($S_{1/2}$) and A($P_{1/2}$) errors and nuclear spins, for both the measured isotopes and the reference ^{221}Fr. Additionally, we measured the $7P_{1/2}$ hyperfine splitting of ^{206}Fr^m ($t_{1/2} \approx 16$ s) to be 6524.3(6) MHz and the shifts with respect to ^{221}Fr for the D1 transition (i.e. RF frequencies $\nu_1 - \nu_2$) to be 11774(2) MHz for the transitions involving the lower $7P_{1/2}$ states and 15864(2) MHz for the upper $7P_{1/2}$ states. Without knowing the nuclear spin or the A($S_{1/2}$), we can not extract an isotope shift or A($P_{1/2}$) value from those measurements.

Table 4.1: Overview of our measurements and literature values that are relevant for calculating isotope shifts to be used for a King plot. Literature D2 isotope shifts ($\delta\nu_{IS}$) are reported with ^{212}Fr as the reference, with the exception of the ^{206}Fr D2 value, which is measured with respect to ^{208}Fr. They have been recalculated using the ^{212}Fr to ^{221}Fr isotope shift from [90] to be common with our D1 isotope shifts. Nuclear spins and A($S_{1/2}$) values are from literature and A($P_{1/2}$) are from our measurements [87]. The final isotope shift uncertainty is a combination of our measurement uncertainty and the A coefficient uncertainties needed to calculate the centers of gravity.

	this work		literature values			
Isotope	A($P_{1/2}$) (MHz)	D1$\delta\nu_{IS}$ (MHz)	Spin	A($S_{1/2}$) (MHz)	D2$\delta\nu_{IS}$ (MHz)	Source
206	1716.9(2)	29175(5)	3	13052.2(20)	30684(5)	[91]
207	1111.9(1)	27432(6)	9/2	8484.(1)	28809(5)	[90]
208	874.68(8)	27210(4)	7	6650.7(8)	28573(4)	[90]
209	1127.7(1)	25432(3)	9/2	8606.7(9)	26698(4)	[90, 92]
210	946.33(9)	24927(3)	6	7195.1(4)	26178(4)	[90, 92]
211	1142.1(1)	23300(5)	9/2	8713.9(8)	24465(4)	[90, 92]
212	1192.2(1)	22437(4)	5	9064.4(15)	23570(2)	[93, 90]
213	1147.9(1)	20869(7)	9/2	8757.4(19)	21929(3)	[93, 90]
221	811.5(2)	0	5/2	6209.9(10)	0	[93, 90]

4.3.2 Frequency axis calibration

Setting the AD4350 cards involves a multistep process in which the 10 MHz clock frequency must be manipulated to select the correct VCO for that card's scanning range. It is not immediately obvious exactly what scan range that will produce. Thus, to obtain the transition frequency difference, we calibrate the frequency of each MCS bin by measuring the output of our frequency generators. The outputs of the latter are mixed down using a Gigatronics 1026 synthesized signal generator and Mini-Circuits ZX05-43+ frequency mixer to allow the waveforms to be observed directly on an oscilloscope, where they are captured to be fit to sinusoids at fixed times during the 10 ms scan. The fitted frequencies show that both the AD cards and Phase Matrix synthesizer behave as expected so long as the AD cards remain phase-locked to their input clocks. All measured frequencies are as predicted, neglecting a few obvious outliers where inspection of the fit shows that the fitting routine failed those very few points, with uncertainties of less than 10 kHz. This enables us to construct a linear frequency-time correspondence of the RF which we use to calibrate the bin axis of the MCS to a frequency axis for our data.

4.3.3 Systematic errors

The dominant systematic effect in our isotope shift measurement is given by the laser lock drift; all other contributions are much smaller than this one. Other sources of systematic error are AC Stark shifts, Zeeman shifts and background contributions. These are more important for the hyperfine splitting measurement, as laser drift in this case causes a broadening but no shift in the observed transition energy.

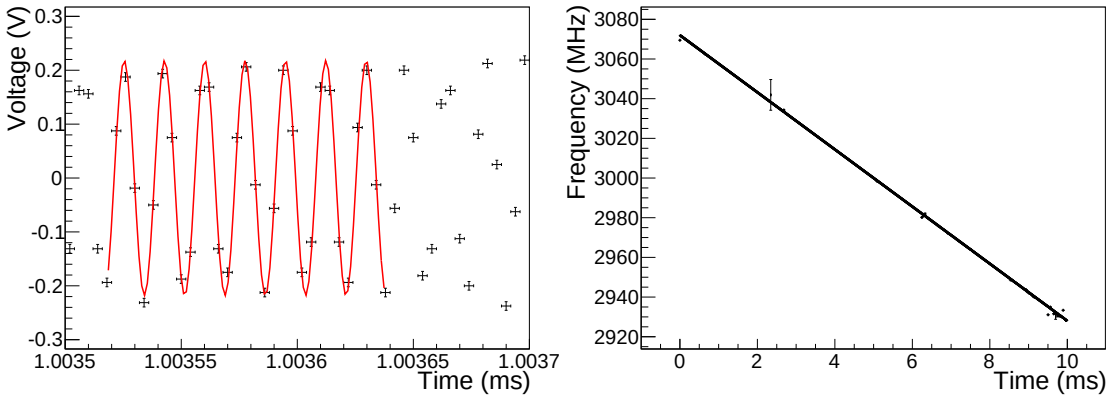

Figure 4.3: (Left) Data of the mixed-down frequency output of the setup with two AD4350 cards for the RF sweep of the ^{206}Fr hyperfine splitting. The red fit line gives us the frequency output at this time, once the mixing frequency is added back in. Many waveforms fitted periodically over the entire frequency sweep reproduce the expected frequency output of the cards. (Right) Frequency ramp produced from the individual fits, with the mixing frequency added in. The outliers are points for which a particular fit failed. The line produced from this plot is used to calibrate the bin frequency for the MCS data for this isotope.

Our laser-locking system exhibited slow drifts over the time between measurements as the isotope in the trap was changed. The latter involved changes in the mass separator of the ISAC facility as well as changing the laser frequencies and took between 30 to 60 minutes before the next isotope was measured. Long term observations of the Fabry-Perot cavity and helium-neon laser exhibited drifts below 3 MHz over periods of one hour for the system in use during the first experiment. The drift was determined by feeding into the cavity a laser stabilized via saturated absorption spectroscopy in rubidium. We discovered that the drift was largely due to uncontrolled feedback by back-reflection from optical surfaces into the HeNe laser, temperature drift-induced expansion of the cavity tube and non-linearity of the piezo scanning the cavity length. Thus, for our first isotope shift measurements, we conservatively place the sum of systematic errors at ± 3 MHz, dominated by the laser-lock

drift. Many of these laser stability issues were improved for the second set of measurements; we introduced an optical isolator to prevent feedback into the HeNe, the cavity was held under vacuum and was temperature-locked via PID control, and we locked the probe laser to a frequency such that its locking peak in the cavity nearly coincided with that of the HeNe, suppressing piezo nonlinearity effects on the measurement. Those improvements reduced the systematic error of the laser drifts to below ± 2 MHz.

An AC Stark shift of the ground state by the D2 line excitation is caused by the trap and repumper light, whose intensities are approximately 20 mW/cm^2 in the trapping beams and 5 mW/cm^2 in the repumping beams; all beams have $1/e^2$ power diameters of 5 cm. The typical detuning of the trap laser is about 15 MHz, roughly two and a half linewidths detuned to the red. This systematic is largely eliminated by chopping the trapping laser light while the RF sideband sweep is occuring. For the splitting measurements, any shift present is cancelled to first order by having the probe frequency set between the two transition frequencies; any change in the ground state shifts the measured transition frequencies the same amount, which cancels when taking the difference. The repumper frequency is set on the other hyperfine ground state, approximately 43 GHz away with some variation between isotopes, making its contribution to the Stark shift negligible. The AC Stark shift of the ground state from the off-resonance probe laser sideband is estimated at less than 180 kHz based on measured intensity and detunings.

A Zeeman shift is due to non-zero magnetic fields across the atom cloud in the trap and must be accounted for, as the quadrupole magnetic field of the MOT (with

gradient 7 G/cm strong axis) remained on when taking a measurement. The effect of the magnetic field is estimated by two methods; varying the current in the quadrupole coils generating the field and changing the polarization of the light exciting the D1 transition. The change in polarization will induce transitions between different magnetic sub-levels, or m_F states by the usual selection rules, each of which has a m_F-dependent Zeeman shift. Furthermore, even with perfectly linear light, we would still induce $\Delta m_F = 0, \pm 1$ due to the changing direction of the quadrupole field around the zero point. We performed these tests both online with francium and offline with rubidium; both alkalis have very similar behaviour in magnetic fields. Altogether, the measurements place an upper bound on the contribution to the systematic error by the magnetic field of 540 kHz.

Background counts are minimized by the spatial filtering of the imaging system: a double relay with an aperture at the image plane. An interference filter centered around 820 nm in front of the PMT and chopping the trap laser during measurement also reduce background counts. Additionally, proper control of the fiber modulator voltage bias greatly suppresses the intensity of the carrier output, reducing its contribution to background. We did observe fluctuations in the shape of the background underneath the transition peaks. These are likely caused by drifts in the phase between paths through the amplitude fiber modulator, due to small changes in temperature or bias voltage, resulting in more background light at the carrier frequency. Investigating this effect over many scans by fitting with different-order polynomials changes the fit centroid less than 100 kHz and we add this to the systematic uncertainty.

Additionally, there is a systematic uncertainty introduced from the literature A($S_{1/2}$) values we use to calculate the ground state hyperfine shift [91, 90, 92, 93] required to find the center of gravity and hence the isotope shift. Measurement of this quantity constitutes an entirely different experimental technique, and we do not currently have the means to measure these 40-50 GHz splittings ourselves. Therefore we add the 1-4 MHz uncertainties calculated from the published ground state values to our isotope shift measurement uncertainty.

4.4 King Plot Analysis

In all but the lightest nuclei, a King plot [65] separates the mass and field shift components of the isotope shift and allows comparison between different atomic transitions. The plot requires isotope shifts for two atomic transitions as well as the masses [94] of the isotopes measured. Our new measurements on the D1 line along with existing data for the D2 line [91, 90, 92] provide shifts in eight francium isotopes with respect to ^{221}Fr. Taking equation 2.38 for the D1 and D2 transitions, writing explicitly the mass factor and collecting terms into a single field shift constant for each transition, gives:

$$\left(\frac{M_A M_{A'}}{M_A - M_{A'}}\right)\delta\nu_{IS,D2} = (N_{D2}+S_{D2}) - (N_{D1}+S_{D1})\frac{F_{D2}}{F_{D1}} + \frac{F_{D2}}{F_{D1}}\left(\frac{M_A M_{A'}}{M_A - M_{A'}}\right)\delta\nu_{IS,D1}, \tag{4.3}$$

a linear equation in isotope shifts $\nu_{IS,i}$ weighted by isotopic masses, i.e. $\left(\frac{M_A M_{A'}}{M_A - M_{A'}}\right)\delta\nu_{IS}$, which we shall call the modified isotope shifts (MIS), with a slope given by the ratio of the field shift constants and intercept dependent on the differences in the mass shift constants. The normal mass shift can be calculated exactly; thus the intercept

can be used to determine the difference in specific mass shift constants. The slope corresponds to the differing electronic overlaps with the nucleus of the $7P_{1/2}$ and $7P_{3/2}$ states.

The King plot in figure 4.4 uses isotopes $^{206-213}$Fr, with ^{221}Fr as a reference; the isomer ^{206m}Fr is also included as the isotope shift constants are, to first order, no different for excited nuclei than for those in the ground state. We find that $F_{D2}/F_{D1} = 1.0521(8)$ and $(N_{D2} + S_{D2}) - (N_{D1} + S_{D1})\frac{F_{D2}}{F_{D1}} = 194(78)$ GHz amu with $\chi^2/ndf = 7.00094/7$. The normal mass shift constants are $N_{D1} = 201$ and $N_{D2} = 229$ GHz amu from equation 2.13 with negligible errors given by the uncertainty in atomic masses. This leaves the specific mass shift constant difference ($\delta\mathcal{S}$) between the two transitions $\delta\mathcal{S} = S_{D2} - S_{D1}\frac{F_{D2}}{F_{D1}} = 176(78)$ GHz amu.

The known corrections to the field shift from the electronic density changing over the nuclear volume (as discussed in section 2.3.2) depend on the nuclear charge distribution [67]. The corrections in $\delta\langle r^4\rangle$ and $\delta\langle r^6\rangle$ can be related in various basic nuclear charge distributions to the shape of the mean square charge radii $d\langle r^2\rangle/dA$, [69]. This quantity then shows odd-even staggering. However, such a phenomenological correction would be within the errors of our measurements, and an inspection of the residuals in figure 4.4 shows no significant difference between the odd-odd and odd-even isotopes. The effect is too small to be observed in our data.

Early isotope shifts in francium were measured with respect to ^{212}Fr. Using ^{212}Fr as the reference isotope shifts the King plot fit results for the present data. The χ^2/ndf is poorer at 9.76/7 and the slope has changed by 0.5σ to 1.0525(5), as shown in figure 4.5. The change in the fit is due to the systematic errors in the measurement

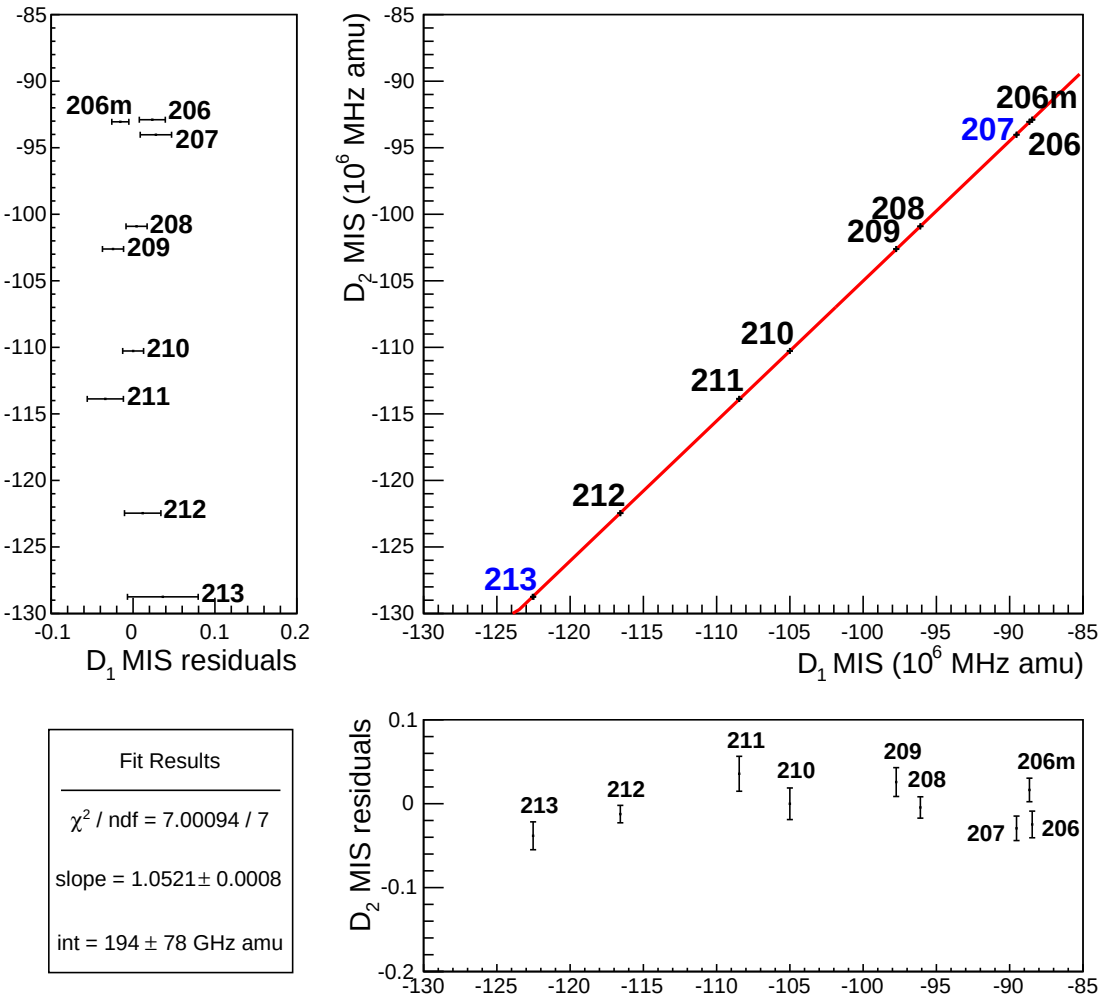

Figure 4.4: King plot of the modified isotope shifts (MIS) of the D2 and D1 lines for francium. Existing D2 line isotope shifts were recalculated using ^{221}Fr as the reference isotope. We provide new results for $^{206-213}$Fr D1 isotope shifts. The slope of the fitted line gives the ratio of the field shift constants for the two transitions. The intercept provides the corresponding difference in the mass shift constants. Plots of the D1 and D2 residuals are shown. The blue ^{207,213}Fr data points are from the first experimental run and the black $^{206(m),208-212}$Fr data points are from the second run.

of the reference isotope; that common error is now with respect to ^{212}Fr instead of ^{221}Fr. Furthemore, using ^{212}Fr as the reference puts the ^{221}Fr King plot point in a

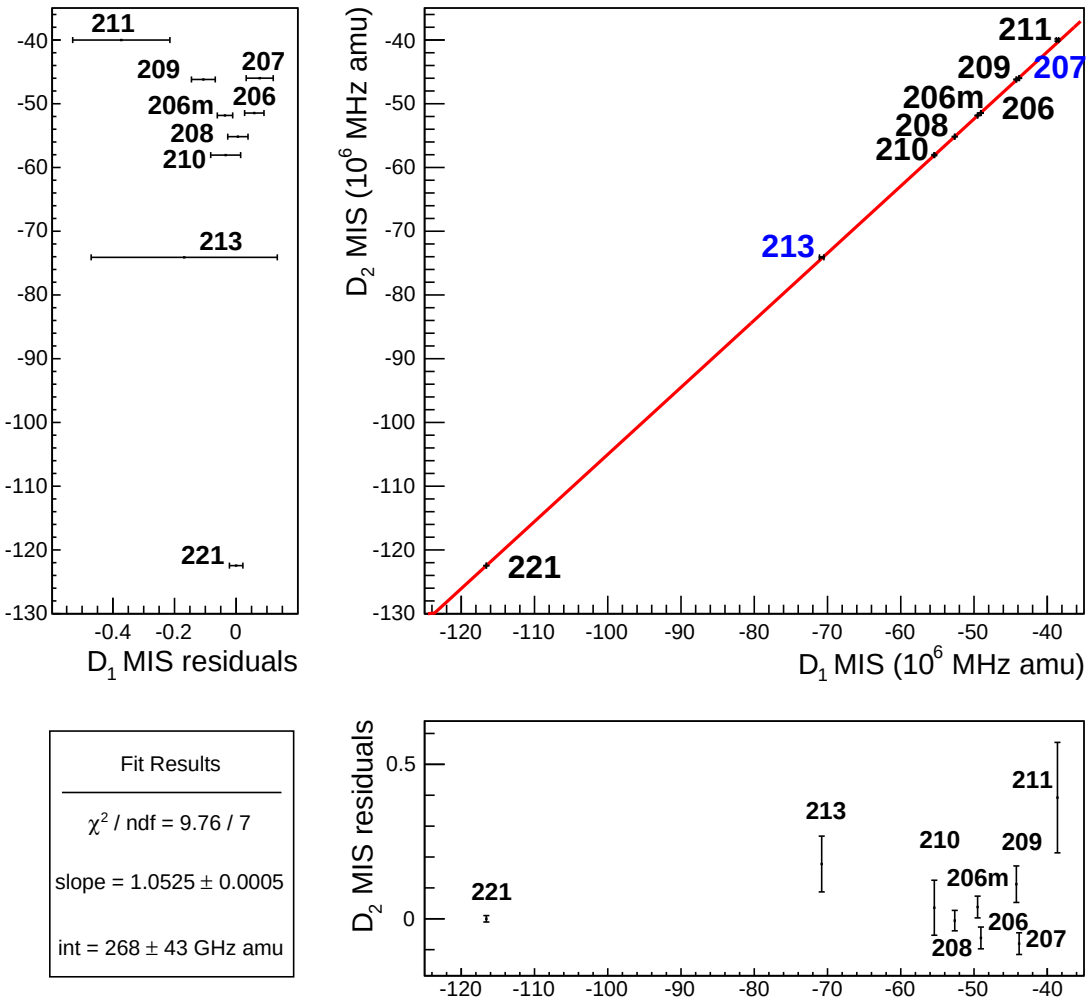

Figure 4.5: King plot of the modified isotope shifts (MIS) of the D2 and D1 lines for francium using ^{212}Fr as the reference isotope. Compare with figure 4.4 to notice the difference in the fit parameters. Changing the reference isotope results in the extraction of different isotope shift constant relations. Overall, the fit is poorer with this reference isotope.

location that dominates the fit due to the mass factor, as seen by its location and small error bar in figure 4.5. Therefore, we consider ^{221}Fr to be a better choice for the reference isotope.

4.5 Theory comparison

Calculations for the field shift and specific mass shift constants have been performed using several methods: many-body perturbation theory and closed-cluster approaches [64] as well as many-body perturbation theory calculation [95]. Our results and their predictions are summarized in table 4.2 for the field shifts and in table 4.3 for the specific mass shifts. In table 4.3, the finite field result uses the average of three different methods which vary in their consideration of higher order effects and the fourth column uses the (SD + E3) value from table 4.2 for F_{D2}/F_{D1} for the results from [64]. Using the (B0(Σ^∞)) value instead would cause no change at this sensitivity. The fit of the King plot agrees with the field shift constants predicted by the closed-cluster method (SD+E3) at the 1σ level and with the pertubation theory (B0(Σ^∞)) method at the 2σ level, and does not agree with the prediction from [95]. The specific mass shift constants extracted from this King plot intercept agree with the finite field and M-P results at the 1σ level and the perturbation theory at the 2σ level.

We can also fix the F_{D2}/F_{D1} ratio to theory and see what specific mass shift constants fit our data. The slope of the King plot is set in turn to the theory values and the resulting $\delta\mathcal{S}$ are displayed in table 4.3. These $\delta\mathcal{S}$ exhibit a linear trend as a function of field shift ratio. Fitting this line results in:

$$\delta\mathcal{S} = (102 \pm 2) \times 10^3 (\frac{F_{D2}}{F_{D1}} - 1.0520) + 170 \pm 7, \tag{4.4}$$

allowing a $\delta\mathcal{S}$ value (in GHz amu) to be calculated from our measurements for any future field shift theory predictions.

Table 4.2: Field shift constants (MHz/fm^2) of equation 2.15 obtained from three theoretical methods along with the experimental ratio obtained from the King plot analysis shown in figure 4.4.

Method	$F(7S_{1/2})$	$F(7P_{1/2})$	$F(7P_{3/2})$	F_{D2}/F_{D1}
BO(Σ^∞)[a]	-20463	-693	303	1.0504
SD + E3[a]	-20188	-640	361	1.0512
M-P[b]	-20782	-696	245	1.0468
expt. [this work]				1.0521(8)

[a] Dzuba, Johnson and Safronova [64]

[b] Mårtensson-Pendrill [95]

Table 4.3: Specific mass shift constants (GHz amu) of equation 2.14 obtained from three theoretical methods along with the experimental value obtained from the King plot analysis shown in figure 4.4. The results from fixing the King plot slope to the different theory values are also shown.

Method	$S(7S_{1/2})$	$S(7P_{1/2})$	$S(7P_{3/2})$	$\delta\mathcal{S}$
PT[a]	-786.1	-53	7.9	24
FF[a]	-237	-62	77	130
M-P[b]	-570	-154	-18	117
expt. [this work]				176(78)
fixed slope BO(Σ^∞)				90(9)
fixed slope SD + E3				8(9)
fixed slope M-P				-359(9)

[a] Perturbation theory and finite field approaches [64]

[b] Mårtensson-Pendrill [95]

The deviation from unity of our King plot slope corresponds to the difference in the overlap of the $7P_{1/2}$ and $7P_{3/2}$ states. Our experimental value for this is 0.0521(8), corresponding to a 2% measurement. We measure the total ratio 1.0521(8) to 0.1%, well below the stated 1% accuracy of the theory [64]. This analysis is limited by our reliance on previous D2 line measurements and the ground state hyperfine A coefficients extracted from those measurements. Our D1 isotope shift uncertainties are inflated by typically a factor of two due to the uncertainties of the ground state A coefficients alone, which are required to determine the center of gravity of the ground state. Improving the experimental result would require more precisely measuring both of these quantities.

4.6 Higher-order nuclear corrections

The exploration of the higher-order nuclear corrections considered in section 2.3.2 was initially motivated by a large disagreement between the King plot ^{206}Fr data point and the fit line [6]. This disagreement has since been resolved by an updated ^{206}Fr D2 isotope shift. Thus these nuclear corrections are no longer required for their original purpose, but we will still consider them to estimate the magnitude of the effect. First, the K values must be determined by calculating the change in charge radii $\delta\langle r^2\rangle$ from isotope shift experiments and using the values thus obtained to estimate $\delta\langle r^2\rangle/\delta A$.

This is complicated by different literature references using different values of the field shift constant F_{D2} to extract $\delta\langle r^2\rangle$; the ^{206}Fr value [91] employs a newer field shift constant [64], which is different from that used for other francium isotopes [90]. Thus, we will only use our D1 isotope shift values along with the best N, S, F_{D1} values

according to our King plot; they are $N_{D1} = 201$ GHz amu, $S_{D1} = -175$ GHz amu and $F_{D1} = -19548$ MHz/fm^2. Then the $\delta\langle r^2\rangle$ value for isotope ^{A}Fr is:

$$\delta\langle r^2\rangle = \left(IS_{D1} - (N_{D1} + S_{D1})\frac{M_A - M_{221}}{M_A M_{221}} \right) / F_{D1}. \tag{4.5}$$

Those $\delta\langle r^2\rangle$ values are calculated with respect to ^{221}Fr. Then $\delta\langle r^2\rangle/\delta A$ is available for each isotope and is determined with their second-nearest neighbours, to avoid effects of odd-even staggering. Explicitly, for ^{209}Fr:

$$\left(\frac{\delta\langle r^2\rangle}{\delta A}\right)_{209} = \frac{\delta\langle r^2\rangle_{211} - \delta\langle r^2\rangle_{207}}{4} \tag{4.6}$$

Finally, $K-1$ can be obtained by applying equation 2.50. The results are summarized in table 4.4. We assume $K(P_{3/2}) = 1$ for all isotopes, i.e. that state defaults to having no effect.

The theory F_t values [64] must be separated into their electronic and nuclear parts, which are isotope independent and dependent, respectively. We select the K value of ^{213}Fr as it is at the neutron shell closure $N = 126$. Table 4.5 displays the results for the three states involved in our King plot.

Next, we will estimate the magnitude of this isotopic effect. We will begin by examining the effect on the slope of the King plot line. Recall from equations 2.38 and 4.3 the slope is given by:

$$\frac{F_{D2}}{F_{D1}} = \frac{F(P_{3/2})K(P_{3/2}) - F(S_{1/2})K(S_{1/2})}{F(P_{1/2})K(P_{1/2}) - F(S_{1/2})K(S_{1/2})} \tag{4.7}$$

and hence the effect of an isotope-dependent slope (IDS) would shift where our data lie on the King plot of figure 4.4.

Begin by considering ^{209}Fr, the data point with the largest disagreement with the King plot, although only at roughly 1.5σ. Its mass factor $M_A M_{221}/(M_A - M_{221}) =$

Table 4.4: $\delta\langle r^2\rangle$ (fm^2) for francium isotopes, defined with respect to ^{221}Fr and calculated using the SD+E3 theory values of field shift constant F_{D1}. The slope $\delta\langle r^2\rangle/\delta A$ (fm^2/amu) is calculated for second-nearest neighbour, to eliminate the effect of odd-even staggering. The values for K are tabulated for both $S_{1/2}$ and $P_{1/2}$ states, with the S_n values for the $P_{1/2}$ state being 4% smaller [67].

Isotope	$\delta\langle r^2\rangle$	$\delta\langle r^2\rangle/\delta A$	$K(S_{1/2})-1$	$K(P_{1/2})-1$
206	-1.49292	0.050291	0.041176	0.039529
207	-1.40372	0.051186	0.042028	0.040347
208	-1.39233	0.054358	0.044576	0.042792
209	-1.30135	0.052874	0.043663	0.041916
210	-1.27548	0.061072	0.049902	0.047906
211	-1.19222	0.058386	0.048146	0.046220
212	-1.14805	0.063719	0.052248	0.050158
213	-1.06780	0.062209	0.051367	0.049312

Table 4.5: Separation of F, K from F_t. The K values used are for ^{213}Fr: $K(S_{1/2}) = 1.051, K(P_{1/2}) = 1.049, K(P_{3/2}) = 1$. All F, F_t values are in MHz/fm^2.

Calculation [64]	$F_t(S_{1/2})$	$F_t(P_{1/2})$	$F_t(P_{3/2})$	$F(S_{1/2})$	$F(P_{1/2})$	$F(P_{3/2})$
SD+E3	-20188	-640	361	-19202	-609	361

-3849 amu, which is used to convert differences in MIS to frequencies. For the original King plot, the difference in the data to fit line is 48 GHz amu, corresponding to -12.5 MHz. With the K correction, that disagreement becomes -25 MHz amu, or 6.4 MHz, a 19 MHz shift. The effect seems insensitive to the $\frac{\delta\langle r^2\rangle}{\delta A}$ values; the corrections remain approximately 20 MHz even for isotopes farther from the neutron

Table 4.6: IDS values given per isotope using second-neighbours to calculate charge radii slopes and the SD+E3 theory values. The D2 modified isotope shift (MIS) is then calculated using the D1 MIS, IDS, and the intercept from the original King plot fit (intercept = 176 GHz amu). This is compared with the D2 MIS from data and the original King plot prediction. MIS values are in GHz amu.

Isotope	F_{D2}/F_{D1}	D1 MIS	D2 MIS (data)	D2 MIS (IDS)	D2 MIS (King)
206	1.05140	-88460	-92895	-92831	-92893
207	1.05138	-89530	-94026	-93954	-94019
208	1.05134	-96094	-100906	-100851	-100924
209	1.05135	-97743	-102611	-102586	-102659
210	1.05123	-105002	-110274	-110206	-110296
211	1.05127	-108455	-113875	-113840	-113930
212	1.05119	-116573	-122460	-122365	-122471
213	1.05121	-122526	-128748	-128624	-128733

shell closure, resulting in a significant overcorrection for points in closer agreement to the linear King plot fit. This can be attributed to the simple liquid drop model calculation of the nuclear correction. It is insufficient for this purpose.

4.7 Summary

In this chapter, we have measured isotope shifts of the D1 line in $^{206-213}$Fr with respect to ^{221}Fr using a fast RF sweep of laser sidebands. A King plot allowed us to separate the field shifts ratio, $F_{D2}/F_{D1} = 1.0521(8)$, and mass shifts in these isotopes, and we deduced the specific mass shifts relation, $S_{D2} - S_{D1}\frac{F_{D2}}{F_{D1}} = 176(78)$ GHz amu,

in good agreement with the theory predictions. The measurements do not support employing the higher order nuclear effects based on a liquid drop nuclear model, as discussed in section 2.3.2.

Chapter 5

Photoionization cross-section of francium

5.1 Introduction

The photoionization cross-section is an indirectly important quantity in the parity violation experiment. We wish to use a power buildup cavity to enhance our $7S-8S$ excitation rates. The ionization potential of ^{221}Fr is 4.07 eV, and the 506 nm $7S-8S$ transition photon has an energy of 2.45 eV, calculated from wavenumbers in [86]. Thus a state with energy 1.63 eV above ground is susceptible to photoionization, neglecting non-linear effects such as two-photon excitations. The $7P_{3/2}$ state at 1.73 eV lies above that energy but the $7P_{1/2}$ state at 1.52 eV does not. Figure 5.1 displays the relevant energy levels and shows which states the 506 nm green light can photoionize.

If photoionization occurs too readily from the $7P_{3/2}$ excited state where a significant amount of the population traverses during the decay from the $8S$ state to

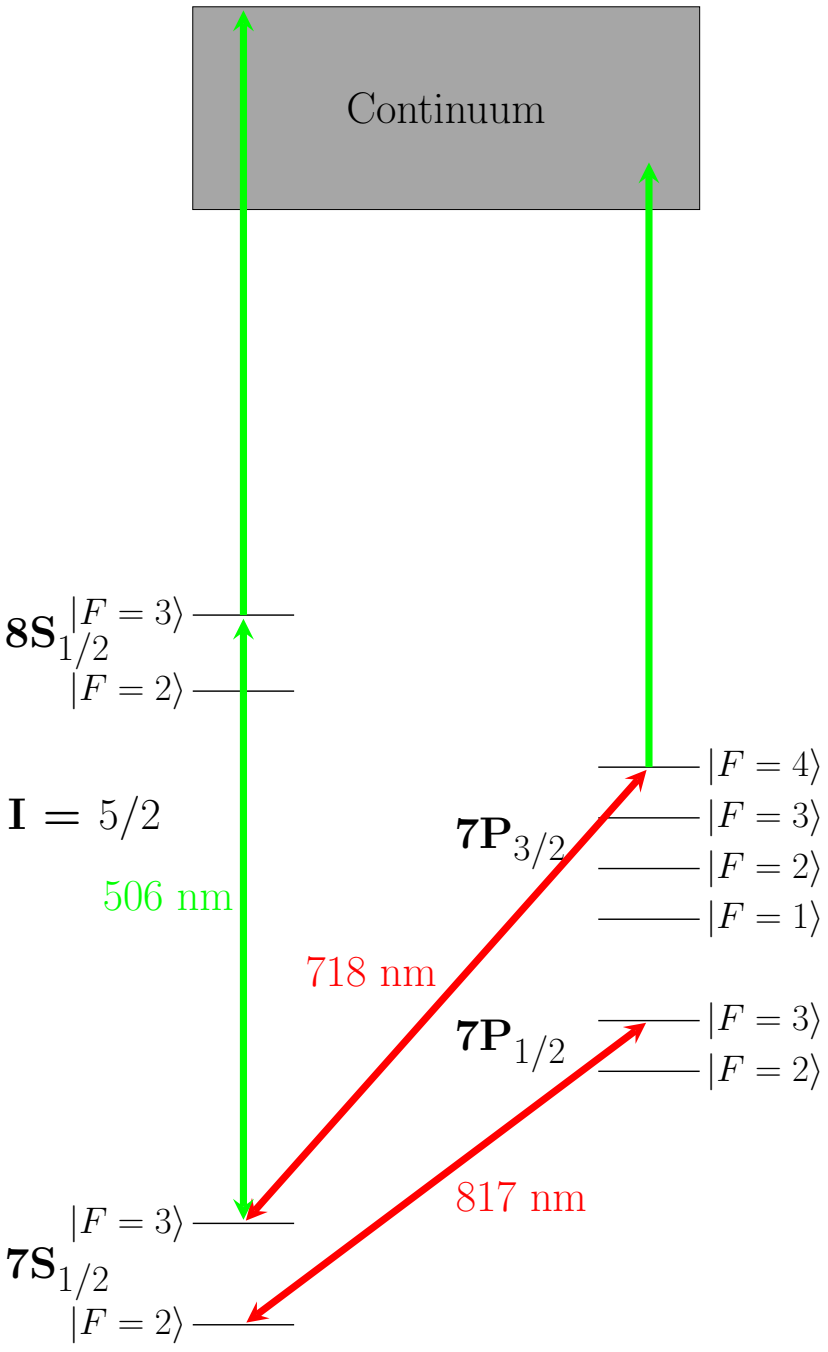

Figure 5.1: Energy level diagram of francium showing the 718 nm and 817 nm trapping transitions (red) as well as the 506 nm $7S-8S$ transition (green). The 506 nm photon has sufficient energy to photoionize both the $8S$ and $7P_{3/2}$ states but not the $7P_{1/2}$ state.

ground, the losses would defeat the advantage of trapping by preventing many $7S-8S$ transitions per atom. Thus we would be forced to operate in a scheme where the 506 nm $7S-8S$ light is not intense enough to cause this problem, likely by reducing the effectiveness of the power buildup cavity or reducing the light intensity. It should be stressed that this measurement will be used to empirically estimate the magnitude of an effect and will not be compared with a theoretical calculation of the photoionization cross-section of the $7P$ states in francium, as we are unaware of any such calculation for those states.

High precision, absolute measurements of photoionization cross-sections are difficult to achieve for several reasons. Most notable are the requirements for the absolute number of atoms, determining the absolute photon flux, and efficient ion counting [96, 97].

The use of a MOT allows for alternative techniques to be employed that are not possible in a beam experiment [98]. The MOT lifetime is determined by a combination of effects, each of which removes atoms from the trap. Typically, for long-lived traps, trap loss is dominated by collisions with background gas, and hence the residual pressure is usually the chief concern. If the trapped species is unstable, the radioactive lifetime must also be considered, and the total loss rate is the sum of all mechanisms, producing an exponential decay of trapped atoms. This is the case for francium, having no stable isotopes. The number of atoms in the trap at time t is $N(t)$, and N_0 atoms are present at $t = 0$. The relation is given by:

$$N = N_0 e^{-t(1/\tau_1 + 1/\tau_2)} = N_0 e^{-Rt}, \tag{5.1}$$

where τ_i is the lifetime determined from a single trap loss mechanism, such as collisions

with background (τ_1) or radioactive decay (τ_2), and R is the combined loss rate per atom from the all of the mechanisms.

The addition of photoionization introduces another loss mechanism; ions do not experience the resonant radiative forces of the MOT and are thereby lost. With the only difference being the presence of the ionizing light, the change in the trap lifetime is fully attributed to photoionization and we use this to calculate the cross-section [98]. Thus, the photoionization rate R_{PI} is determined by

$$R_{\mathrm{PI}} = \frac{1}{\tau_{\mathrm{on}}} - \frac{1}{\tau_{\mathrm{off}}}, \tag{5.2}$$

where $\tau_{\mathrm{on,\ (off)}}$ is the trap lifetime with the photoionizing light on(off). If one photon only has sufficient energy to photoionize from a single populated state in the MOT, we can identify the photoionization rate as coming from that state, neglecting higher order effects such as two-photon excitations or photoassociation. Once the photoionization rate is known, the cross-section from that excited state (e) can be calculated from [98]:

$$\sigma = \frac{R_{\mathrm{PI}}}{n_e \Phi}, \tag{5.3}$$

where n_e is the fraction of trapped atoms in the excited state from which photoionization occurs and $\Phi = I/h\nu$ is the photon flux (photons s^{-1} cm^{-2}) of the ionizing light of intensity I ($\mathrm{W/cm}^2$) at frequency ν. The excited state fraction is determined from the conditions of the MOT and the properties of the trapped isotope. This equation is valid in the regime where the target atoms experience the full photon flux, i.e. the density is not large enough that absorption decreases the flux for atoms deeper in the atom cloud.

This technique has the advantage of not needing to know the absolute number of

atoms interacting with the ionizing light; it only requires knowledge of the fraction of atoms involved in the interaction. This quantity corresponds to the fraction of atoms in an excited state and is calculated from the set parameters of the trap. Another advantage of this technique is that determining the trap lifetime to obtain the photoionization rate is a fluorescence measurement. Thus it does not require any ion detection and can therefore be carried out in the capture MOT.

5.2 Experimental Method

It must be stated that this was an *ad hoc*, unplanned measurement conducted during the last hours of a beamtime with a quickly-ordered commercial laser. As such, we do not achieve the precision that would otherwise be expected for a photoionization cross-section using this technique.

The photoionization measurement occured on a sample of ^{221}Fr contained within the MOT, which has a radioactive half-life of 4.8 minutes. The latter was sufficiently long that we did not need to account for nuclear decay during our lifetime measurements. We measured the change in the trap lifetime when 442 nm ionizing laser light was applied compared to the lifetime when that light was blocked. We used a 442 nm laser as we had not yet acquired our 506 nm laser at the time of this experiment.

The 442±2 nm light was from an unregulated Laserglow Polaris-200 battery powered diode laser calibrated by a simple grating spectrometer, which was in turn calibrated using the 436 nm mercury line. The light was transported through an optical fiber and collimated to a 5 mm beam, whose spatial profile was measured using a calibrated iris and photodiode. To determine the alignment of the photoionization

beam with the MOT, rubidium atoms were trapped after the francium measurement in the same location, and light resonant with the 780 nm rubidium D2 line was sent through the fiber. The calibrated aperture was adjusted until the probe light was observed to destroy the MOT on the camera image. This found how off-center the beam position was, which we found to be 1.5 to 3 mm. Combined with a power measurement, we determined the light intensity incident on the atom cloud to be 41 $\pm$ 6 mW/cm^2, including a correction for reflections from the surfaces of the glass cell, and this corresponded to a photon flux of $\Phi = 9.1 \pm 1.3 \times 10^{16}\text{s}^{-1}$ cm^{-2}.

The photoionizing laser was powered by batteries. It was not known during the experimental run that the laser exhibited a gradual decrease in output power as the batteries were depleted. This was only noticed after the data collection was finished. Afterwards, we created a time profile of this behaviour using a new set of batteries and matched it to the few data points collected at the end of the life of the first set. The time profile was scaled to match the endlife behaviour of both sets of batteries. An observation of the time of data collection (as shown in figure 5.2) shows that the laser power loss begins during that time. However, before that point, the laser power was fairly constant. Thus, we used the earlier data to avoid this decreasing power issue.

The MOT fluorescence was measured by a CCD camera and the recorded integrated signal was analyzed to determine the trap lifetime. An absolute calibration of the camera count-to-atoms was not required as we only needed the change in fluorescence to fit the lifetime. As we were not saturating the CCD chip, the camera response was linear in the fluorescence intensity and we could determine the trap lifetime by

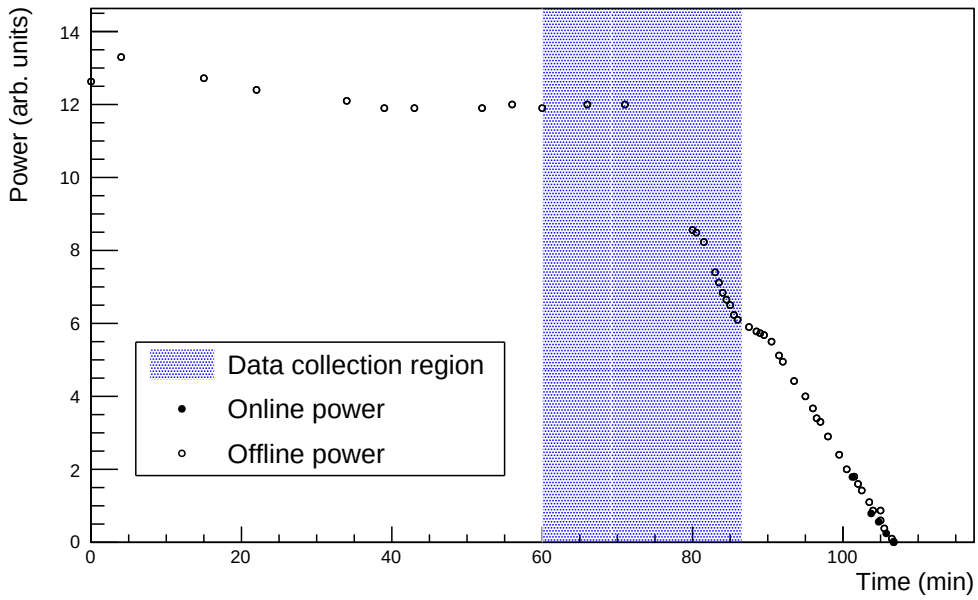

Figure 5.2: Plot of the power output of the 442 nm laser over time. Online power measurements were taken during the experimental run, after it was noticed that the batteries were depleting quickly. Offline power measurements were from a fresh set of batteries from the same lot as the first. The power was scaled to match the slopes of both sets of data points. The shaded area denotes the time of data collection (displayed in figure 5.4), which contains the data used in the calculation of the photoionization cross-section. Note that for the first half, the laser power remained near maximum.

fitting simple exponentials.

5.3 Results

The photoionization cross-section analysis has two parts. First, the excited state fraction needs to be determined. This is accomplished by employing a rate equation comprising the relevant states on or near resonance with the laser light involved in trapping. The 442 nm laser light is of sufficient energy to photoionize not only

the $7P_{3/2}$ level but the $7P_{1/2}$ level as well. We find that five levels are needed to accurately represent the system, covering the states coupled by the trapping laser on the D2 transition and those coupled by the repumper laser on the D1. Next, the CCD camera data must be fitted to determine the trap lifetimes with and without the photoionizing light. Then we combine these results to determine the photoionization cross-section according to equation 5.3.

5.3.1 Excited state fraction

The fraction of trapped atoms in the excited state is determined by a five-level rate equation. The levels involved are those at or near-resonance with either the trapping or repumping laser, as shown in figure 5.3. Also included is the $|F = 3\rangle$ $7P_{3/2}$ level with natural linewidth 7.57 MHz [89] separated from the $|F = 4\rangle$ level by 58 MHz [99], which is close enough to the trapping laser frequency such that its Gaussian extent is appreciable enough to cause a non-negligible population.

We use both ground states, the top two $7P_{3/2}$ states and the top $7P_{1/2}$ state for this calculation. These levels are coupled by the trapping and repumping lasers. The other excited states are not included; the relatively large hyperfine splittings make their steady-state populations in the trap negligible ($< 10^{-4}$). The detailed calculations are in Appendix B. The total excited state fraction $n_e(\text{full}) = 0.144 \pm 0.025$.

The contribution from the $7P_{1/2}$ state is negligible within the uncertainty of the $F' = 4$ excited state fraction, $n_e(7P_{1/2}) = 0.0085 \pm 0.0038$. For alkali atoms, there are only small differences in the cross-sections of the $nP_{1/2}$ and $nP_{3/2}$ states for the same photon energies [100, 97]. Thus, we will ignore the effect of the difference between

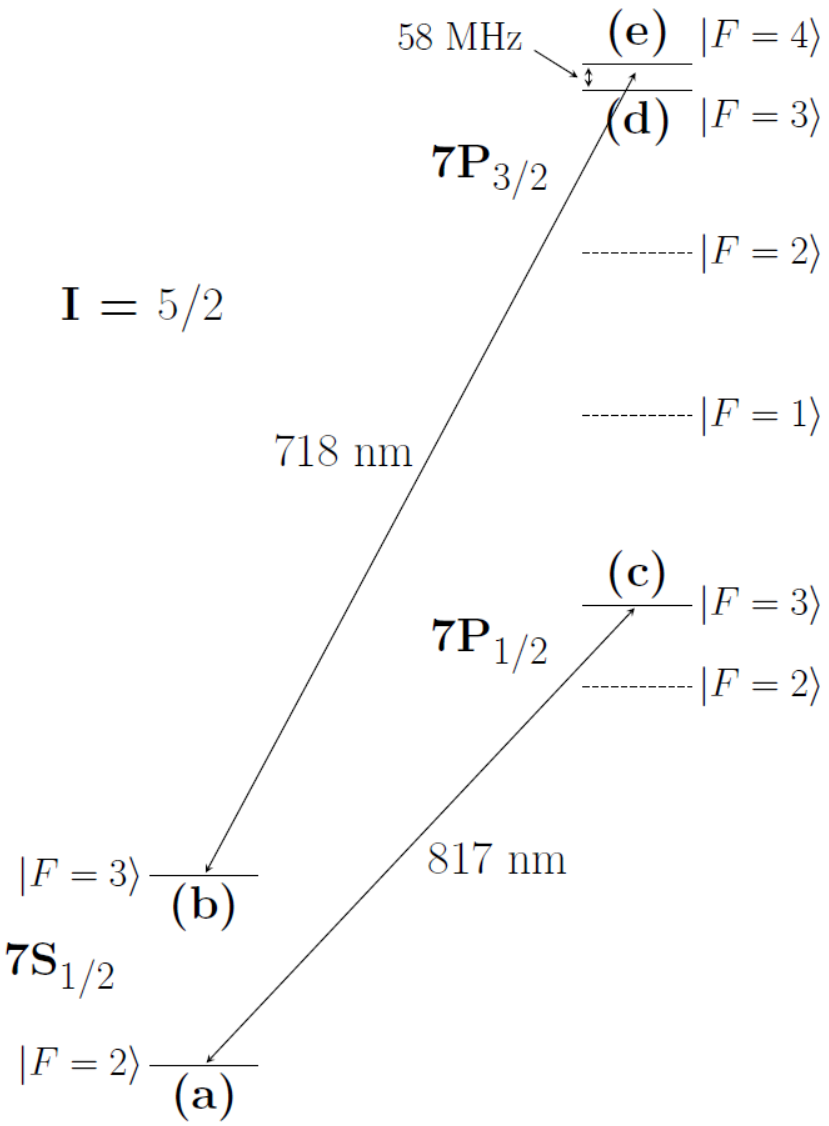

Figure 5.3: ^{221}Fr energy levels involved in the rate equation. The trap (718 nm) and repump (817 nm) lasers couple the solid-lined levels such that in the steady-state, those levels have non-zero population. Dash-lined levels are sufficiently detuned from the lasers to not be involved. The state labels (a-e) denote the shorthand used for the rate equation. Only the splittings of the $7P_{3/2}$ level are to scale with one another.

the cross-sections of the two states for this small $7P_{1/2}$ fraction of the excited state population.

5.3.2 Trap lifetimes

There were many *ad hoc* techniques applied during this experiment in order to make a good measurement of the photoionization cross-section. A quick review of the whole dataset shows that the best conditions with the most contrast between 442 nm light on/off occured when the light was cycled between successive 20 second trapping cycles. However, recall that the 442 nm laser power was declining during the data collection period, as shown in figure 5.2. Thus the very late cycles are not useful for extracting the photoionzation cross-section, as there was very little power available.

We look primarily at two regions in the entire dataset shown in figure 5.4, where the time axis is recorded in camera frame number since the beginning of the record; the first region begins roughly at frame 700 ("region A") and the second at frame 1600 ("region B"). The timestamps assigned to each frame by the camera control and data acquisition program allow us to calibrate the time axis, with frames being spaced by approximately 0.7 s. We do not know the exact laser power in region B. From figure 5.2, we can estimate it to be approximately half of the power from region A, when the laser output was still near full power. Additionally, at frame 1600, the power was deliberately halved by a waveplate-polarizing beamsplitter combination. Combined with the output power drop, the power in region B was very approximately one-quarter that of region A; we can use the result from region B as a consistency check but the uncertainty limits its use as an independent photoionization cross-section measurement.

First, we fit the peaks in region A, as shown in figure 5.5. We fit the peaks to simple exponentials (equation 5.1) on a fixed, constant background. The background

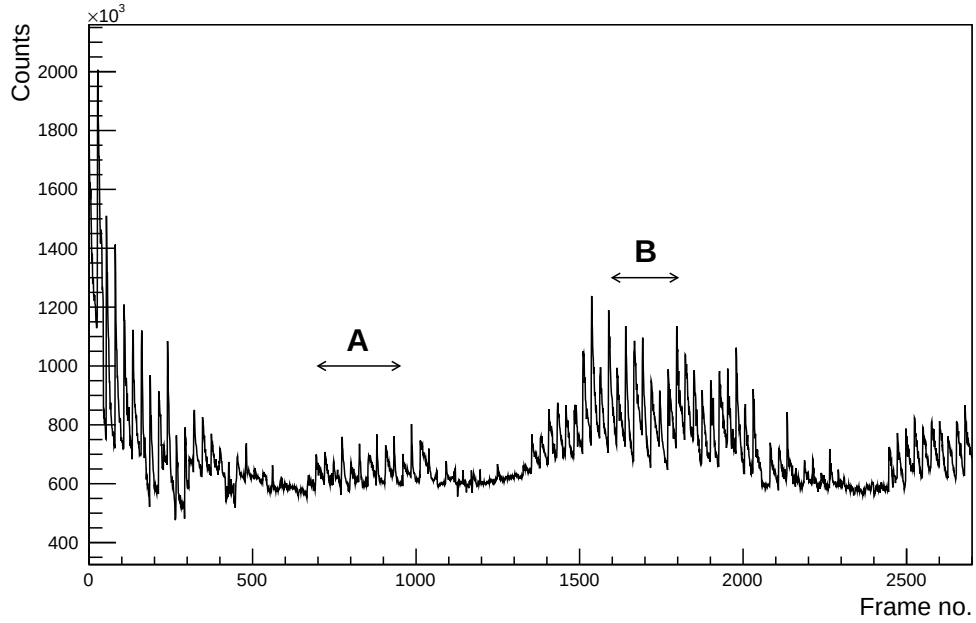

Figure 5.4: Full dataset of the photoionzation cross-section measurement showing fluorescence counts recorded by the camera focused on the trap. The regions used for further analysis begin at frames 700 (region A) and 1600 (region B) where the 442 nm light was alternatively blocked and unblocked between successive 20 second trapping cycles. A frame is approximately 0.7 s long.

level is determined by observing the data around region A when the trap was void of atoms. Additionally, we check that this background level is consistent with the data between short lifetime peaks when most atoms have been lost. We observe significant noise on the data and attribute it to fluctuations in trap laser power since it also appears where there are no atoms in the trap. This makes fitting difficult as we lose numerical criteria to judge the quality of the fit, i.e. the χ^2 of any fit is very large. Instead, we must judge if the fits are reasonable *by eye* and accept the relatively large variation in results as an increased source of error.

Of note is the increase of fluorescence signal when the 442 nm light is applied.

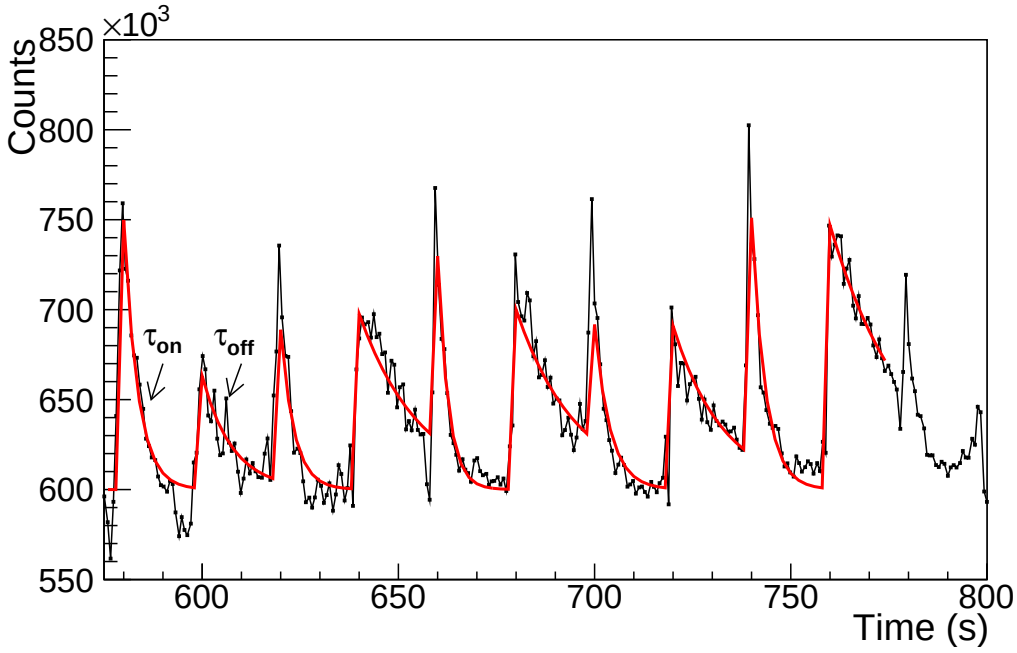

Figure 5.5: Data from region A, beginning at frame 700, showing peaks with alternating 442 nm light on/off.

Since those peaks also fit to reasonable exponentials, we conclude that additional atoms must be present from photoadsorption of francium either on the yttrium foil or the glass cell walls [101]. This does not have an effect on the trap lifetime; there are simply more atoms present for these pulses.

Next, we fit the peaks of region B using the same method as region A, as shown in figure 5.6. The exponentials with the 442 nm light on have a noticeably longer lifetime than their counterparts in region A. This is due to the decreased photoionizing power, attributed to both the deliberate splitting of the beam and the unintentional depletion of the batteries in the laser. While there may also be an increase in the lifetime of the light-off peaks, it is minor and likely due to changing MOT conditions, such as trapping laser drift. The lifetimes fitted from region A are summarized in

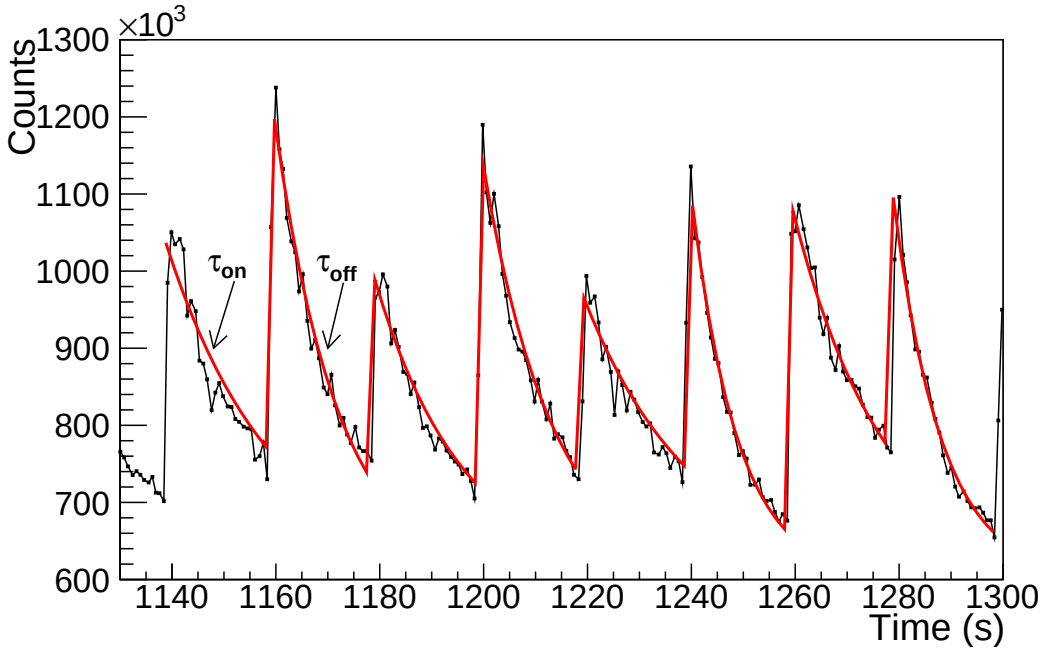

Figure 5.6: Data from region B, beginning at frame 1600, showing peaks with alternating 442 nm light on/off. This region has approximately one-quarter the photoionizing laser power of region A.

Table 5.1 and from region B in Table 5.2.

The average lifetimes are converted to loss rates, and then subtracted to extract the loss rate due to photoionization according to equation 5.2. For region A we find $R^A_{\mathrm{PI}} = 0.230 \pm 0.031$ s^{-1} and for region B $R^B_{\mathrm{PI}} = 0.043 \pm 0.012$ s^{-1}. Taking the ratio $R^A/R^B = 5.3$ suggests that the photoionizing blue light had 5.3 times more power in region A than in region B, which is consistent with our estimate considering the uncertainties involved.

Table 5.1: Exponential lifetimes obtained by fitting peaks shown in figure 5.5 (region A). The weighted averages have their errors inflated by their $\sqrt{\chi^2/\nu}$.

τ_{on} (s)	τ_{off} (s)
3.6 ± 0.4	7.7 ± 2.8
3.4 ± 0.5	15.8 ± 2.9
2.7 ± 0.3	15.4 ± 2.8
4.0 ± 0.5	12.8 ± 1.7
3.6 ± 0.5	19.5 ± 3.7
average: τ_{on} =3.29 ± 0.24 s	average: τ_{off} = 13.5 ± 1.6 s

Table 5.2: Exponential lifetimes obtained by fitting peaks shown in figure 5.6 (region B). The weighted averages have their errors inflated by their $\sqrt{\chi^2/\nu}$.

τ_{on} (s)	τ_{off} (s)
12.2 ± 0.7	20.7 ± 1.9
13.4 ± 0.9	17.1 ± 1.6
8.8 ± 0.6	21.3 ± 2.6
9.2 ± 0.6	17.9 ± 1.4
average: τ_{on} =10.4 ± 1.0 s	average: τ_{off} = 18.63 ± 0.93 s

5.3.3 Photoionization cross-section calculation and comparison to other alkalis

We now have all the pieces required to calculate the photoionization cross-section using the data from region A, the excited state fraction, the laser power measurement and equation 5.3.

$$\sigma = \frac{R_{\mathrm{PI}}}{n_e \Phi} = \frac{0.230 \pm 0.031}{(0.144 \pm 0.025)(9.1 \pm 1.3 \times 10^{16})}$$
$$= 1.75 \pm 0.46 \times 10^{-17}\ cm^2. \tag{5.4}$$

Thus, the photoionization cross-section of ^{221}Fr by 442 nm light is $1.75 \pm 0.46 \times 10^{-17}$ cm^2 or 17.5 ± 4.6 Mb.

A review of photoionization cross-sections of excited alkali atoms can be found in [100]. This contains theoretical treatments of the other alkali elements, showing the photoionization cross-sections for different photoelectron energies, for different calculations. For our 442 nm light photoionizing the $7P_{3/2}$ state, the photoelectron energy is $E_e = 0.46$ eV. We can obtain experimental cross-sections near our photoelectron energy and compare with our result for francium. Table 5.3 summarizes the published numbers near $E_e = 0.46$ and we interpolate the potassium value to project a cross-section closer to 0.46 eV. The cross-sections are plotted in Figure 5.7.

5.4 Application to a parity violation measurement in francium

With the photoionization cross-section in francium now experimentally quantified, we can estimate its effect on our future atomic parity violation measurement. First, we must account for the parity violation experiment using a different wavelength photon than this photoionization measurement. A 506 nm photon will produce a 0.10 eV photoelectron from the $7P_{3/2}$ state of francium or a 0.82 eV photoelectron

Table 5.3: Photoionization cross-section measurements of first excited $P_{3/2}$ state for photoelectron energies near 0.46 eV.

Element	Photoionization cross-section (Mb)	Photoelectron energy (eV)	Reference
Na	3.7 ± 0.7	0.48	[96]
Na	4.8 ± 1.2	0.47	[102]
K	7.3 ± 1.1	0.21	[100]
K	7.0 ± 1.0	0.81	[100]
Rb	12.5 ± 1.1	0.46	[98]
Rb	13.6 ± 1.2	0.41	[98]
Cs	16.5 ± 1.2	0.40	[97]
Cs	14.0 ± 1.4	0.62	[97]
Cs	8.1 ± 1.0	0.50	[103]
Cs	11.5 ± 1.0	0.50	[103]
Fr	17.5 ± 4.6	0.46	this work

from the $8S_{1/2}$ state. Experimental measurements and theory predictions in cesium have cross-sections approximately 30% larger at 0.1 eV photoelectron energy than at 0.5 eV energy. The cross-section at 0.8 eV photoelectron energy is approximately 30% smaller than at 0.5 eV. Furthermore, the measurement of the photoionization cross-section of the $7S_{1/2}$ state in cesium [104] shows that is it roughly 1% that of a $6P$ state [103], for the same photoelectron energy. Thus, the photoionization rate of the $8S_{1/2}$ state is greatly suppresed compared to the rate from the $7P_{3/2}$ state in francium, and we will neglect its contribution in the following discussion. We estimate the photoionization cross-section at 506 nm to be approximately 22 Mb from scaling

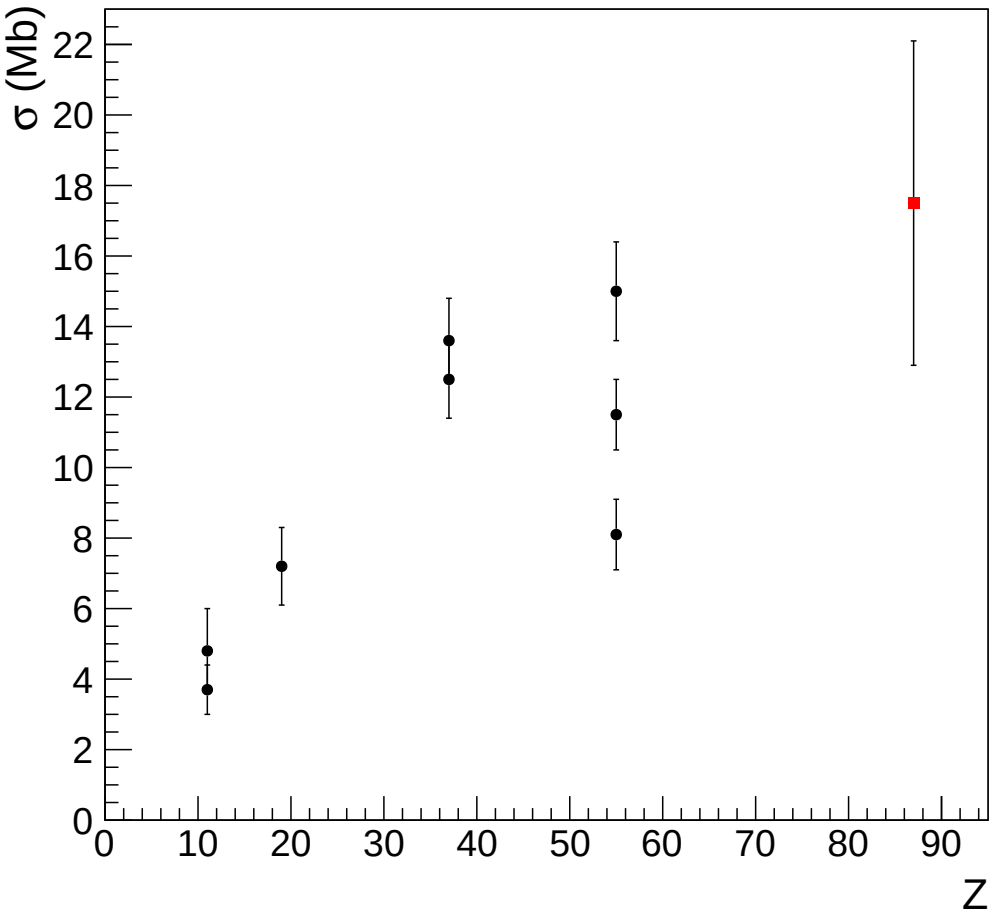

Figure 5.7: Comparison of experimental photoionization cross-sections for the first excited $nP_{3/2}$ state of the alkali elements (Na, K, Rb, Cs and Fr) for photoelectron energies near 0.45 eV. The new francium measurement (Z=87) follows the general trend set by the lighter alkali atoms.

the 442 nm measurement of the $7P$ states.

In the parity violation measurement, an electron is excited through the $7S - 8S$ transition and decays through a $7P$ state to ground. The likelihood of that electron passing through the $7P_{3/2}$ state is statistically determined by the angular momentum couplings. For alkali atoms like francium, this probability is $P(P_{3/2}) = 0.67$. Electrons

in a $7P_{3/2}$ state may be photoionized with probability:

$$P_{PI} = \left[\frac{\sigma I/h\nu}{\sigma I/h\nu + 1/\tau}\right] = \left[\frac{\sigma\tau I/h\nu}{\sigma\tau I/h\nu + 1}\right], \tag{5.5}$$

recalling that $I/h\nu$ is the 506 nm photon flux, σ is the photoionization cross-section and τ is the lifetime of the state. This is the ratio of the rate of photoionization versus the total rate of the electron leaving the $7P_{3/2}$ state, and it tends to unity at high light intensity.

Next, we need to determine the transition rate for the $7S - 8S$ excitation. The quoted rate per atom for the $6S - 7S$ cesium experiment is [105]:

$$R_{Cs} = 6 \times 10^{-2} E^2 (\mathrm{s}^{-1}), \tag{5.6}$$

where E is the applied Stark field in V/cm and the small APV amplitude is neglected. This rate is for their "current maximum laser intensity", which we will assume to be the 800 kW/cm^2 in the long report on their measurement [3]; this is inside their finely tuned power buildup cavity. Furthermore, this is determined from a transition induced by the vector transition polarizability $\beta = 27.02(8)$ atomic units (a.u.) [33]. To estimate R for a francium measurement, we will have to scale by the difference in intensities and transition polarizabilities. For francium, the theory value is $\beta = 74.3(7)$ a.u. [106]. Using the typical electric field strength of 500 V/cm for the cesium experiment [3], the $7S - 8S$ transition rate for francium is estimated to be:

$$\begin{aligned} R_{7S-8S} &= 6 \times 10^{-2} (500)^2 \ [I/(8 \times 10^5)](74.3/27.02) \\ &\approx 0.0516 \ I(\mathrm{s}^{-1}), \end{aligned} \tag{5.7}$$

where I is the intensity of the 506 nm laser in W/cm^2.

Then the loss rate due to photoionization is estimated to be:

$$\begin{aligned} R_{PI} &= R_{7S-8S} P(P_{3/2}) P_{PI} \\ &= \frac{4.18 \times 10^{-8} I^2}{1.22 \times 10^{-6} I + 1}, \end{aligned} \tag{5.8}$$

which tends to $P(P_{3/2})R_{7S-8S}$ at high light intensity, i.e. everything that passes through the $7P_{3/2}$ state is photoionized.

The intensity limit will be set by the operational parameters of the APV experiment. If we operate on a 10 s measurement period, we would want a similar trap lifetime for the atoms, and, only considering photoionization, the acceptable loss rate would be $R_T = 0.1$ s^{-1} per atom. Also, chopping the 506 nm light on an upper limit 4 ms light-on excitation followed by 6 ms of light-off retrapping cycle increases the acceptable loss rate to $R_T = 0.25$ s^{-1} per atom. Setting this equal to R_{PI} in equation 5.8 gives a modest intensity limit $I = 2450$ W/cm^2. At that intensity, the $7S - 8S$ excitation rate is 51 s^{-1} per atom, using equation 5.7 and accounting for chopping the 506 nm light.

In cesium, the oscillator strength of the pure APV transition is $f_{APV} \approx 10^{-22}$ and the pure Stark-induced transition is $f_{Stark} \approx 10^{-11}$ for an applied field of 500 V/cm [3]. The interference term is then $2A_{Stark}A_{APV} \approx 6 \times 10^{-17}$, resulting in an asymmetry of roughly 6×10^{-6} upon a parity reversal of the system. In francium, where the APV effect is predicted to be $20\times$ larger, the asymmetry is roughly 10^{-4}. We can use this to estimate a signal-to-noise (S/N) for our parity violation measurement:

$$S/N = A\sqrt{RtN}, \tag{5.9}$$

where our signal is the modulation given by the asymmetry A on the total number

of counts from N atoms excited at rate R for time t, in seconds, with the noise being purely statistical on that number of counts. Rearranging to determine the time needed for a certain precision given a number of trapped atoms produces table 5.4.

Table 5.4: Predicted data collection times for statistical precisions for given numbers of trapped atoms. Quantifying and reducing systematic errors will take longer.

Precision	number of atoms	time (h)
1%	10^6	3.44
0.1%	10^6	344
0.1%	10^7	34.4
0.1%	10^8	3.44

Our earliest francium MOTs had peak atom numbers on the order of 10^6. These numbers, along with improvements we have made to the trap since then, suggest that our desired 0.1% measurement is within reach. Quantifying and reducing systematic uncertainties will take much longer. However, we anticipate that much of that work can be done offline using rubidium.

5.5 Summary

The photoionization cross section of the $7P_{3/2}$ state of francium for 442 nm light has been measured to be 17.5 ± 4.6 Mb. We irradiated atoms in a magneto-optical trap and measured the change in trap lifetime to deduce the photoionization rate. The result is in line with the general trend exhibited by photoionization cross-sections for the other alkalis. This measurement was used to estimate the photoionization loss rate during a Stark-induced transition measurement and shows that modest 506 nm

laser light intensity still provides a good signal with which to make a precision APV measurement in a reasonable time.

Chapter 6

Conclusion and future steps

6.1 Summary

The Francium Trapping Facility (FTF) has come a long way in the past four years. We have progressed from bare concrete to a radioactive trapping facility where several species of francium have been trapped for the first time. Our capture MOT has repeatedly demonstrated trapped atom populations on the order of 10^6 atoms. We have demonstrated the transfer of atoms between the capture trap and a second MOT in our recently commissioned science chamber. The transfer efficiency demonstrated in rubidium has not yet been achieved in francium, but our first (and only) attempt at a francium transfer was successful. Overall, the required level of laboratory infrastructure is nearing completion and we can anticipate advancing towards the series of measurements culminating in an APV $7S - 8S$ forbidden transition measurement. Our next beamtime will see a test of a more robust neutralizer design. This design will reduce the likelihood of the neutralizer failing, as it did during our most recent

beamtime. Then we will optimize the francium transfer to the science chamber MOT.

The RF sideband technique which we utilized to measure isotope shifts was successful. Our published measurements of the D1 transition, along with D2 values obtained from literature, allowed us to generate a King plot to separate the mass and field shifts [6]. These two quantities are calculated very differently [64], and our results allow benchmarking of the methods employed by theorists. Improving our final isotope shift values would require an improvement in the stability of our laser frequency-lock or more precise ground state hyperfine splitting measurements. Such a measurement is in development by our collaborators working on the anapole moment experiment, and their microwave spectroscopy technique should produce results within the next few beamtimes. Our laser frequency-lock has been greatly improved since our first beamtime. Its stability is now approaching the limit of the polarization stabilized HeNe laser, and thus further improvements would involve a redesign of the system.

The photoionization cross-section measurement was sufficient to extract a value for our empirical estimate of the loss rate during an APV measurement. An improved photoionization measurement would require much greater care on a number of experimental details, such as more precisely measuring the ionizing laser power, saturating the cycling transition to maximize the excited state fraction, and reducing fluctuations in the trap for more reliable lifetime fitting. This last point we have already improved as our current traps are much more stable than those we achieved in our earliest beamtime, where the photoionization measurement occured.

6.2 Ongoing APV development

We have reached a point where the development of the electric field plates for the $7S - 8S$ Stark-interference has become a priority in the near term. The metal plates, in the science chamber at the time of writing, are ready for a Stark measurement in rubidium in preparation for a similar measurement in francium. Whether this is a static Stark shift or transition polarizability measurement of the $5S - 6S$ transition in rubidium remains to be determined. The transparent field plates are on hand and can be easily switched with the metal plates once required.

The frequency-doubled Ti:sapphire laser that will be used for the forbidden transition spectroscopy can excite a two-photon transition with its fundamental output. This means that there is a potentially stronger signal available to locate the $7S - 8S$ transition. We only know the energy of the $8S_{1/2}$ state in ^{210}Fr with respect to the $7P$ states to wavemeter accuracy [107]. The transition must be located in our laboratory and possibly in a different isotope, with an unknown isotope shift; this is a goal for an upcoming beamtime. Once the transition is directly observed, measurements of the transition in an applied electric field can occur.

In the farther term, there exists a series of increasingly difficult measurements of the Stark-interference terms in equation 1.3. The largest of these terms is proportional to the scalar transition polarizability squared. Once that is observed, the search for the interference with the M1 amplitude or a measurement of the vector transition polarizability will be attempted before the ultimate measurement of the APV term. For these interference terms to be observed, there remain a number of technical developments required in our laboratory, e.g. the means for a fast, exact

and reproducible reversal of the electric field. These high precision measurements are in the future for a following student.

Appendix A

Isotope shift data

This appendix shows all of the data used for the D1 isotope shift measurements. The red lines are the fit result for each displayed transition peak.

Our first experimental beamtime used a pair of AD4350 synthesizer cards to produce the RF used to generate sidebands on our probe laser, whose 817 nm wavelength was held constant by the laser control program, and the RF was swept to scan the transitions of the target isotope and the reference isotope ^{209}Fr. Figures A.1-A.4 show data collected during this beamtime. AD4350 cards are limited in their range of frequencies, requiring careful selection of probe laser frequency so that a transition could be reached by the RF in both the target isotope and the reference. In some cases, the second harmonic sideband was required to span the frequency difference. Thus, each measurement has two sets of data; one is for the target isotope and the other is for the reference. Figure A.1 shows an example of the unprocessed data collected by our MCS. The scan clearly shows the separation between photons collected when the trap light is on compared to when the trap light is off, and the AC Stark shift is

obvious.

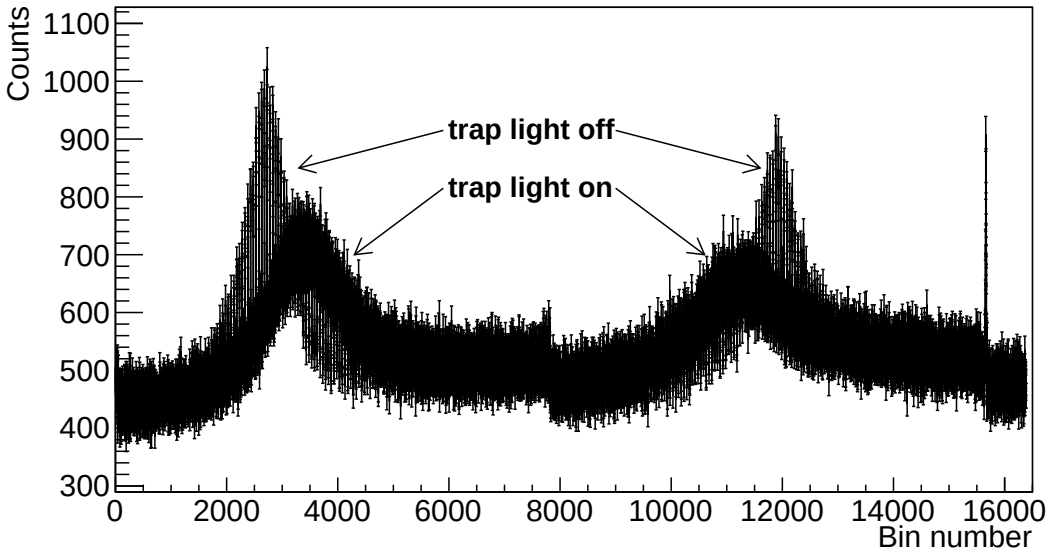

Figure A.1: Raw data of the $F = 7/2 \rightarrow F' = 5/2, 7/2$ transition in ^{206}Fr using the AD4350 synthesizers. The alternating signal is due to chopping of the trap light and the AC Stark shift is visible in the displacement of the peaks between trap light-on and trap light-off.

We analyze by selecting the trap light-off data and fitting Lorentzian functions to each peak. This is done for both the target isotope, where each sideband is scanned over a peak giving us the hyperfine splitting, and the reference isotope, where only one peak is observed, see, e.g., figure A.2.

The second experimental beamtime used the Phasematrix digital synthesizer as the frequency generator for the fiber modulator. Figures A.5-A.18 show data from this second beamtime. This synthesizer enabled us to reach transitions in all of our isotopes without having to adjust the laser frequency. Thus, the data were collected for each transition individually, rather than in pairs as in the previous beamtime.

Some of these data, e.g. that shown in figure A.5, show spikes that are possibly

due to the behaviour of the Phasematrix as it changes frequencies. The MCS bin width and the Phasematrix dwell time are not synchronized. This means that there will be bins during which the frequency is changed. Also, the synthesizer requires some time to settle after its discrete frequency steps. Thus, as the MCS continues to record data during these steps, we observe sometimes large fluctuations at the edges of each frequency window.

The discrete nature of the Phasematrix scan means that some data processing is required before the fitting can be done. We neglect the anomalous data points by comparing them to adjacent points, keeping only those that are within an error bar. Then the remaining points in each frequency step are averaged, producing an average counts per bin at that frequency. The processed data are then fit to a Lorentzian and the obtained centroid is used to calculate the isotope shift. The process is not perfect, especially in cases where low counts cause a poorer Lorentzian fit. However, it does provide reliable fits to determine the centroid and the accumulated errors, such as peak asymmetry, backgrounds, etc., are well below the other systematic errors present in our isotope shift measurements.

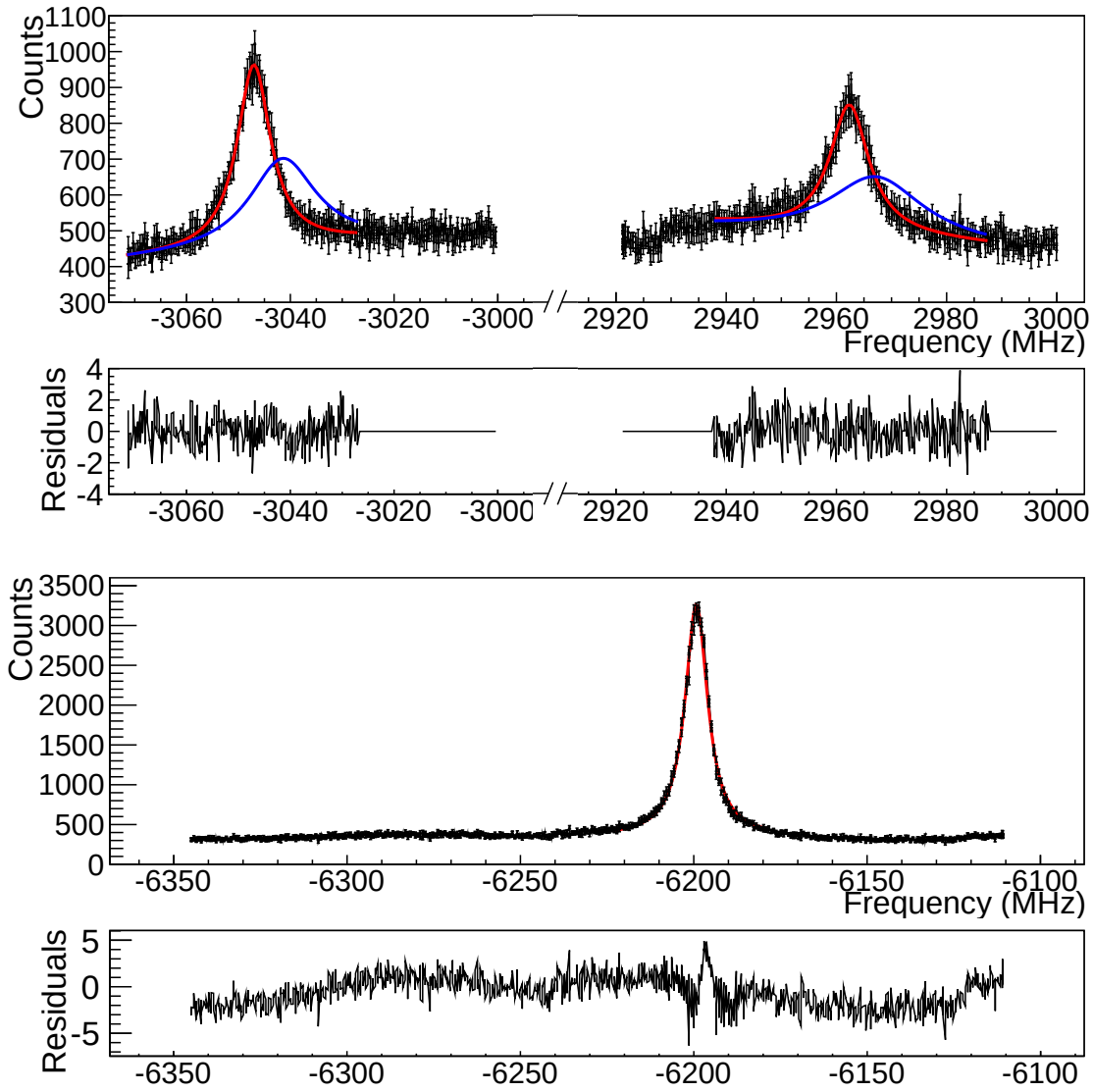

Figure A.2: (Top) Data of the $F = 7/2 \rightarrow F' = 5/2, 7/2$ transition in ^{206}Fr using the AD4350 synthesizer. Red Lorentzian fits are used to calculate the hyperfine splitting and the isotope shift. The blue lines are fits with the trap light-on (data not shown), displaying the AC Stark shift. (Bottom) Data of the reference isotope ^{209}Fr $F = 5 \rightarrow F' = 5$ transition. The fit (red line) is Lorentzian with the center value used to calculate the isotope shift.

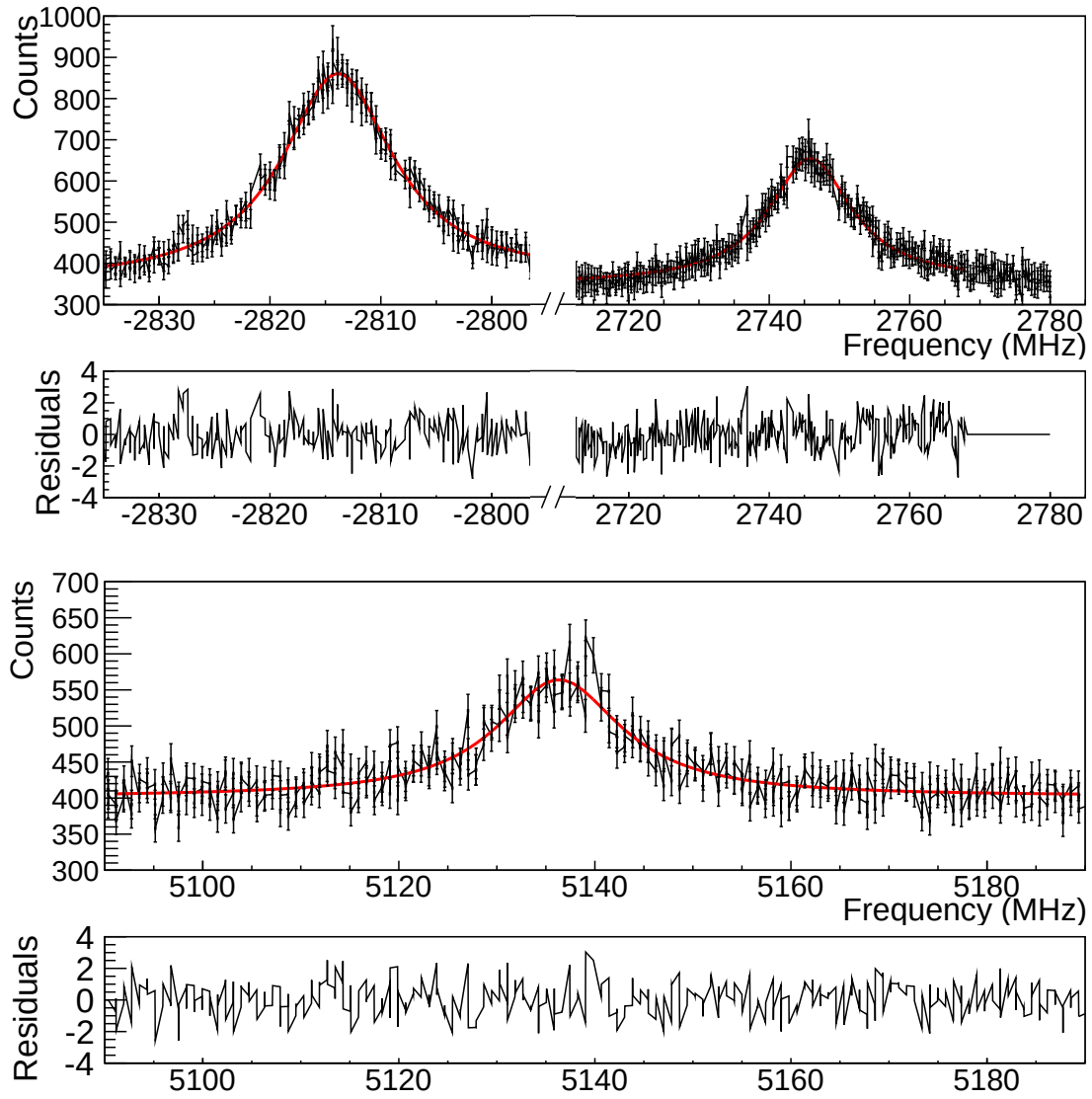

Figure A.3: (Top) Data of the $F = 5 \rightarrow F' = 4, 5$ transition in ^{207}Fr using the AD4350 synthesizer. The red Lorentzian fits are used to calculate the hyperfine splitting and the isotope shift. (Bottom) Data of the reference isotope ^{209}Fr $F = 5 \rightarrow F' = 5$ transition. The fit (red line) is Lorentzian with the center value used to calculate the isotope shift.

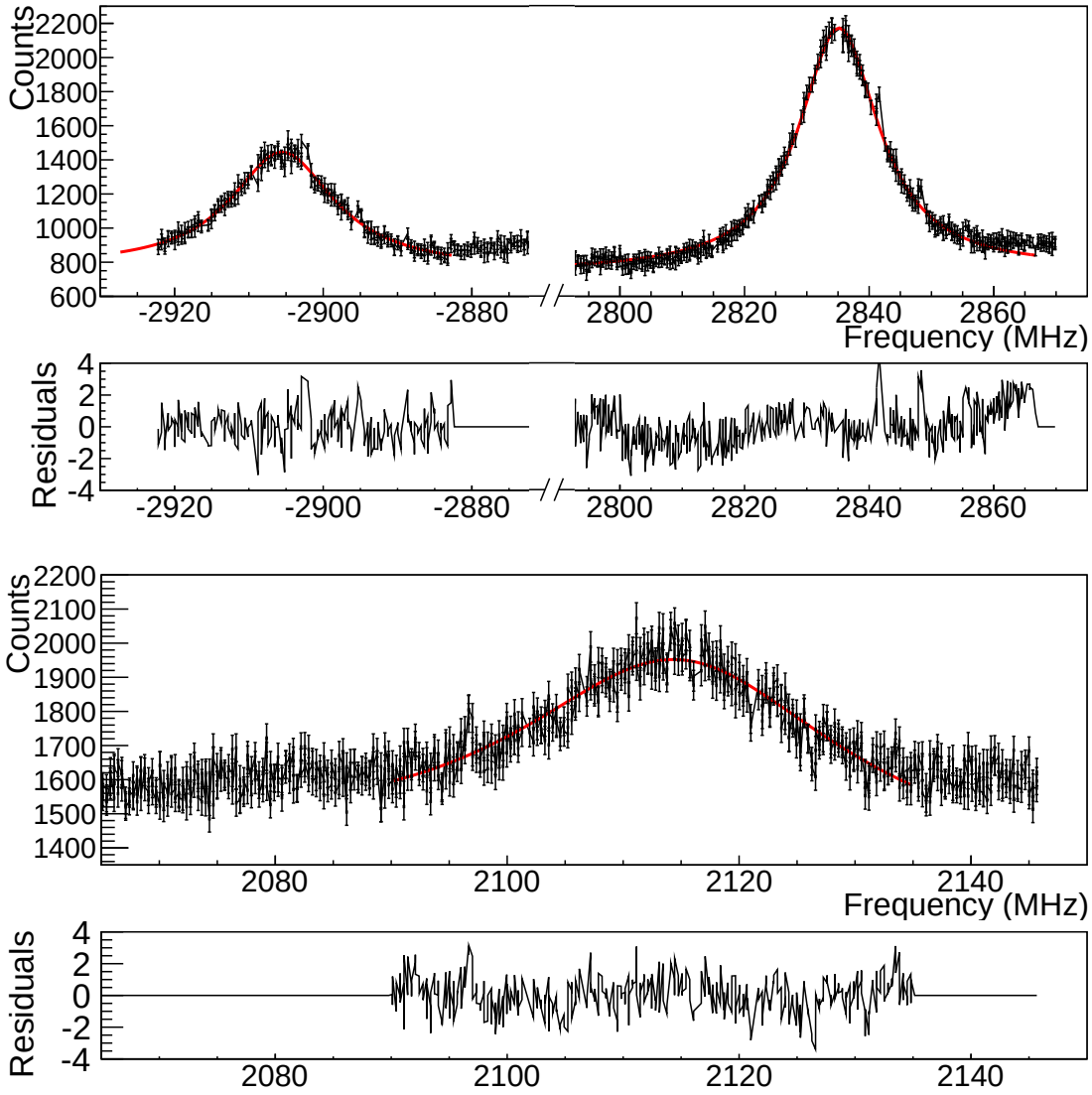

Figure A.4: (Top) Data of the $F = 5 \rightarrow F' = 4, 5$ transition in ^{213}Fr using the AD4350 synthesizer. The red Lorentzian fits are used to calculate the hyperfine splitting and the isotope shift. (Bottom) Data of the reference isotope ^{209}Fr $F = 5 \rightarrow F' = 5$ transition. The fit (red line) is Lorentzian with the center value used to calculate the isotope shift.

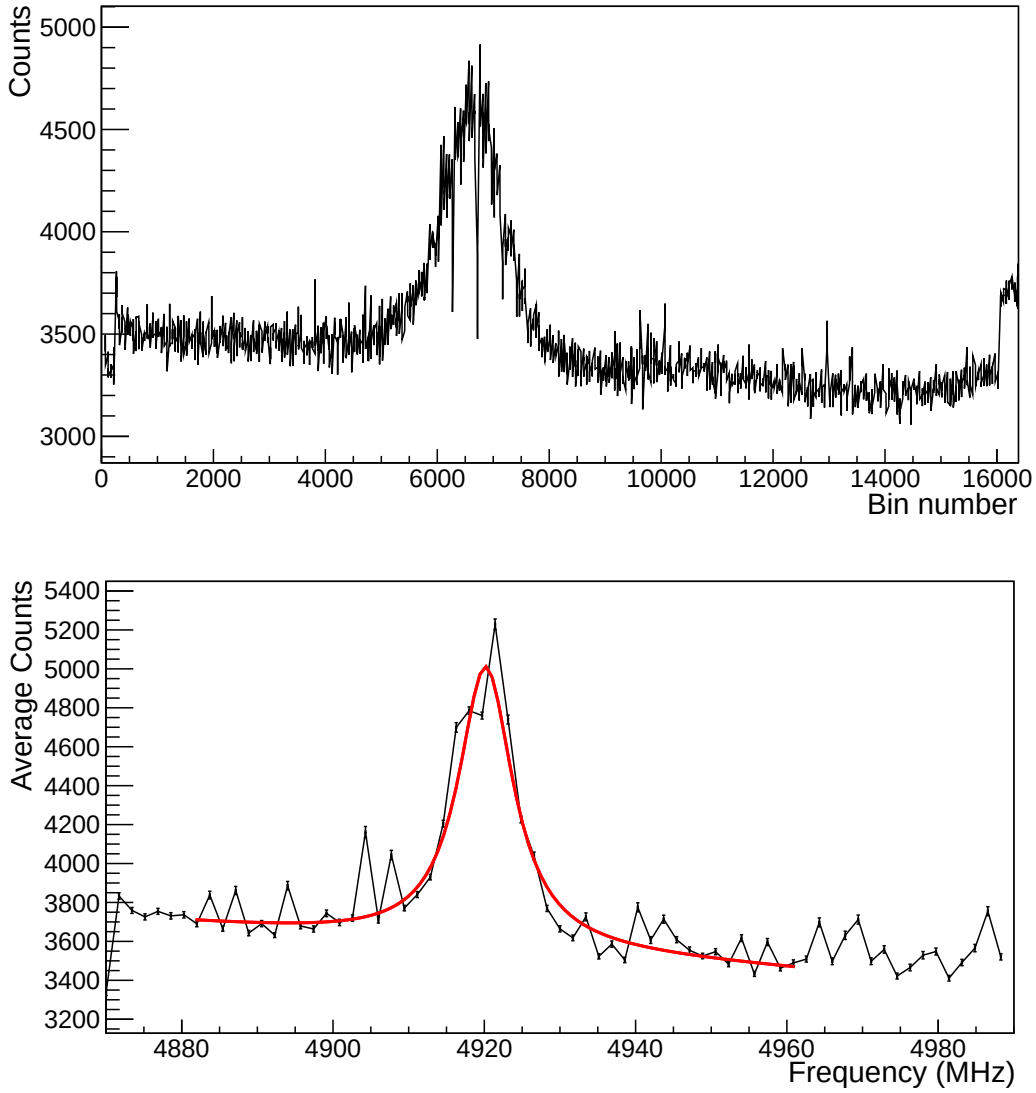

Figure A.5: (Top) Raw data of the $F = 15/2 \rightarrow F' = 15/2$ transition in ^{206m}Fr using the Phasematrix QuickSyn digital synthesizer. The spikes are likely due to the lack of synchronization between the synthesizer dwell time and bin width. (Bottom) Processed data with a calibrated frequency axis. The fit (red line) is Lorentzian with the center value used to calculate the isotope shift.

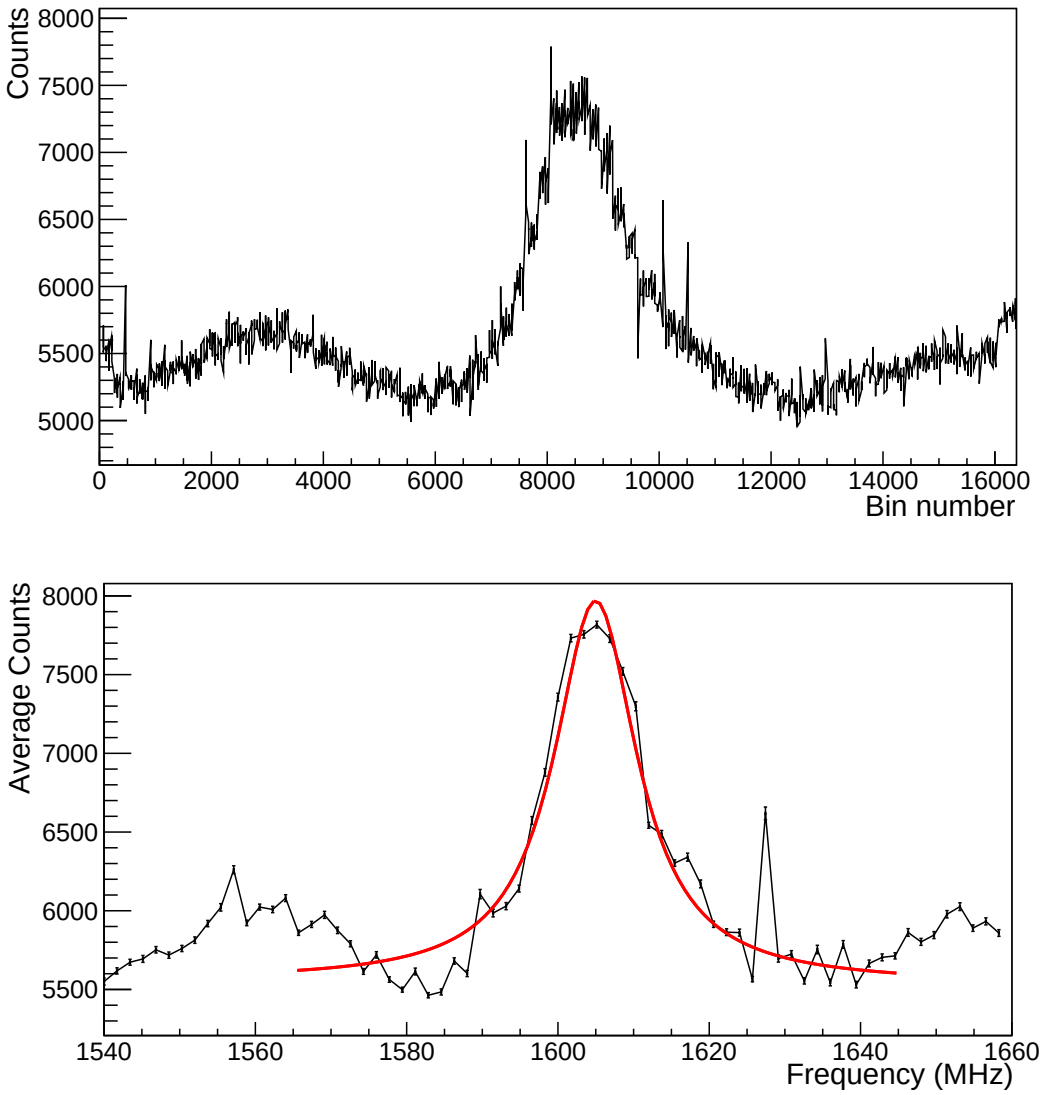

Figure A.6: (Top) Raw data of the $F = 15/2 \rightarrow F' = 13/2$ transition in ^{206m}Fr using the Phasematrix QuickSyn digital synthesizer. (Bottom) Processed data with a calibrated frequency axis. The fit (red line) is Lorentzian with the center value used to calculate the isotope shift.

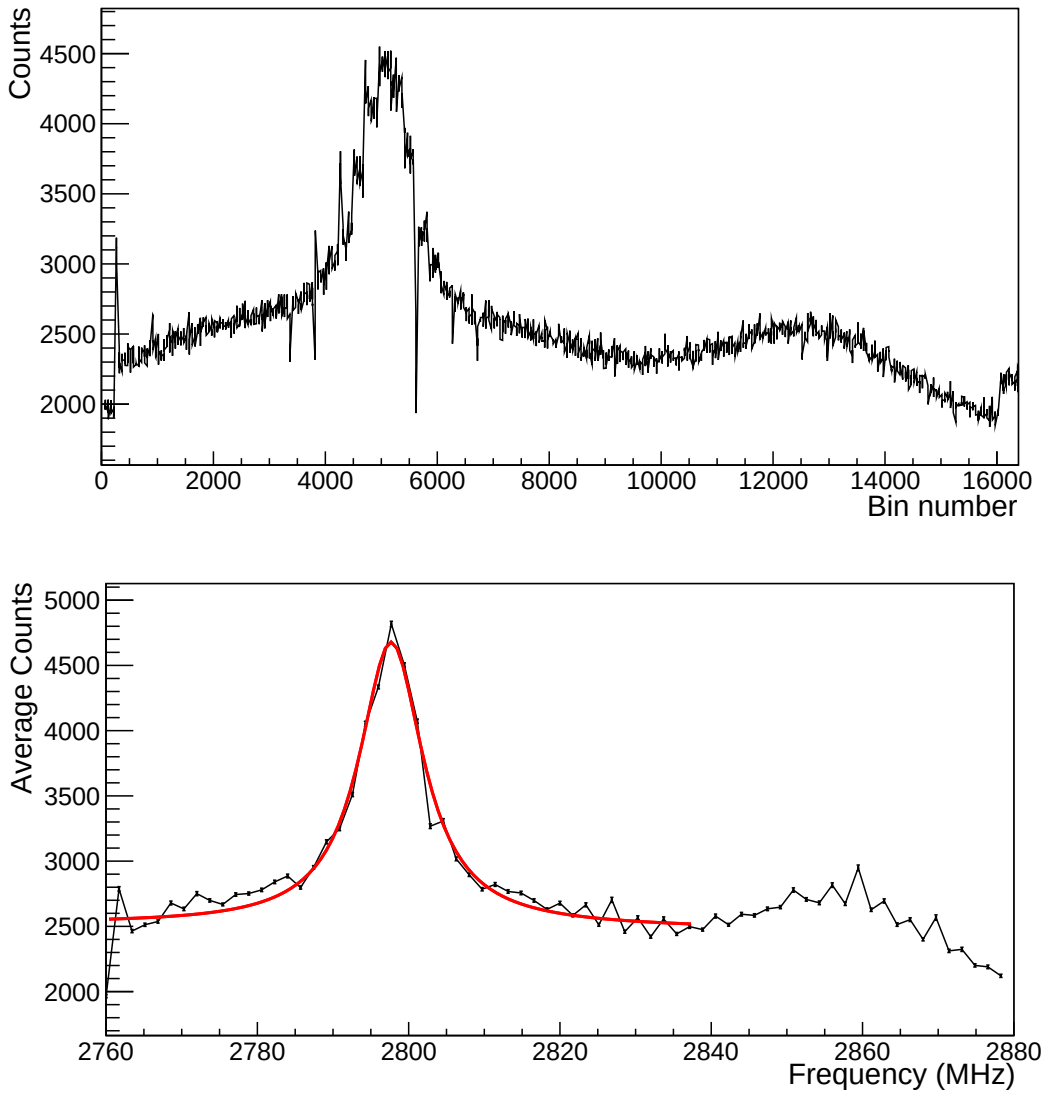

Figure A.7: (Top) Raw data of the $F = 15/2 \rightarrow F' = 15/2$ transition in ^{208}Fr using the Phasematrix QuickSyn digital synthesizer. (Bottom) Processed data with a calibrated frequency axis. The fit (red line) is Lorentzian with the center value used to calculate the isotope shift.

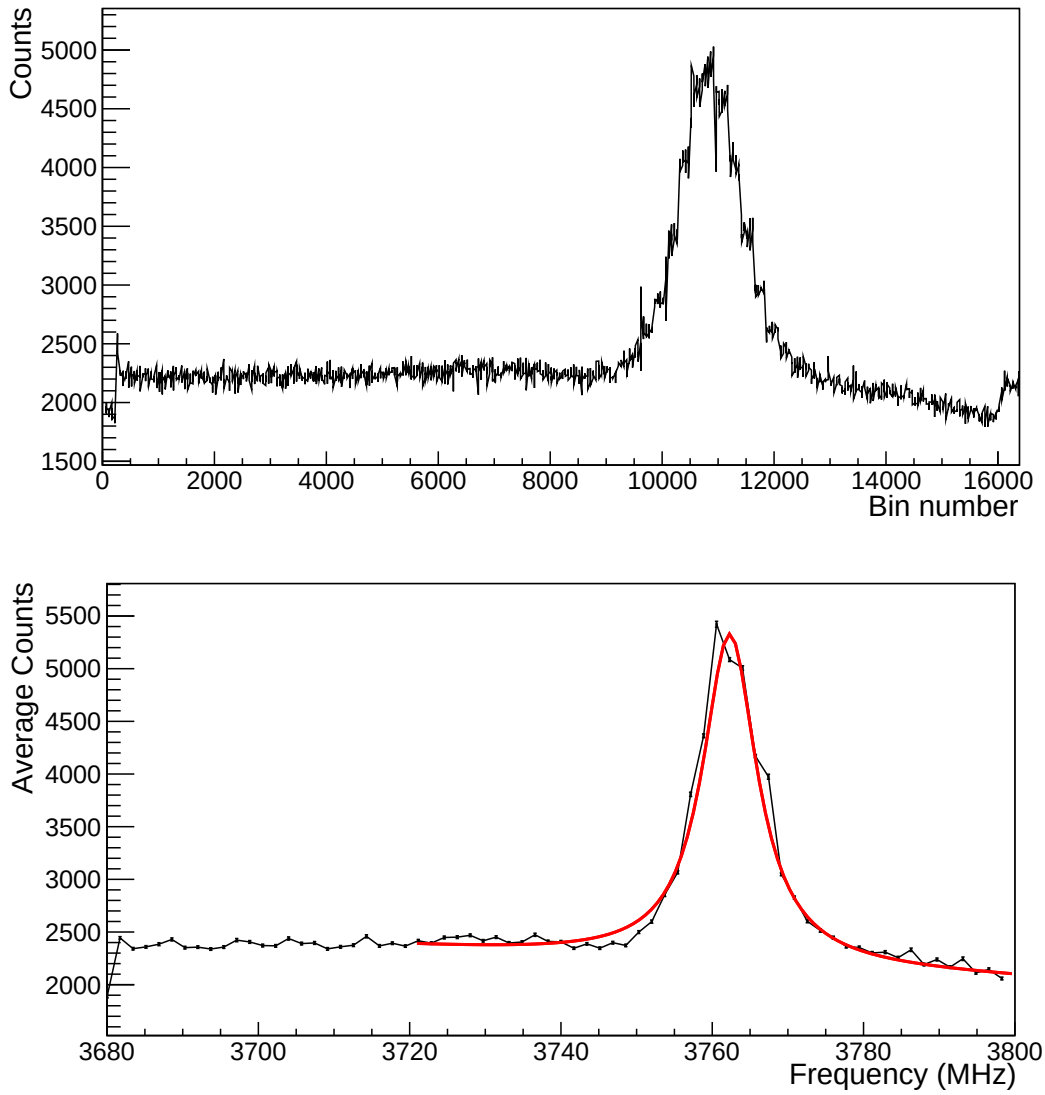

Figure A.8: (Top) Raw data of the $F = 15/2 \rightarrow F' = 13/2$ transition in ^{208}Fr using the Phasematrix QuickSyn digital synthesizer. (Bottom) Processed data with a calibrated frequency axis. The fit (red line) is Lorentzian with the center value used to calculate the isotope shift.

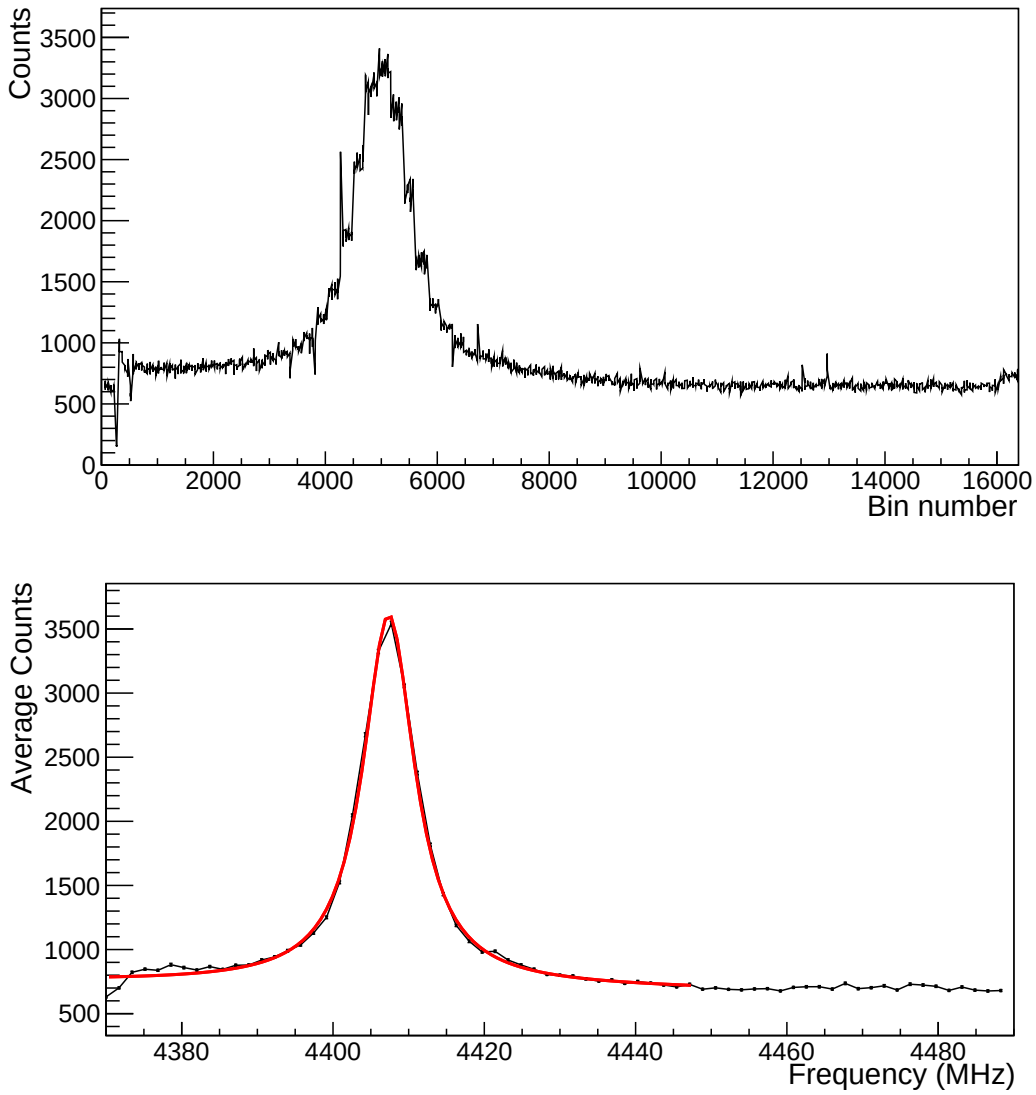

Figure A.9: (Top) Raw data of the $F = 5 \rightarrow F' = 5$ transition in ^{209}Fr using the Phasematrix QuickSyn digital synthesizer. (Bottom) Processed data with a calibrated frequency axis. The fit (red line) is Lorentzian with the center value used to calculate the isotope shift.

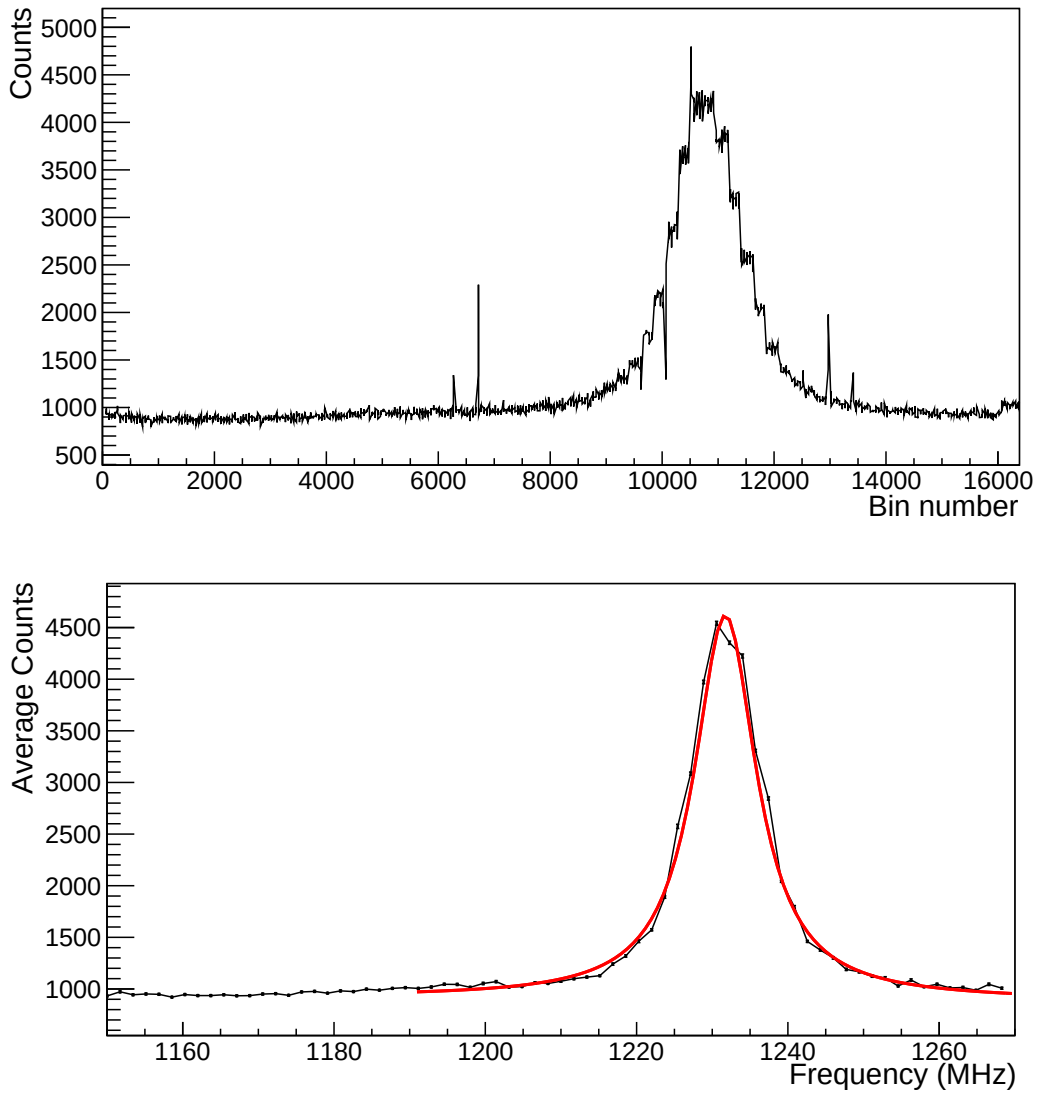

Figure A.10: (Top) Raw data of the $F = 5 \rightarrow F' = 4$ transition in ^{209}Fr using the Phasematrix QuickSyn digital synthesizer. (Bottom) Processed data with a calibrated frequency axis. The fit (red line) is Lorentzian with the center value used to calculate the isotope shift.

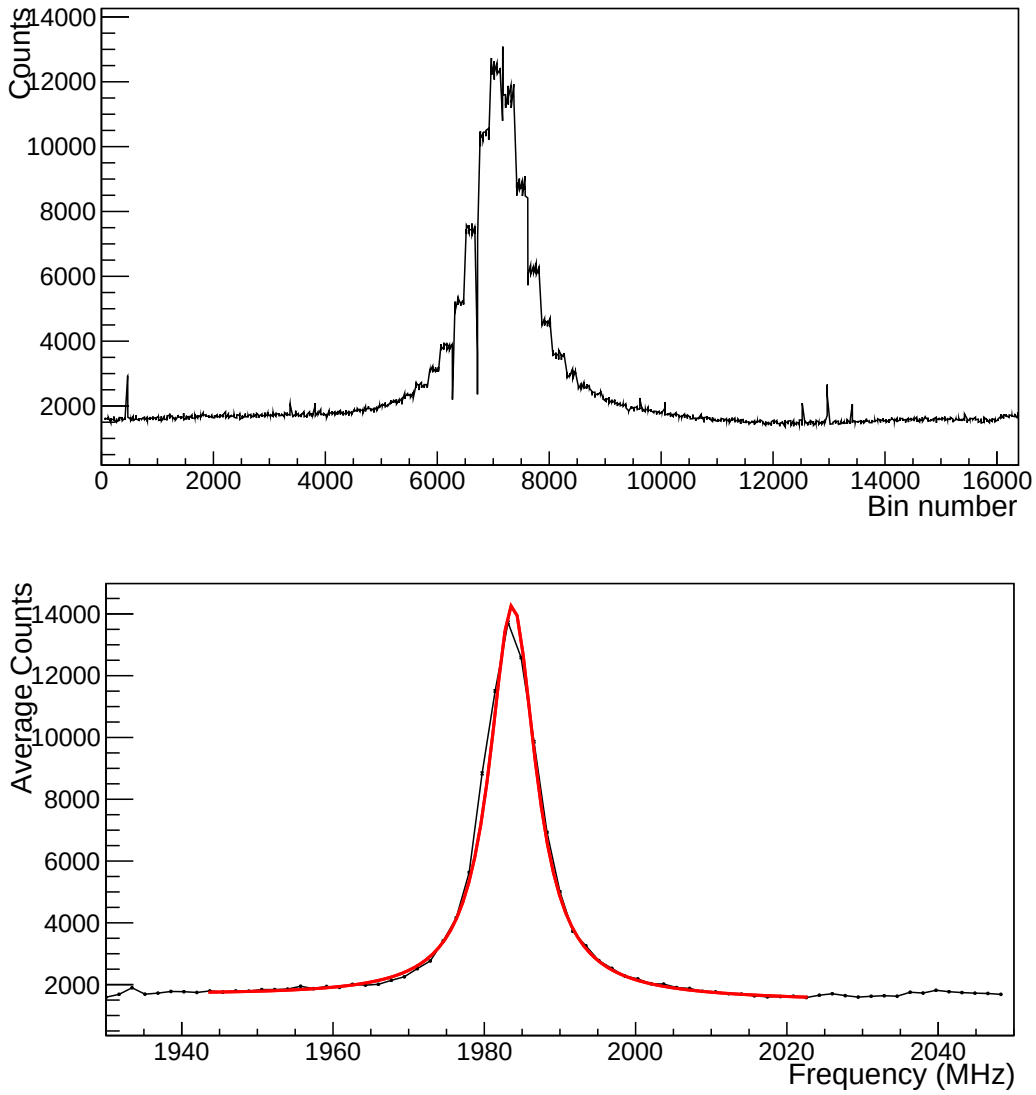

Figure A.11: (Top) Raw data of the $F = 13/2 \rightarrow F' = 13/2$ transition in ^{210}Fr using the Phasematrix QuickSyn digital synthesizer. (Bottom) Processed data with a calibrated frequency axis. The fit (red line) is Lorentzian with the center value used to calculate the isotope shift.

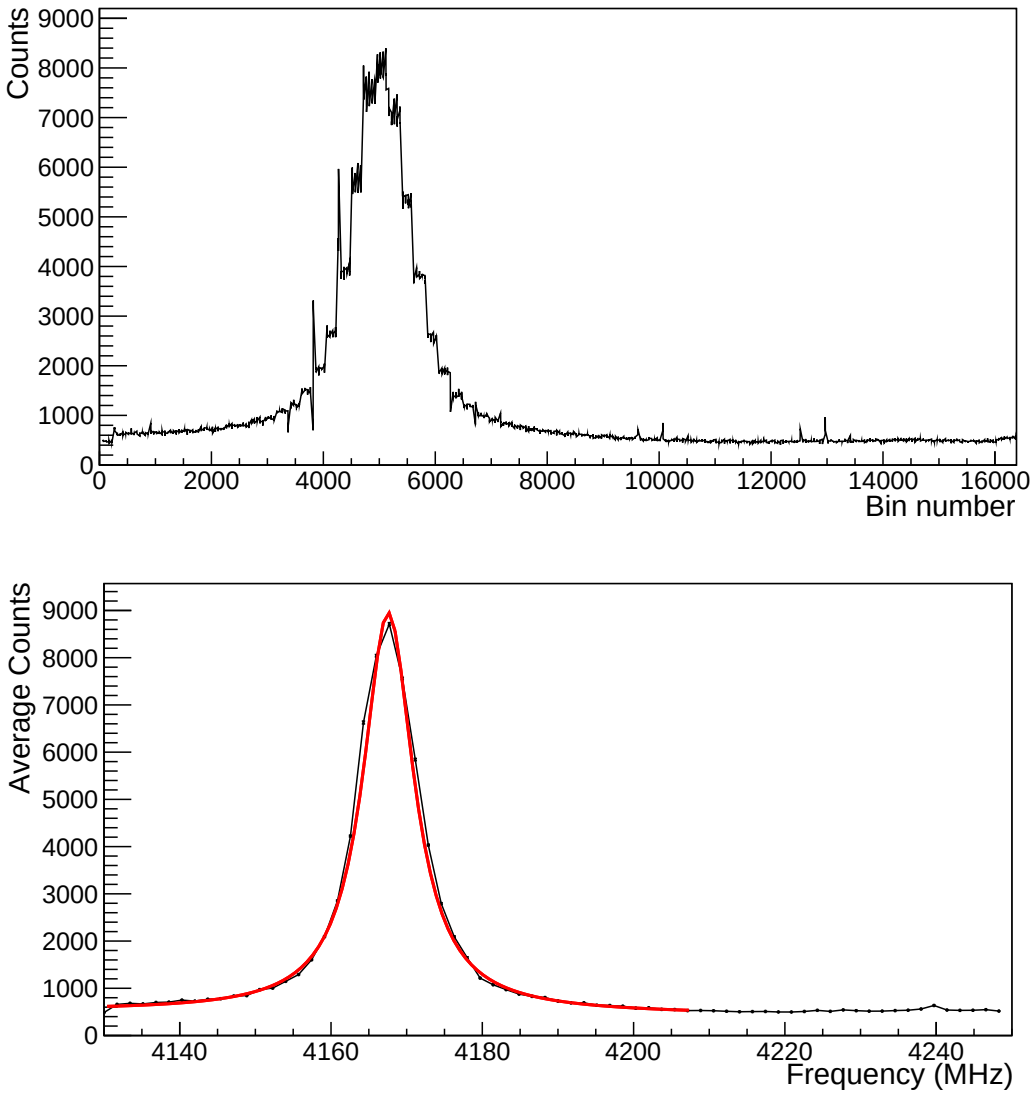

Figure A.12: (Top) Raw data of the $F = 13/2 \rightarrow F' = 11/2$ transition in ^{210}Fr using the Phasematrix QuickSyn digital synthesizer. (Bottom) Processed data with a calibrated frequency axis. The fit (red line) is Lorentzian with the center value used to calculate the isotope shift.

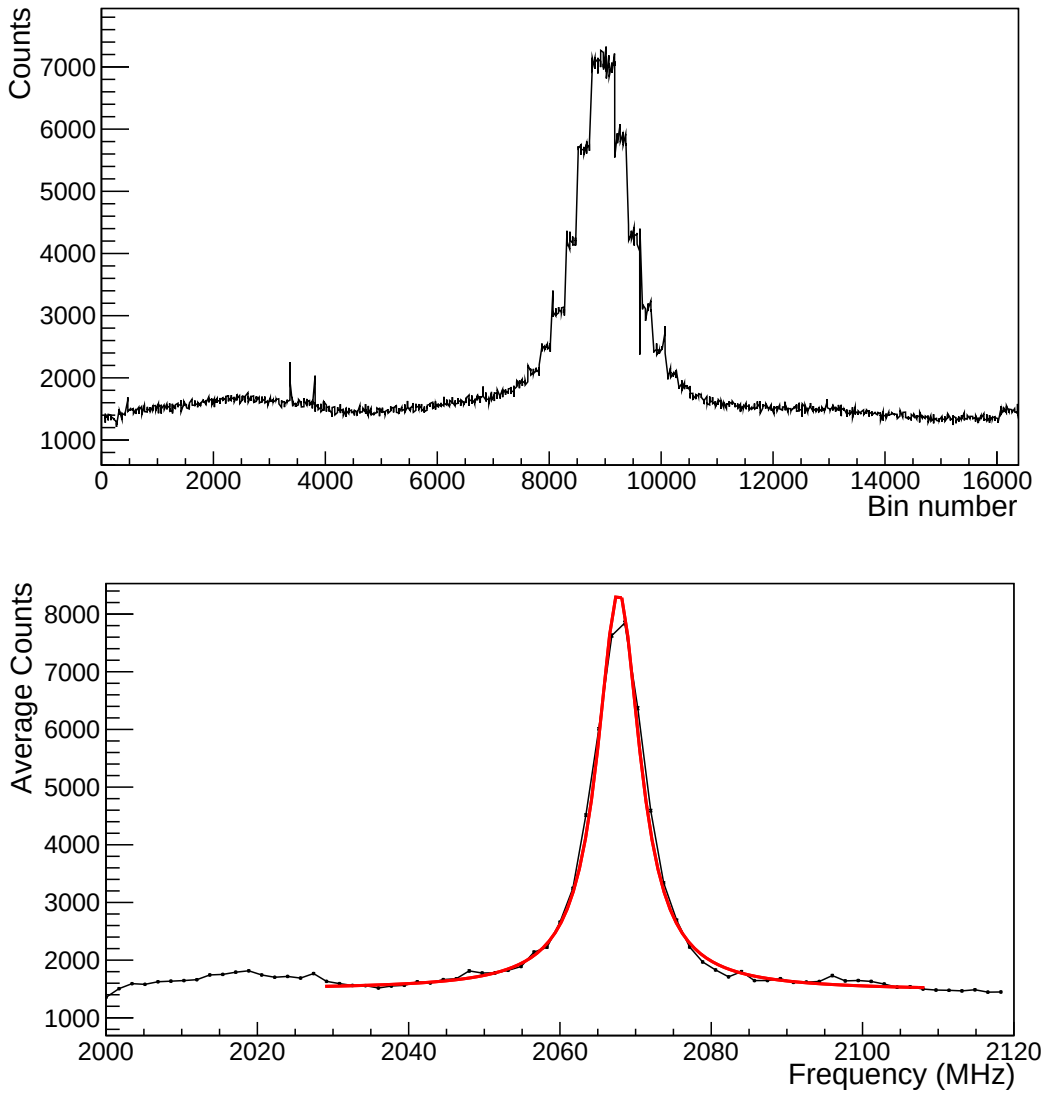

Figure A.13: (Top) Raw data of the $F = 5 \rightarrow F' = 5$ transition in ^{211}Fr using the Phasematrix QuickSyn digital synthesizer. (Bottom) Processed data with a calibrated frequency axis. The fit (red line) is Lorentzian with the center value used to calculate the isotope shift.

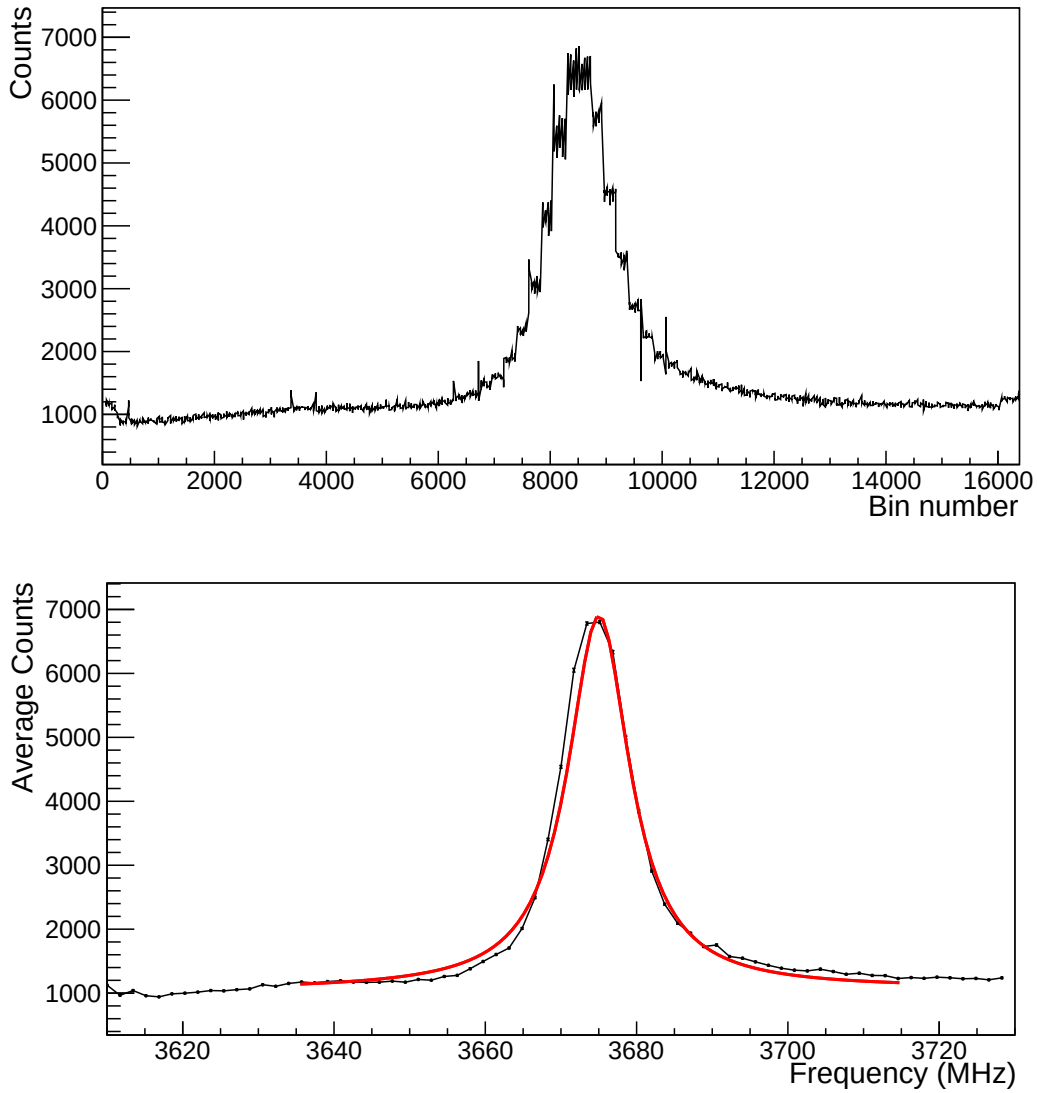

Figure A.14: (Top) Raw data of the $F = 5 \rightarrow F' = 4$ transition in ^{211}Fr using the Phasematrix QuickSyn digital synthesizer. (Bottom) Processed data with a calibrated frequency axis. The fit (red line) is Lorentzian with the center value used to calculate the isotope shift. There was a recording error which caused a suspected 30 MHz error on this frequency axis. Thus this particular transition was not used for further analysis.

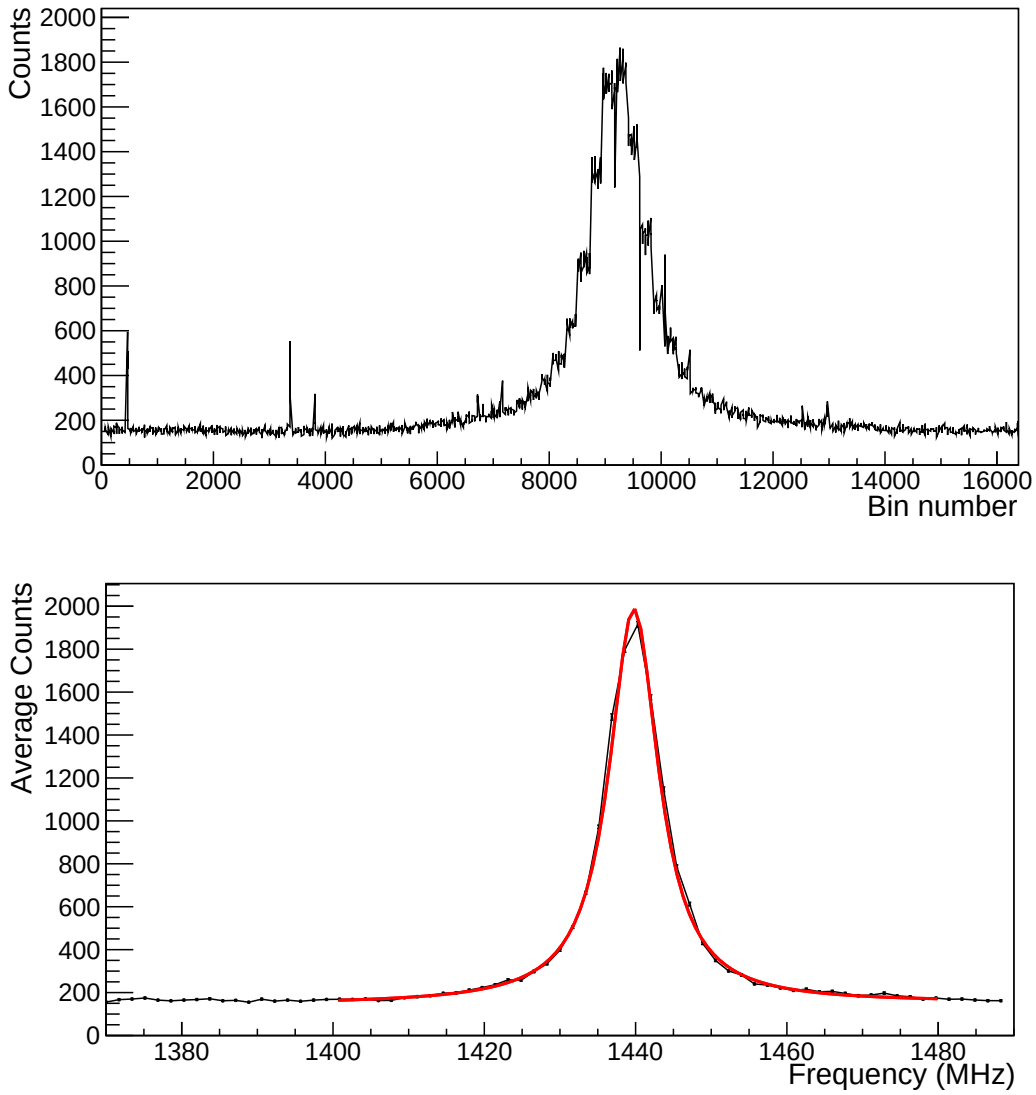

Figure A.15: (Top) Raw data of the $F = 11/2 \rightarrow F' = 11/2$ transition in ^{212}Fr using the Phasematrix QuickSyn digital synthesizer. (Bottom) Processed data with a calibrated frequency axis. The fit (red line) is Lorentzian with the center value used to calculate the isotope shift.

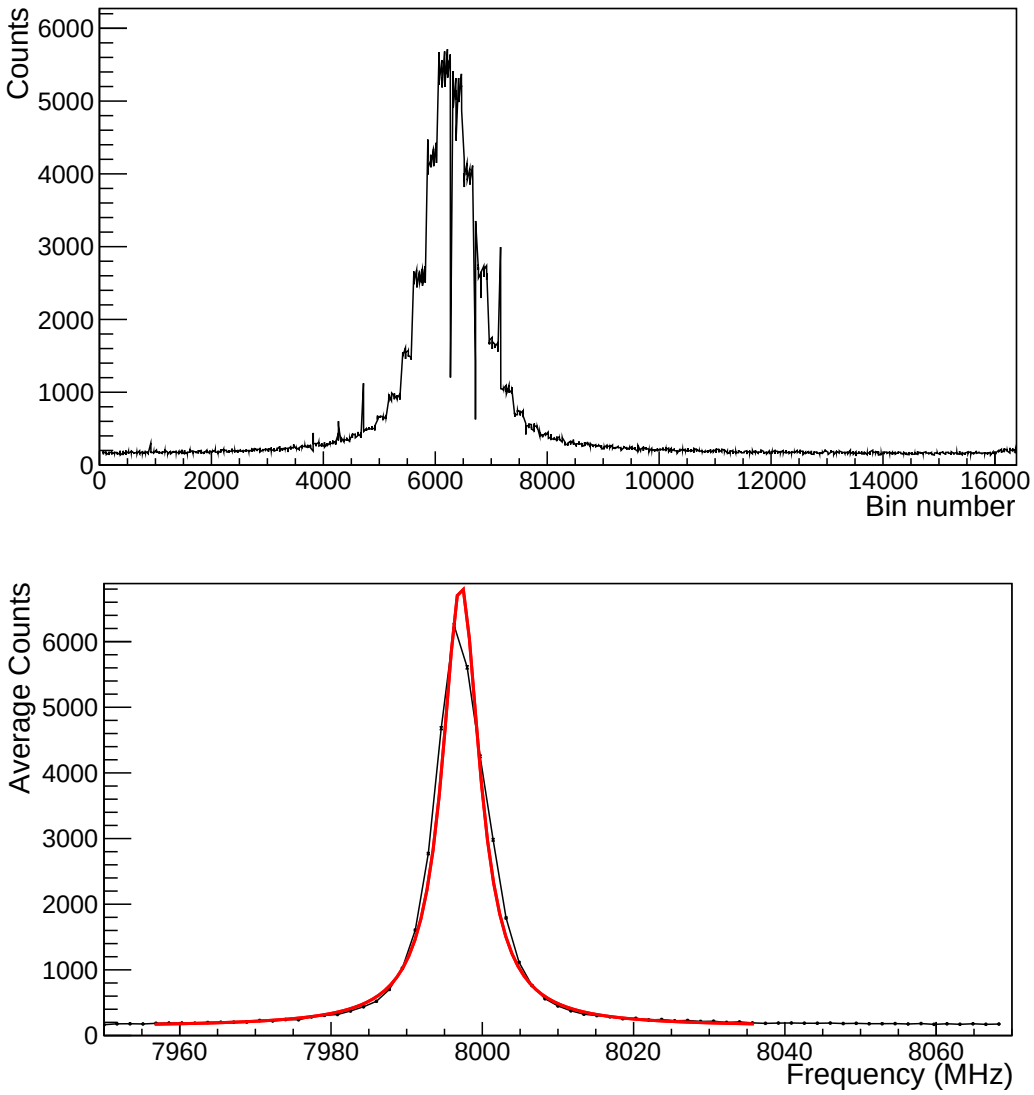

Figure A.16: (Top) Raw data of the $F = 11/2 \rightarrow F' = 9/2$ transition in ^{212}Fr using the Phasematrix QuickSyn digital synthesizer. (Bottom) Processed data with a calibrated frequency axis. The fit (red line) is Lorentzian with the center value used to calculate the isotope shift.

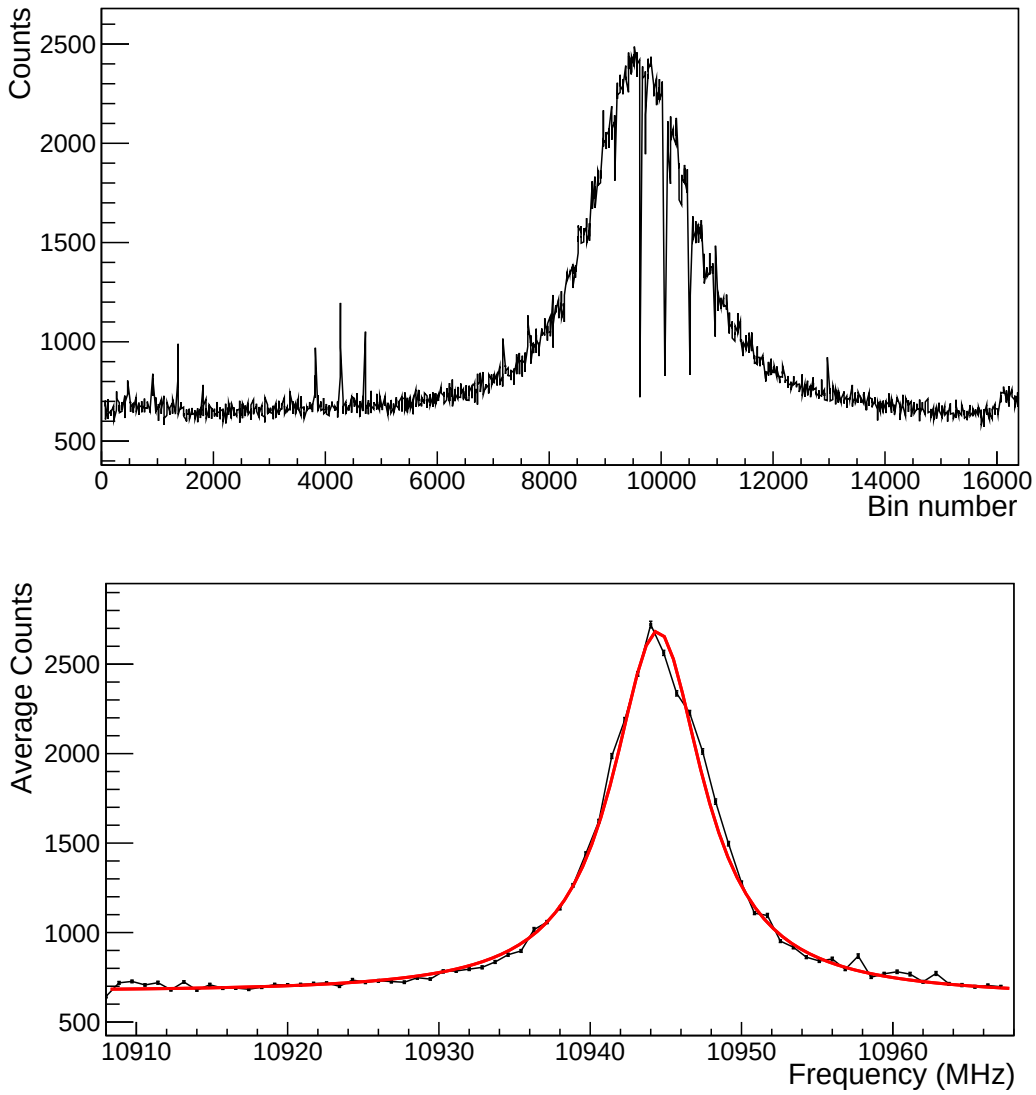

Figure A.17: (Top) Raw data of the $F = 3 \rightarrow F' = 3$ transition in ^{221}Fr using the Phasematrix QuickSyn digital synthesizer. (Bottom) Processed data with a calibrated frequency axis. The fit (red line) is Lorentzian with the center value used to calculate the isotope shift.

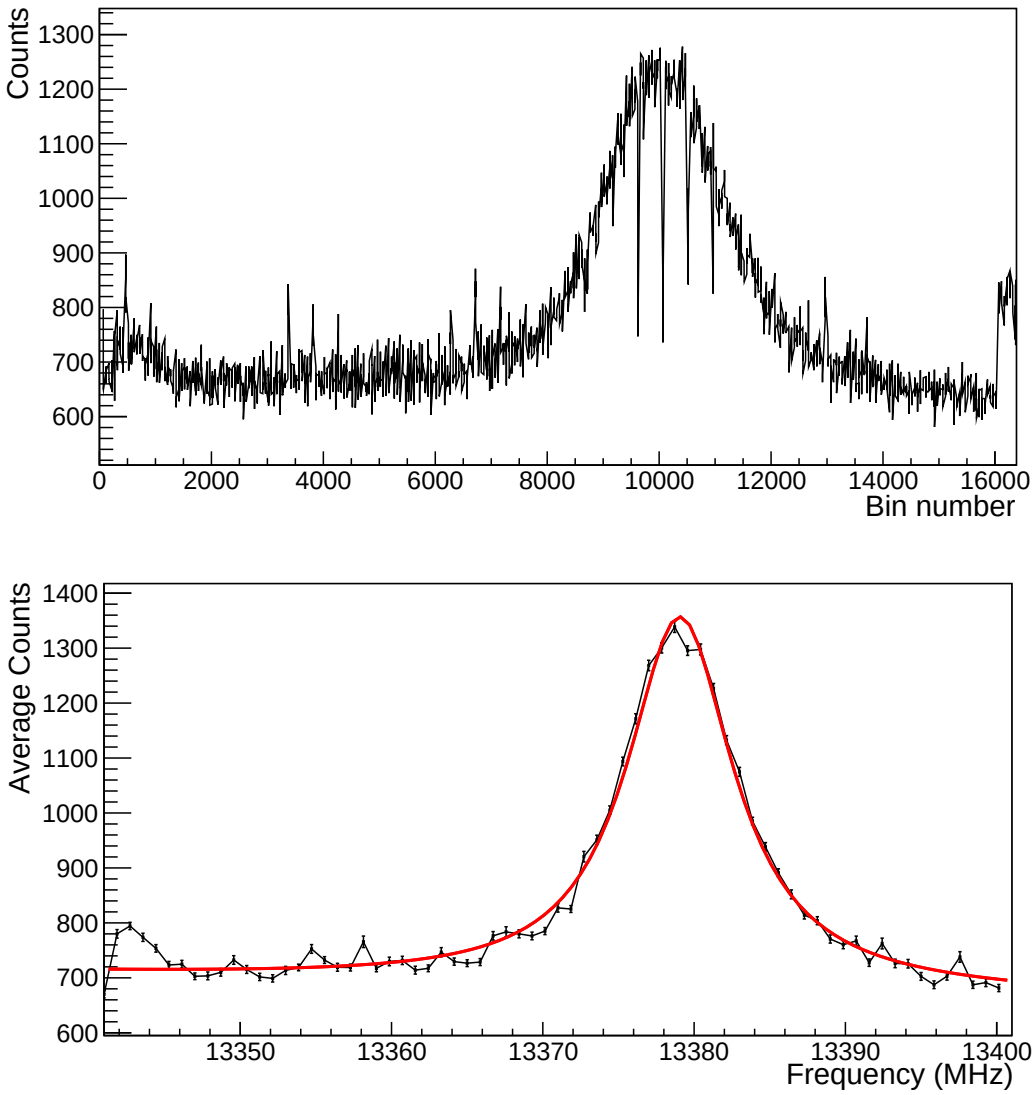

Figure A.18: (Top) Raw data of the $F = 3 \rightarrow F' = 2$ transition in ^{221}Fr using the Phasematrix QuickSyn digital synthesizer. (Bottom) Processed data with a calibrated frequency axis. The fit (red line) is Lorentzian with the center value used to calculate the isotope shift.

Appendix B

Rate equations

This appendix contains the full rate equations used for the calculation of the excited state fraction involved in the determination of the photoioinization cross-section in chapter 5.

The selection rules for electric dipole transitions are $\Delta F = 0, \pm 1$, and they dictate which states are coupled. Figure 5.3 shows the states populated during trapping and labels them for the following rate equation.

Couplings between states are denoted by A_{ij} for spontaneous emissions and $W_{ij} = W_{ji}$ for stimulated emission/absorption. $\dot{N}_i$ denotes the time derivative of the population of the state, and is by definition zero in the steady-state. The magnitudes of

the couplings will be introduced later but for now will remain completely general.

$$\dot{N_e} = W_{eb}(N_b - N_e) - A_{eb}N_e \tag{B.1}$$

$$\dot{N_d} = W_{db}(N_b - N_d) - (A_{db} + A_{da})N_d \tag{B.2}$$

$$\dot{N_c} = W_{ca}(N_a - N_c) - (A_{cb} + A_{ca})N_c \tag{B.3}$$

$$\dot{N_b} = W_{eb}(N_e - N_b) + W_{db}(N_d - N_b) + A_{eb}N_e + A_{db}N_d + A_{cb}N_c \tag{B.4}$$

$$\dot{N_a} = W_{ca}(N_c - N_a) + A_{da}N_d + A_{ca}N_c \tag{B.5}$$

Once the trap reaches a steady state, the time derivatives are zero and we can solve for ratios of the state populations. Beginning with equations (B.1),(B.2),(B.3), respectively, for the excited states:

$$N_b = \left(\frac{W_{eb} + A_{eb}}{W_{eb}}\right) N_e = C_{eb}N_e \tag{B.6}$$

$$N_b = \left(\frac{W_{db} + A_{db} + A_{da}}{W_{db}}\right) N_d = C_{db}N_d \tag{B.7}$$

$$N_a = \left(\frac{W_{ca} + A_{cb} + A_{ca}}{W_{ca}}\right) N_c = C_{ca}N_c. \tag{B.8}$$

Now, using the lower hyperfine ground state equation (B.5) and substituting in (B.8):

$$\begin{aligned} 0 &= W_{ca}N_c - W_{ca}\left(\frac{W_{ca} + A_{cb} + A_{ca}}{W_{ca}}\right) N_c + A_{da}N_d + A_{ca})N_c \\ &= -A_{cb}N_c + A_{da}N_d \\ N_c &= \frac{A_{da}}{A_{cb}}N_d = C_{dc}N_d. \end{aligned} \tag{B.9}$$

The fraction of atoms in each excited state is determined by combinations of the above ratios. We start with calculating N_e/N, where $N = N_a + N_b + N_c + N_d + N_e$.

$$\begin{aligned}\frac{N}{N_e} &= \frac{N_a}{N_e} + \frac{N_b}{N_e} + \frac{N_c}{N_e} + \frac{N_d}{N_e} + \frac{N_e}{N_e} \\ &= \frac{N_a}{N_c}\frac{N_c}{N_d}\frac{N_d}{N_b}\frac{N_b}{N_e} + \frac{N_b}{N_e} + \frac{N_c}{N_d}\frac{N_d}{N_b}\frac{N_b}{N_e} + \frac{N_d}{N_b}\frac{N_b}{N_e} + 1 \\ &= \frac{C_{ca}C_{dc}C_{eb}}{C_{db}} + C_{eb} + \frac{C_{dc}C_{eb}}{C_{db}} + \frac{C_{eb}}{C_{db}} + 1 \end{aligned} \tag{B.10}$$

Taking the reciprocal of (B.10) gives the excited state fraction of the $F' = 4$ $7P_{3/2}$ state. Once this is done for each of the photoionizable states, those results are summed to give the total excited state fraction $n_{excited} = (N_c + N_d + N_e)/N$.

Now, the couplings W_{ij} and A_{ij} must be determined in order to evaluate $n_{excited}$. The A_{ij} are Einstein spontaneous emission coefficients, related to the lifetime of the excited states, split according to angular momentum coupling if there is more than one possible ground state for the decay. Thus:

$$\begin{aligned} A_{eb} &= \frac{1}{\tau_{D2}} \\ A_{db} &= \frac{1}{\tau_{D2}}\left(\frac{4900}{4900+3920}\right) \\ A_{da} &= \frac{1}{\tau_{D2}}\left(\frac{3920}{4900+3920}\right) \\ A_{cb} &= \frac{1}{\tau_{D1}}\left(\frac{28}{28+35}\right) \\ A_{ca} &= \frac{1}{\tau_{D1}}\left(\frac{35}{28+35}\right), \end{aligned} \tag{B.11}$$

where τ_k denotes the lifetime of the excited state of the transition and the terms in brackets are the sums over m_F states of the normalized transition strengths between hyperfine levels of the D1 and D2 transitions in alkali atoms. They are determined by angular momentum couplings and are caculated in Appendix D of [73]; here we use

the values for an $I = 5/2$ atom and the polarization of the laser light is unimportant in the total factor since we sum over all m_F states.

The stimulated rates W_{ij} are calculated using saturation intensities (I_s), lifetimes (τ), wavelengths (λ), laser detunings (Δ) and intensities (I) according to equation (2.21) from [73]. Note that the natural linewidth of a transition ($\gamma_{ij} = 1/A_{ij}$) includes the ratios from equation B.11, determined by angular momentum couplings. The stimulated rates are:

$$W_{ij} = \frac{s_{ij}\gamma_{ij}/2}{1 + s_{ij} + (2\Delta_{ij}/\gamma_{ij})^2}, \tag{B.12}$$

where s_{ij} is the saturation parameter for each transition, given by:

$$s_{ij} = I/I_s \tag{B.13}$$

with the transition-dependent saturation intensity being:

$$I_s = \frac{\pi hc}{3\lambda\tau_{ij}}. \tag{B.14}$$

Each transition is treated as a separate two-level system for the rate calculation; this point is important for the properties of the transitions for which, e.g., the full state lifetime τ_k is split between the two ground states τ_{ij}. All of these parameter values are summarized in table B.1.

Using equation B.12, these parameters produce $W_{eb} = 1.02 \pm 0.30 \times 10^7$ Hz, $W_{db} = 4.0 \pm 2.1 \times 10^5$ Hz and $W_{ca} = 2.6 \pm 3.1 \times 10^6$ Hz. Uncertainties are determined using standard error propagation techniques. Then using our rate equation solution (B.10) and calculated A coefficients (B.11), we solve for $N_e/N = 0.130 \pm 0.025$, which is the steady-state fraction of atoms in the $F' = 4$ excited state.

Table B.1: Summary of parameters involved in calculating the stimulated scattering rates [89, 99]. Linewidths/detunings are given in angular frequency ($\omega = 2\pi\nu$).

Transition	τ_{ij} (ns)	γ_{ij} (MHz)	Wavelength (nm)	I_s (mW/cm^2)	Δ (MHz)	I (mW/cm^2)
$5 \rightarrow 2$	21.02(11)	7.57(4)	718.0402(1)	2.67(1)	12(3)	22(5)
$4 \rightarrow 2$	37.84(20)	4.21(2)	718.0403(1)	1.485(8)	46(3)	22(5)
$3 \rightarrow 1$	53.01(20)	3.00(1)	816.9653(2)	0.720(3)	3(3)	1.4(5)

Next, we solve the rate equation for N_d/N:

$$\begin{aligned}\frac{N}{N_d} &= \frac{N_a}{N_d} + \frac{N_b}{N_d} + \frac{N_c}{N_d} + \frac{N_d}{N_d} + \frac{N_e}{N_d} \\ &= \frac{N_a}{N_c}\frac{N_c}{N_d} + \frac{N_b}{N_d} + \frac{N_c}{N_d} + 1 + \frac{N_e}{N_b}\frac{N_b}{N_d} \\ &= C_{ca}C_{dc} + C_{db} + C_{dc} + 1 + \frac{C_{db}}{C_{eb}}. \end{aligned} \tag{B.15}$$

From this we obtain $N_d/N = 0.0061 \pm 0.0008$. Finally, the last relevant level population is found by:

$$\begin{aligned}\frac{N}{N_c} &= \frac{N_a}{N_c} + \frac{N_b}{N_c} + \frac{N_c}{N_c} + \frac{N_d}{N_c} + \frac{N_e}{N_c} \\ &= \frac{N_a}{N_c} + \frac{N_b}{N_d}\frac{N_d}{N_c} + 1 + \frac{N_d}{N_c} + \frac{N_e}{N_b}\frac{N_b}{N_d}\frac{N_d}{N_c} \\ &= C_{ca} + \frac{C_{db}}{C_{dc}} + 1 + \frac{1}{C_{dc}} + \frac{C_{db}}{C_{eb}C_{dc}}. \end{aligned} \tag{B.16}$$

The result is $N_c/N = 0.0085 \pm 0.0038$. We now have population fractions for all three excited states. Summing produces the total excited state fraction $n_{excited}(\text{full}) = 0.144 \pm 0.025$.

Appendix C

Neutralizer current timer interlock

The current timer interlock mentioned in section 3.2.1, designed and built by the author, consists of a series of timer delay blocks and logic gates. Its purpose is to transmit a logic-high pulse for up to 1 s and to not transmit any other pulses for the following 10 s. If the input is logic-high for longer than 1 s, the interlock forces its output low. Similarly, if a second high pulse arrives within 10 s of the first, the interlock output remains low. This is to ensure that the neutralizer foil is neither heated for too long nor heated again before it is completely cooled off. The concern is that either of these states may damage the neutralizer, which would cause a decrease in neutral atom release or a complete failure and termination of trapping. It is a major task to replace a broken neutralizer foil due to the complexity of the assembly, requirement of the spot-welding, regenerating the ultra-high vacuum needed for trapping, and radiation safety concerns once beam is delivered to the apparatus. Thus, the reliability of the heating current is worthy of concern.

The core of the timer interlock is a pair of Texas Instruments NE555P precision

timer chips. The timing characteristics of each chip is controlled by an RC constant set by a resistor in series with a trim pot and a capacitor. The trim pots can be accessed from the front of the box for fine tuning. The first chip controls the 1 s pulse duration limit and the second controls the 10 s pulse repetition limit. A series of logic gates (Texas Instruments SN74LS08N AND gates and SN74LS04N inverters) pass the signals correctly for this combined function.

The output of the timer-gate circuit is sent to a voltage divider whose ratio is set by a finger-turn potentiometer on the front of the interlock box. This controls the exact level of the output, so that the signal sent to the Kepco supply voltage control causes the correct current to be output. This voltage is set slightly above the voltage required for the desired current output of the supply, as determined by the resistance of the foil through its electrical connection. Thus the supply, when triggered, operates in constant current mode and, when the trigger goes low, switches to being voltage limited and stops outputting current. That way, the power through the neutralizer will not increase as the foil ages and the resistance changes; if the foil tends to lower resistance, the supply remains current limited while if it tends to higher resistance, the limit set by the voltage of the interlock box will prevent a much higher current from being output.

The voltage control of the supply is set on the backpanel of the supply through a built-in operational amplifier. The pins connected to the timer interlock box set the inputs of the supply amplifier and connect the grounds of the power supply and interlock box. A zeroing pre-amp on the supply is set so that the interlock low output, which may not be exactly ground compared to the Kepco supply, corresponds to no

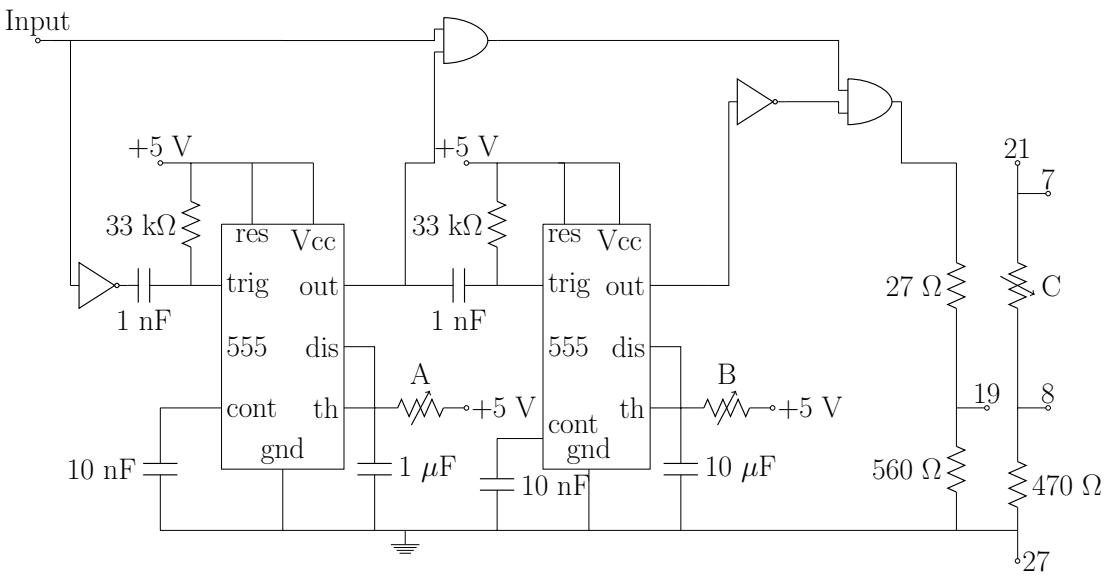

Figure C.1: Circuit diagram for the timer interlock box. Labels A, B are each a 820 kΩ resistors in series with a 100 kΩ trim pot to fine tune the timer values and C is for a 20 kΩ potentiometer to set the output level to the Kepco power supply. The inputs on the rectangular 555 timer chips are: reset (res), trigger (trig), control-voltage (cont), threshold (th) and discharge (dis). Numerical outputs correspond to the pin numbers of the Kepco control bus connecting to its voltage control amplifier: output (7), inverting input (8), non-inverting input (19), drive voltage (21) and common ground (27).

current output to the neutralizer.

Appendix D

LabView-based laser control program

This appendix examines the laser frequency-lock system we use to correct the long term frequency drifts of our lasers. The system works by transferring the stability of a polarization stabilized HeNe laser to any other laser in the system.

The HeNe is located in the same enclosure as the confocal Fabry-Perot cavity. All of the other lasers are transmitted via fiber to a multiplexing breadboard where the beams are overlapped and then coupled into a fiber that is sent to the cavity enclosure. Inside the enclosure, the combination beam from the fiber is overlapped with the HeNe beam and transmitted through the scanning cavity. On the other side of the cavity, a series of filters and polarization optics directs individual laser beams each to their own photodiode, whose signals are read into the analog inputs of the locking computer. Figure D.1 shows a diagram of the setup and figure D.2 is a photograph of the setup in the Francium Trapping Facility at the time of writing.

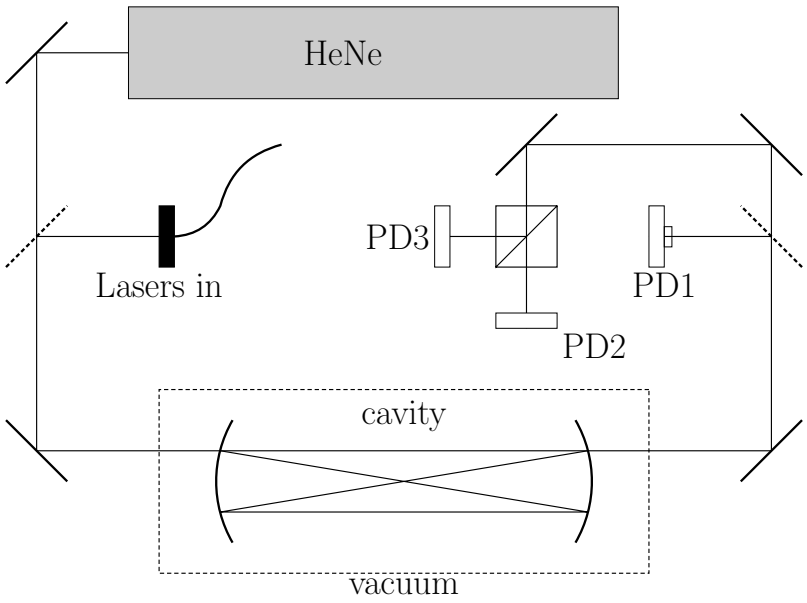

Figure D.1: Basic optics scheme for locking two lasers to the HeNe using the laser locking program. The lasers are combined with opposite polarizations into a single beam and coupled into a fiber (not shown). That fiber is coupled into the locking scheme and combined with the HeNe beam on a beamsplitter. The combined beam passes through the confocal Fabry-Perot cavity, held under vacuum to reduce atmospheric effects. After the cavity, a beamsplitter picks off light that is filtered for 633 nm on photodiode 1 (PD1). The remaining light is split on a polarizing beamsplitter and sent to the other photodiodes 2 and 3. This scheme can be expanded to additional lasers using more filters and beamsplitters.

The laser control program sets the feedback voltages applied to the locked lasers to correct for frequency drifts. It functions by generating a voltage ramp such that two adjacent fringes of the HeNe are transmitted through the cavity. The upper image of figure D.3 shows the program at initialization with a single fringe transmitted during

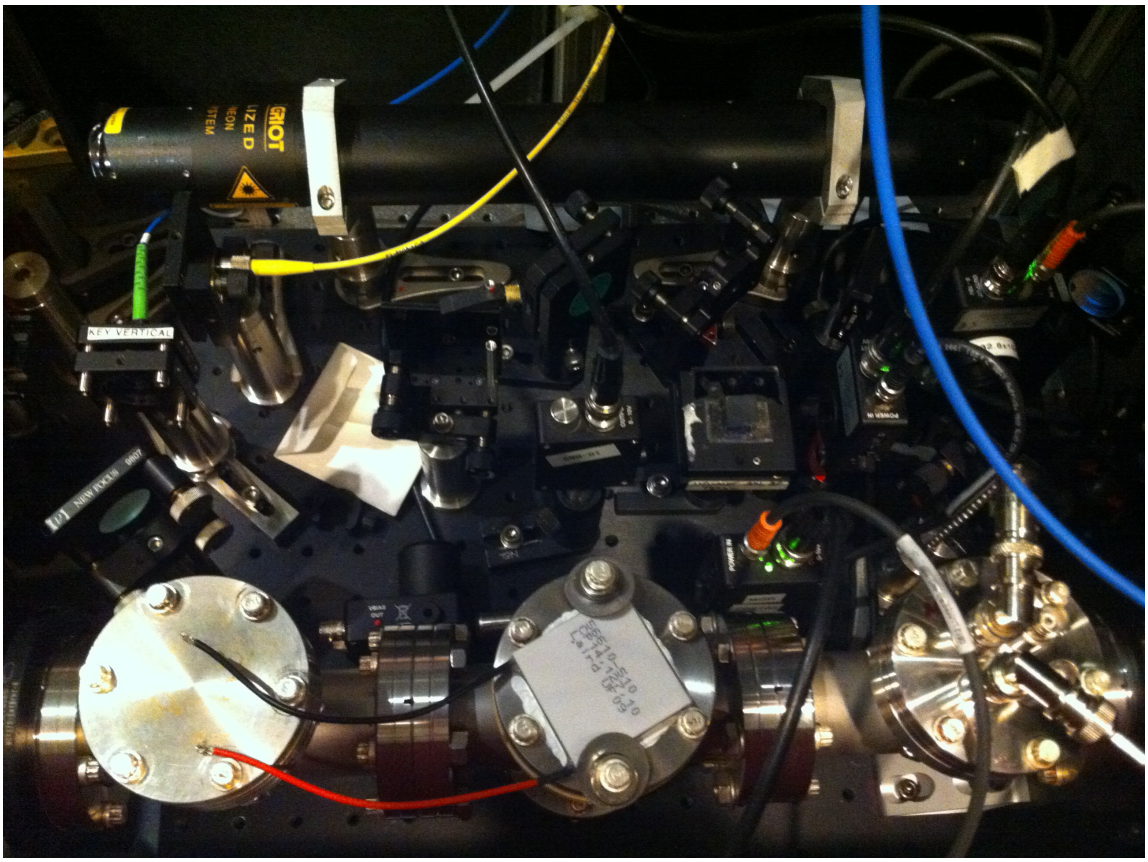

Figure D.2: Components of the cavity locking scheme. The polarization stabilized HeNe (black tube) lends its stability to any other laser passed through the scanning Fabry-Perot cavity (under vacuum). The filters and polarization optics ensure that each photodiode collects light from only a single laser, to eliminate backgrounds on the signal sent to the locking program. This displayed setup is for three lasers to be locked to the HeNe.

the voltage ramp. The lower image shows once the program has been told to lock the cavity and the ramp has been adjusted such that two adjacent fringes are transmitted through the cavity during the ramp. The ramp goes from the analog output to a high-voltage amplifier, which is connected to the piezoelectric stack attached to one of the cavity mirrors. All of the ramp parameters are set in the control program. Currently, the start value of the ramp is set by the user using buttons on the interface; a typical

initial value is about 5 V so that there is little opportunity to reach the limits of the analog output card, and the width of the ramp is adjusted by the program to position the second HeNe peak in a preset location. Previously, the width of the ramp was also set explicitly by the user.

Each photodiode signal has its own analog input channel, and the control program display is configured to communicate with the correct laser. The program tracks the relative position of the laser peak between the two HeNe peaks, and the desired locking position must be set. Peak tracking is accomplished by a two-step operation on the array of data collected from the analog input. First, the maximum value is found in a region where the peak was previously found. This requires manually setting the peak position when that channel is first initialized. Second, the peak is fit using a Lorentzian function after which the center parameter is extracted and passed to the control program. Once the program has a peak location and is told to lock that laser, it increments the output voltage by the gain times the difference between the set point and the peak position:

$$\text{output}(t+1) = \text{gain} \times (\text{set point}(t) - \text{position}(t)), \tag{D.1}$$

and iterates in order to adjust the laser's position to its set point and maintain it there. This is illustrated in figure D.4, where enabling the lock allows the program to change the output voltage and the laser position moves to the set point.

This laser control program is capable of locking four lasers independently. The wavemeter software runs in the background and communicates with the control program so that frequency readings may be acquired. Each laser has a diagnostic beam sent via fiber to a fiber switch, whose output is set by digital logic controlled by

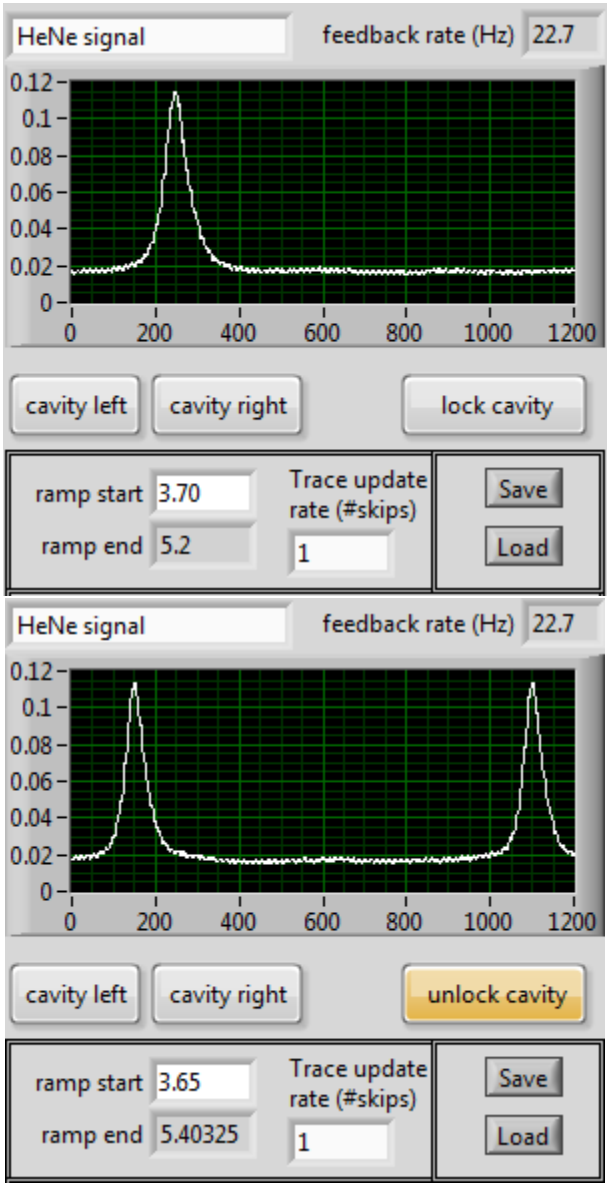

Figure D.3: (Top) Initialization of laser locking program has a default ramp width that shows one HeNe peak. Cavity left/right adjusts position of ramp and should be set at some some midway value. (Bottom) Locking the cavity allows the program to adjust the ramp width to put the next peak near the edge of the ramp.

the program. Thus the laser control program may step through the logic values and update laser frequency readings every few seconds, limited by the safe response time of the fiber switch.

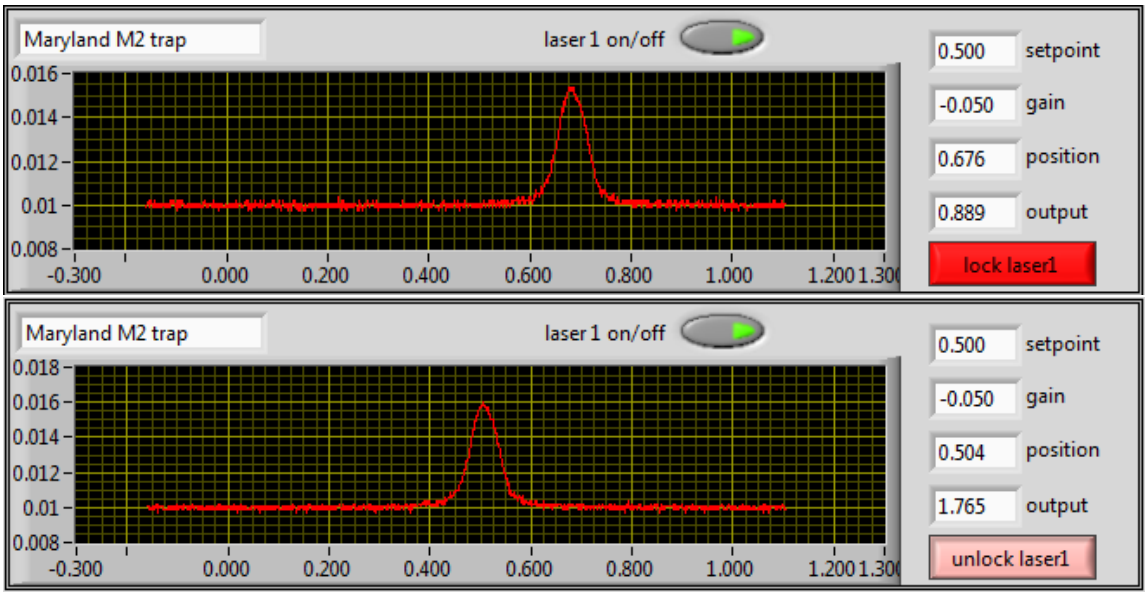

Figure D.4: (Top) The program tracks the position of the laser 1 peak relative to the two HeNe peaks. Selecting the proper laser identifier, here Maryland M2 trap, controls which analog output the voltage is applied to. It also controls the fiber switch so that wavemeter readings of that laser can be obtained. (Bottom) Once the laser is locked, the output is adjusted to move the laser position to the setpoint value. So long as the sign on the gain is correct, the quality of the feedback is largely insensitive to the magnitude of the gain, within reason.

There is no hard limitation on the number of lasers that can be locked using this scheme. It is relatively straightforward to expand the locking program to accomodate another laser. In practice though, it becomes difficult to combine additional lasers into one beam and then split them all again so that there is enough light on each photodiode for a good signal for the locking program.

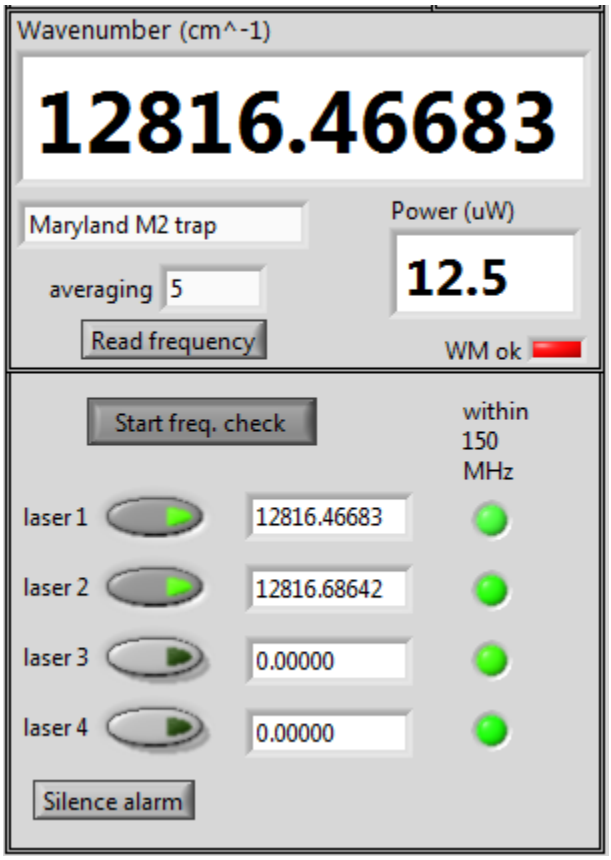

Figure D.5: The control program communicates with the wavemeter software running in the background to take frequency readings. Digital logic values, set by which laser identifier is selected for each laser display, are passed to the fiber switch determining.

Appendix E

Information on isotopes trapped at Francium Trapping Facility

This appendix includes information on the francium isotopes we have successfully trapped at TRIUMF.

Table E.1: Basic information on the francium isotopes and isomer trapped in our MOT. Also included are the maximum yields for each isotope delivered to us by the ISAC ion beam. Masses, spins and half-lives are obtained from [94]. Nuclear magnetic moments are obtained from [108]. Spins and nuclear moments for ^{206,206m}Fr, and the nuclear moment for ^{208}Fr are from [91]. For the yield measurements [109], the ISAC yield station can not distinguish between ^{206}Fr and the isomer ^{206m}Fr.

Isotope	Mass excess (keV)	Nuclear Spin	Half-life	Magnetic moment (μ_N)	Yield (ions/s)
206	-1243	3	16.0 s	3.91(3)	7.00×10^7
206m	-1048	7	15.9 s	4.68(4)	7.00×10^7
207	-2840	9/2	14.8 s	3.89(8)	8.80×10^7
208	-2670	7	59.1 s	4.71(4)	2.60×10^8
209	-3769	9/2	50.0 s	3.95(8)	5.90×10^8
210	-3346	6	3.18 min	4.40(9)	9.10×10^8
211	-4158	9/2	3.10 min	4.00(8)	1.30×10^9
212	-3538	5	20.0 min	4.62(9)	1.20×10^9
213	-3550	9/2	34.6 s	4.02(8)	1.20×10^9
221	13278	5/2	4.9 min	1.58(3)	1.20×10^8

Bibliography

[1] Drell, P. S. and Commins, E. D. *Physical Review A* **32**, 2196–2210 Oct (1985).

[2] Tsigutkin, K., Dounas-Frazer, D., Family, A., Stalnaker, J. E., Yashchuk, V. V., and Budker, D. *Physical Review A* **81**, 032114 Mar (2010).

[3] Wood, C. S., Bennett, S. C., Roberts, J. L., Cho, D., and Wieman, C. E. *Canadian Journal of Physics* **77**(1), 7–75 (1999).

[4] Erler, J. In *Journal of Physics: Conference Series*, volume 485, 012010. IOP Publishing, (2014).

[5] Androic, D. et al. *Physical Review Letters* **111**, 141803 (2013).

[6] Collister, R., Gwinner, G., Tandecki, M., Behr, J. A., Pearson, M. R., Zhang, J., Orozco, L. A., Aubin, S., and Gomez, E. *Physical Review A* **90**(5), 052502 (2014).

[7] Wu, C. S., Ambler, E., Hayward, R. W., Hoppes, D. D., and Hudson, R. P. *Physical Review* **105**, 1413–1415 (1957).

[8] Garwin, R. L., Lederman, L. M., and Weinrich, M. *Physical Review* **105**, 1415–1417 (1957).

[9] Friedman, J. I. and Telegdi, V. L. *Physical Review* **105**, 1681–1682 (1957).

[10] Glashow, S. L. *Nuclear Physics* **22**(4), 579–588 (1961).

[11] Weinberg, S. *Physical Review Letters* **19**, 1264–1266 (1967).

[12] Salam, A. *Proceedings of the Eighth Nobel Symposium on Elementary Particle Theory, Relativistic Groups, and Analyticity, Stockholm, Sweden* (1968).

[13] Khriplovich, I. B. *Parity Nonconservation in Atomic Phenomena*. Gordon and Breach Science Publishers, (1991).

[14] Haxton, W. C. and Wieman, C. E. *Annual Review of Nuclear and Particle Science* **51**(1), 261–293 (2001).

[15] Haxton, W. C., Liu, C.-P., and Ramsey-Musolf, M. J. *Physical Review C* **65**, 045502 (2002).

[16] Bouchiat, M. A. and Bouchiat, C. C. *Physics Letters B* **48**(2), 111–114 (1974).

[17] Baird, P. E. G., Brimicombe, M. W. S. M., Roberts, G. J., Sandars, P. G. H., Soreide, D. C., Fortson, E. N., Lewis, L. L., and Lindahl, E. G. *Nature* **264**, 528–529.

[18] Barkov, L. M. and Zolotorev, M. S. *Journal of Experimental and Theoretical Physics Letters* **27**(6), 379–383 (1978).

[19] Barkov, L. M. and Zolotorev, M. S. *Soviet Physics Journal of Experimental and Theoretical Physics Letters* **52**(3), 360–369 (1980).

[20] Birich, G. N., Bogdanov, Y. V., Kanorskii, S. I., Sobelman, I. I., Sorokin, V. N., Struk, I. I., and Yukov, E. A. *Soviet Physics Journal of Experimental and Theoretical Physics Letters* **60**, 442–449 (1984).

[21] Hollister, J. H., Apperson, G. R., Lewis, L. L., Emmons, T. P., Vold, T. G., and Fortson, E. N. *Physical Review Letters* **46**(10), 643 (1981).

[22] Macpherson, M. J. D., Zetie, K. P., Warrington, R. B., Stacey, D. N., and Hoare, J. P. *Physical Review Letters* **67**(20), 2784 (1991).

[23] Warrington, R. B., Thompson, C. D., and Stacey, D. N. *Europhysics Letters* **24**(8), 641 (1993).

[24] Edwards, N. H., Phipp, S. J., Baird, P. E. G., and Nakayama, S. *Physical Review Letters* **74**(14), 2654 (1995).

[25] Vetter, P. A., Meekhof, D. M., Majumder, P. K., Lamoreaux, S. K., and Fortson, E. N. *Physical Review Letters* **74**(14), 2658 (1995).

[26] Meekhof, D. M., Vetter, P., Majumder, P. K., Lamoreaux, S. K., and Fortson, E. N. *Physical Review Letters* **71**(21), 3442 (1993).

[27] Wood, C. S., Bennett, S. C., Cho, D., Masterson, B. P., Roberts, J. L., Tanner, C. E., and Wieman, C. E. *Science* **275**(5307), 1759–1763 (1997).

[28] DeMille, D., Budker, D., and Commins, E. D. *Physical Review A* **50**(6), 4657 (1994).

[29] Tsigutkin, K., Dounas-Frazer, D., Family, A., Stalnaker, J. E., Yashchuk, V. V., and Budker, D. *Physical Review Letters* **103**(7), 071601 (2009).

[30] Bowers, C. J., Budker, D., Freedman, S. J., Gwinner, G., Stalnaker, J. E., and DeMille, D. *Physical Review A* **59**(5), 3513 (1999).

[31] Bouchiat, M. A., Guena, J., Hunter, L., and Pottier, L. *Physics Letters B* **117**(5), 358–364 (1982).

[32] Bouchiat, M. A., Guena, J., Pottier, L., and Hunter, L. *Physics Letters B* **134**(6), 463–468 (1984).

[33] Bennett, S. C. and Wieman, C. E. *Physical Review Letters* **82**(12), 2484 (1999).

[34] Rosner, J. L. *Physical Review D* **65**(7), 073026 (2002).

[35] Porsev, S. G., Beloy, K., and Derevianko, A. *Physical Review Letters* **102**(18), 181601 (2009).

[36] Dzuba, V. A., Berengut, J. C., Flambaum, V. V., and Roberts, B. *Physical Review Letters* **109**, 203003 (2012).

[37] Erler, J., Kurylov, A., and Ramsey-Musolf, M. J. *Physical Review D* **68**(1), 016006 (2003).

[38] Diener, R., Godfrey, S., and Turan, I. *Physical Review D* **86**, 115017 (2012).

[39] Bouchiat, C. and Fayet, P. *Physics Letters B* **608**(1), 87–94 (2005).

[40] Cheung, K. *Physics Letters B* **517**(12), 167 – 176 (2001).

[41] Antypas, D. and Elliott, D. S. *Physical Review A* **87**, 042505 (2013).

[42] Nuez Portela, M., Dijck, E. A., Mohanty, A., Bekker, H., van den Berg, J. E., Giri, G. S., Hoekstra, S., Onderwater, C. J. G., Schlesser, S., Timmermans, R. G. E., Versolato, O. O., Willmann, L., Wilschut, H. W., and Jungmann, K. *Applied Physics B* **114**(1-2), 173–182 (2014).

[43] Williams, S. R., Jayakumar, A., Hoffman, M. R., Blinov, B. B., and Fortson, E. N. *Physical Review A* **88**, 012515 (2013).

[44] Cahn, S. B., Ammon, J., Kirilov, E., Gurevich, Y. V., Murphree, D., Paolino, R., Rahmlow, D. A., Kozlov, M. G., and DeMille, D. *Physical Review Letters* **112**, 163002 (2014).

[45] Inoue, T., Ando, S., Aoki, T., Arikawa, H., Ezure, S., Harada, K., Hayamizu, T., Ishikawa, T., Itoh, M., Kato, K., Kawamura, H., Uchiyama, A., Aoki, T., Asahi, K., Furukawa, T., Hatakeyama, A., Hatanaka, K., Imai, K., Murakami, T., Nataraj, H. S., Sato, T., Shimizu, Y., Wakasa, T., Yoshida, H. P., Yoshimi, A., and Sakemi, Y. *Hyperfine Interactions* **231**(1-3), 157–162 (2015).

[46] Munger Jr, C. T., Feinberg, B., Gould, H., Kalnins, J., Nishimura, H., Jentschura, U., Behr, J., and Pearson, M. In *APS Division of Nuclear Physics Meeting Abstracts*, volume 1, (2014).

[47] Mariotti, E., Khanbekyan, A., Marinelli, C., Marmugi, L., Moi, L., Corradi, L., Dainelli, A., Calabrese, R., Mazzocca, G., and Tomassetti, L. *International Journal of Modern Physics E* **23**(05) (2014).

[48] Kuchiev, M. Y. and Flambaum, V. V. *Physical Review Letters* **89**, 283002 (2002).

[49] Savukov, I. M., Derevianko, A., Berry, H. G., and Johnson, W. R. *Physical Review Letters* **83**, 2914–2917 (1999).

[50] Brown, B. A., Derevianko, A., and Flambaum, V. V. *Physical Review C* **79**, 035501 (2009).

[51] Haxton, W. C. *Nuclear Physics A* **827**(1), 42c–52c (2009).

[52] Safronova, M. S. and Johnson, W. R. *Physical Review A* **62**, 022112 (2000).

[53] Dzuba, V. A., Flambaum, V. V., and Sushkov, O. P. *Physical Review A* **51**, 3454–3461 (1995).

[54] Gomez, E., Aubin, S., Sprouse, G. D., Orozco, L. A., and DeMille, D. P. *Physical Review A* **75**, 033418 (2007).

[55] Flambaum, V. V., Khriplovich, I. B., and Sushkov, O. P. *Physics Letters B* **146**(6), 367 – 369 (1984).

[56] Bouchiat, M. A. and Bouchiat, C. *Journal de Physique* **36**(6), 493–509 (1975).

[57] Nörtershäuser, W., Sánchez, R., Ewald, G., Dax, A., Behr, J., Bricault, P., Bushaw, B. A., Dilling, J., Dombsky, M., Drake, G., et al. *Physical Review A* **83**(1), 012516 (2011).

[58] Nieminen, A., Campbell, P., Billowes, J., Forest, D. H., Griffith, J. A. R.,

Huikari, J., Jokinen, A., Moore, I. D., Moore, R., Tungate, G., et al. *Physical Review Letters* **88**(9), 094801 (2002).

[59] Kozlov, M. G., Korol, V. A., Berengut, J. C., Dzuba, V. A., and Flambaum, V. V. *Physical Review A* **70**(6), 062108 (2004).

[60] Aoki, W., Ryan, S. G., Norris, J. E., Beers, T. C., Ando, H., Iwamoto, N., Kajino, T., Mathews, G. J., and Fujimoto, M. Y. *The Astrophysical Journal* **561**(1), 346 (2001).

[61] Ginges, J. S. M. and Flambaum, V. V. *Physics Reports* **397**(2), 63–154 (2004).

[62] Ramsey-Musolf, M. J. and Page, S. A. *Annual Review of Nuclear and Particle Science* **56**(1), 1–52 (2006).

[63] Gwinner, G., Gomez, E., Orozco, L. A., Perez Gaivan, A., Sheng, D., Zhao, Y., Sprouse, G. D., Behr, J. A., Jackson, K. P., Pearson, M. R., Aubin, S., and Flambaum, V. V. *Hyperfine Interactions* **172**(1-3), 45–51 (2006).

[64] Dzuba, V. A., Johnson, W. R., and Safronova, M. S. *Physical Review A* **72**(2), 022503 (2005).

[65] King, W. H. *Isotope Shifts in Atomic Spectra*. Physics of atoms and molecules. Plenum Press, (1984).

[66] Heilig, K. and Steudel, A. *Atomic Data and Nuclear Data Tables* **14**(5), 613–638 (1974).

[67] Blundell, S. A., Baird, P., Palmer, C. W. P., Stacey, D. N., and Woodgate, G. K. *Journal of Physics B: Atomic and Molecular Physics* **20**(15), 3663 (1987).

[68] Seltzer, E. C. *Physical Review* **188**(4), 1916 (1969).

[69] Angeli, I. *Acta Physica Hungarica Series A, Heavy Ion Physics* **17**(1), 3–9 (2003).

[70] Tandecki, M., Zhang, J., Collister, R., Aubin, S., Behr, J. A., Gomez, E., Gwinner, G., Orozco, L. A., and Pearson, M. R. *Journal of Instrumentation* **8**(12), P12006 (2013).

[71] Aubin, S., Gomez, E., Orozco, L. A., and Sprouse, G. D. *Review of Scientific Instruments* **74**(10), 4342–4351 (2003).

[72] Fedchak, J. A., Cabauy, P., Cummings, W. J., Jones, C. E., and Kowalczyk, R. S. *Nuclear Instruments and Methods in Physics Research Section A: Accelerators, Spectrometers, Detectors and Associated Equipment* **391**(3), 405–416 (1997).

[73] Metcalf, H. J. and van der Straten, P. *Laser Cooling and Trapping*. Graduate Texts in Contemporary Physics. Springer, (1999).

[74] Zhang, J. *Spectroscopy with laser-cooled francium and progress on atomic parity non-conservation*. PhD thesis, University of Maryland, (2015).

[75] Zhao, W. Z., Simsarian, J. E., Orozco, L. A., and Sprouse, G. D. *Review of Scientific Instruments* **69**(11), 3737–3740 (1998).

[76] Tandecki, M., Zhang, J., Aubin, S., Behr, J. A., Collister, R., Gomez, E., Gwinner, G., Heggen, H., Lassen, J., Orozco, L. A., et al. *Journal of Instrumentation* **9**(10), P10013 (2014).

[77] Scientific Instrument Services Inc. *SIMION (R) Ion and Electron Optics Simulation Software (Version 8.0).*

[78] Ellmer, K. *Nature Photonics* **6**(12), 809–817 (2012).

[79] Wood, C. S. *High precision atomic parity nonconservation measurement using a spin polarized cesium beam and the nuclear anapole moment of Cesium-133.* PhD thesis, University of Colorado at Boulder, (1997).

[80] Carter, J. and Martin, J. *Physical Review A* **83**(3), 032902 (2011).

[81] Silverans, R. E., Borghs, G., Dumont, G., and Van den Cruyce, J. M. *Zeitschrift für Physik A Atoms and Nuclei* **295**(4), 311–314 (1980).

[82] Lu, M., Youn, S. H., and Lev, B. L. *Physical Review A* **83**, 012510 (2011).

[83] Brandi, F., Velchev, I., Hogervorst, W., and Ubachs, W. *Physical Review A* **64**, 032505 (2001).

[84] Piller, C., Gugler, C., Jacot-Guillarmod, R., Schaller, L. A., Schellenberg, L., Schneuwly, H., Fricke, G., Hennemann, T., and Herberz, J. *Physical Review C* **42**, 182–189 (1990).

[85] Shera, E. B., Wohlfahrt, H. D., Hoehn, M. V., and Tanaka, Y. *Physics Letters B* **112**(2), 124–128 (1982).

[86] Sansonetti, J. E. *Journal of Physical and Chemical Reference Data* **36**(2), 497–508 (2007).

[87] Zhang, J., Tandecki, M., Collister, R., Aubin, S., Behr, J., Gomez, E., Gwinner, G., Orozco, L., Pearson, M., Sprouse, G., et al. *Physical Review Letters* **115**(4), 042501 (2015).

[88] Steck, D. A. *Quantum and Atom Optics*. available online at http://steck.us/teaching (revision 0.10.1, 30 April 2015).

[89] Simsarian, J. E., Orozco, L. A., Sprouse, G. D., and Zhao, W. Z. *Physical Review A* **57**(4), 2448 (1998).

[90] Coc, A., Thibault, C., Touchard, F., Duong, H. T., Juncar, P., Liberman, S., Pinard, J., Lermé, J., Vialle, J. L., Büttgenbach, S., et al. *Physics Letters B* **163**(1), 66–70 (1985).

[91] Voss, A., Buchinger, F., Cheal, B., Crawford, J. E., Dilling, J., Kortelainen, M., Kwiatkowski, A. A., Leary, A., Levy, C. D. P., Mooshammer, F., Ojeda, M. L., Pearson, M. R., Procter, T. J., and Tamimi, W. A. *Physical Review C* **91**, 044307 (2015).

[92] Sanguinetti, S., Calabrese, R., Corradi, L., Dainelli, A., Khanbekyan, A., Mariotti, E., de Mauro, C., Minguzzi, P., Moi, L., Stancari, G., et al. *Optics Letters* **34**(7), 893–895 (2009).

[93] Duong, H. T., Juncar, P., Liberman, S., Mueller, A. C., Neugart, R., Otten, E. W., Peuse, B., Pinard, J., Stroke, H. H., Thibault, C., et al. *Europhysics Letters* **3**(2), 175 (1987).

[94] Audi, G., Bersillon, O., Blachot, J., and Wapstra, A. H. *Nuclear Physics A* **729**(1), 3–128 (2003).

[95] Mårtensson-Pendrill, A.-M. *Molecular Physics* **98**(16), 1201–1204 (2000).

[96] Burkhardt, C. E., Libbert, J. L., Xu, J., Leventhal, J. J., and Kelley, J. D. *Physical Review A* **38**(11), 5949 (1988).

[97] Nygaard, K. J., Hebner Jr, R. E., Jones, J. D., and Corbin, R. J. *Physical Review A* **12**(4), 1440 (1975).

[98] Dinneen, T. P., Wallace, C. D., Tan, K.-Y. N., and Gould, P. L. *Optics Letters* **17**(23), 1706–1708 (1992).

[99] Lu, Z.-T., Corwin, K. L., Vogel, K. R., Wieman, C. E., Dinneen, T. P., Maddi, J., and Gould, H. *Physical Review Letters* **79**(6), 994 (1997).

[100] Petrov, I. D., Sukhorukov, V. L., Leber, E., and Hotop, H. *The European Physical Journal D-Atomic, Molecular, Optical and Plasma Physics* **10**(1), 53–65 (2000).

[101] Burchianti, A., Bogi, A., Marinelli, C., Mariotti, E., and Moi, L. *Physica Scripta* **2009**(T135), 014012 (2009).

[102] Preses, J. M., Burkhardt, C. E., Corey, R. L., Earsom, D. L., Daulton, T. L., Garver, W. P., Leventhal, J, J., Msezane, A. Z., and Manson, S. T. *Physical Review A* **32**(2), 1264 (1985).

[103] Maragò, O., Ciampini, D., Fuso, F., Arimondo, E., Gabbanini, C., and Manson, S. T. *Physical Review A* **57**(6), R4110 (1998).

[104] Gilbert, S., Noecker, M., and Wieman, C. *Physical Review A* **29**(6), 3150 (1984).

[105] Vieira, D. J., Wieman, C. E., Bolton, R. D., Bowman, J. D., Chamerlin, E. P., Fearey, B. L., Gould, H. A., Oona, H., Sandberg, V. D., Stephens, M., Swenson, D. R., Talbert, W. L., Tupa, D., White, D. H., and Wouters, J. M. *Los Alamos Meson Physics Facility Research Proposal* **1303** (1992).

[106] Safronova, M. S., Johnson, W. R., and Derevianko, A. *Physical Review A* **60**(6), 4476 (1999).

[107] Simsarian, J. E., Zhao, W. Z., Orozco, L. A., and Sprouse, G. D. *Physical Review A* **59**(1), 195 (1999).

[108] Ekström, C., Robertsson, L., and Rosén, A. *Physica Scripta* **34**(6A), 624 (1986).

[109] *Yields for francium beams, ISAC Yield Database.*